# Gain and Efficiency Enhancement of the Miniaturized Split Ring Based Antennas

by

Yanxia Liu

A Thesis submitted to the Faculty of Graduate Studies of

The University of Manitoba

in partial fulfilment of the requirements of the degree of

MASTER OF SCIENCE

Department of Electrical and Computer Engineering

University of Manitoba

Winnipeg

# Abstract

Small antennas are very attractive due to their compactness and lightness. However, the price one has to pay for having a small antenna, such as significant reduction in radiation efficiency, gain and bandwidth, makes them less practical and less useful. This thesis demonstrates how one can miniaturize an antenna by artificially inducing high-permeability in the antenna such that less efficiency and gain will be sacrificed. The improvement in efficiency is achieved by reducing the losses in the antenna; and the improvement in gain is achieved by increasing both efficiency and directivity, which are realized by reducing the losses in the antenna and replacing a conventional ground plane with a U-shaped ground plane, respectively. The high-permeability is induced by employing metallic loops (e.g. split ring resonators (SRRs)) and properly arranging them with respect to the magnetic field. First, split ring loaded dielectric resonator antennas are studied. It is shown that loading a conventional dielectric resonator antenna (DRA) with SRRs can indeed miniaturize the antenna. The miniaturization capability varies with SRR parameters and arrangements: the larger the SRR area, the higher the miniaturization capability. The arrangement of a single SRR allows for the most miniaturization, compared to other arrangements, but the others can provide wider bandwidths. One of the examples shows that loading a very low-permittivity ($\varepsilon_r = 2.2$) based DRA with three layers of single SRR is equivalent to increasing the permittivity of the dielectric to $\varepsilon_r = 976$. The miniaturized antenna also has a reasonably good efficiency (80.85%) and gain (6.69 dBi), despite its small dimensions ($0.124\lambda_0 \times 0.062\lambda_0 \times 0.002\lambda_0$). In order to further miniaturize the SRR loaded DRAs, two types of metallization, namely U-shaped and split-ring-shaped metallizations, are applied to the surfaces of the loaded DRAs. It is found that both metallizations have little effect on a single-element

loaded DRA, but can effectively miniaturize the unloaded DRA, since similar to SRRs, both metallizations are also capable of inducing permeability. Therefore, a probe-fed flat-wire open ring antenna, essentially just the split-ring-shaped metallization, is also studied. Good antenna performance (efficiency of 86.36% and gain of 7.94 dBi) is also observed with such a miniaturized antenna (dimensions: $0.113\lambda_0 \times 0.057\lambda_0 \times 0.011\lambda_0$). In order to further miniaturize the open ring antenna, a two-turn flat-wire open ring with different slit combinations is investigated. By placing the slit of the outer ring at the bottom and the slit of the inner ring at the top, the antenna can be most effectively miniaturized.

# Acknowledgement

I would like to first express my gratitude to my supervisor, Dr. L. Shafai, whose expertise, patience and encouragement has made this journey so much easier and more enjoyable than it could have been. With the vast knowledge he has, he is so down to earth and approachable and encourages questions and different opinions. Without his generous financial support, it would have been impossible for me to fully concentrate on my research work, and neither would have had the opportunity to attend so many conferences that have helped boost my confidence immensely. He has also been incredibly generous in sharing his time, ideas and experience with me. I appreciated all these meaningful and interesting discussions we had. I was especially moved how he reacted and responded positively when I was unable to attend a conference because of the delayed visa. It is an absolute honor and pleasure to be his student and to work with him.

I would also like to thank Dr. Dustin Isleifson and Dr. Stephen Pistorius, for agreeing to be my examining committee despite their busy schedules, and for their time and effort in reading this thesis and providing valuable feedback.

A very special thanks goes out to our fabrication and measurement team, Mr. Cory Smit and Mr. Brad Tabachnick. I am so grateful that they went above and beyond their duty to ensure that I would get perfect experimental results.

I must also express my gratitude to the office staff, Ms. Amy Dario, Ms. Shelly Girardin, Ms. Heather Katrick, Ms. Judy Noble, etc., for their kind assistance during my graduate program.

To my dearest friend, Karen Dawes: I miss you. You were the happiest and the most positive person I have ever met, and you were also the most pleasant friend to be around. It has never been the same since you left. I will never forget those old times when you had to get up very early in the morning to talk to me and help me improve my English so that I would feel more comfortable when I came to Canada. You and Andy made your home my first home here in Canada. With those warm welcomes and carefully planned activities, you never let me feel that I was actually far away from home. I miss those long letters we used to write to each other and I miss your screams of joy and those long hugs whenever we reunited. You have inspired me to be a better friend and to be a happier person, which truly made a difference in my life.  How lucky I am to have had a friend like you.

To one very special friend and mentor, CS Watt: without you reaching out to me and checking out my progress every so often, I wouldn't get out of those depressing phases so quickly and regain my motivation to finish this work. I am so grateful to have such a wise, caring and supportive friend like you.

I must also acknowledge those friends who have been supporting me along the way: Bixia Wang, Ching Tien, Cindy Jensen, Francis Lai, Carla Stucchi, Andrew Dawes and Ilze. Appreciation also goes out to all the teachers who have taught and inspired me, especially my undergraduate supervisor Prof. Fengxun Gong. It was under his guidance that I became interested in doing

research and discovered my passion for antennas. And of course, I am also very grateful for the related work done by many great researchers that has helped lay the foundation of this work. Thanks also goes out to all my colleagues for those interesting and useful discussions.

Finally, I want to thank my family for their unconditional love and support. In particular, I must acknowledge my grandfather and role model, Shijie Liu, who inspired me and encouraged me to appreciate knowledge and to enjoy learning. He spent his entire life learning and reading, even during his final days. It was him who answered each and every single question of mine when I was a kid instead of killing my curiosity.

# Table of Contents

# List of Figures

# List of Tables

# List of Symbols and Acronyms

| Symbol | Description | Symbol | Description | Symbol | Description |
|--------|-------------|--------|-------------|--------|-------------|
| $\varepsilon_r$ | Relative Permittivity | MSRR | Multiple Split Ring Resonator | $P_{prox}$ | Conductor Loss due to Proximity Effect |
| $\mu_r$ | Relative Permeability | SR | Spiral Resonator | $\delta$ | Skin Depth |
| $f_r$ | Resonant Frequency | $\tan \delta$ | Loss Tangent | $\sigma$ | Conductivity |
| $\lambda_0$ | Free-space Wavelength | $P_h$ | Hysteresis Loss | AMDRA | Artificial Magneto-dielectric Resonator Antenna |
| $\lambda$ | Wavelength | $k_h$ | Steinmetz Hysteresis Constant | L | Length of the Antenna |
| PILA | Planar Inverted-L Antenna | $B_{max}$ | Maximum Magnetic Flux Density | H | Height of the Antenna |
| PIFA | Planar Inverted-F Antenna | f | Frequency | W | Width of the Antenna |
| DRA | Dielectric Resonator Antenna | V | Volume | w | Split Ring Trace Width |
| MNG | $\mu$-negative | $P_e$ | Eddy Current Loss | g | Split Ring Gap Width |
| ENG | $\varepsilon$-negative | $k_e$ | Eddy Current Coefficient | $L_{ground}$ | Ground Plane Length |
| EPS | $\varepsilon$-positive | $P_{diel}$ | Dielectric Loss | $H_{side\ wall}$ | Side wall height |
| ENZ | $\varepsilon$-near-zero | $\omega$ | Angular Frequency | $h_{probe}$ | Probe Height |
| ENNZ | $\varepsilon$-negative-near-zero | E | Applied Electric Field | $r_{probe}$ | Probe Radius |
| M | Magnetic Dipole Moment | $\varepsilon_0$ | Permittivity of Air | $g_{probe}$ | Gap between the Probe and the Antenna |
| $\chi$ | Magnetic Susceptibility | $\varepsilon_r{}'$ | Real Part of the Permittivity | MC | Miniaturization Capability |
| H | Magnetic Field Intensity | $\varepsilon_r{}''$ | Imaginary Part of the Permittivity | Dir | Directivity |
| I | Current | $P_{cond}$ | Conductor Loss | Co-pol | Co-polarization |
| A | Area Enclosed by a Loop | $P_{AC}$ | AC Conductor Loss | X-pol | Cross-polarization |
| SRR | Split Ring Resonator | $P_{DC}$ | DC Conductor Loss | h | Air Gap |
| CSRR | Complementary Split Ring Resonator | $P_{skin}$ | Conductor Loss due to Skin Effect | $w_{slit}$ | Slit Width |

# Chapter 1

# Introduction

## 1.1 Why Small Antennas?

As electronic devices and systems are becoming smaller and lighter, antennas, as part of the whole devices/systems, should also be miniaturized in order to make a positive contribution to the miniaturization that has been achieved by other electronic components. Being small is most desirable for an antenna only when it can work as well as, or at least is comparable to a normal sized antenna. However, this is not usually the case because the antenna performance, such as radiation efficiency, bandwidth, and impedance matching, deteriorates when its size reduces [1] [2]. Despite all these drawbacks, small antennas are of great interest for several solid reasons. First, with a small antenna, the host device will become more compact and lighter, which leads to a lower cost, but most importantly, it leads to invention of new technologies where small size and weight are essential, such as in aerospace applications. Second, if the antenna is designed for portable devices, such as cell phones, laptops, RFID (Radio Frequency Identification) tags, wearable sensors, etc., or implantable biomedical applications, being small and light not only makes it more comfortable and convenient for the users to carry/wear, but also allows for space to be saved for new features. Thanks to advanced manufacturing techniques, antenna miniaturization has been pushed into a new level, especially with miniaturization techniques that involves utilizing small features, such as metamaterials in the microwave region or above.

## 1.2 Antenna Miniaturization Techniques

To date, all antenna miniaturization techniques that have been used can be classified into the following five categories.

## I. Material Loading

By using high permittivity and/or high permeability materials, the antenna size can be reduced by a factor of $1/\sqrt{\varepsilon_r \mu_r}$ ($\varepsilon_r$ and $\mu_r$ are relative permittivity and permeability, respectively) due to the reduced velocity and wavelength in such materials. In [3] and [4], high permittivity materials are applied to miniaturize a microstrip patch antenna and a dielectric resonator antenna, respectively. By using high permittivity materials antennas can be miniaturized by a factor of $1/\sqrt{\varepsilon_r}$, and also these high permittivity materials are widely available in nature. Similarly, high permeability materials have also been widely used in antenna miniaturization, allowing for a miniaturization factor of $\sqrt{\mu_r}$ [5] [6]. However, they are mostly limited to applications with operating frequencies up to the lower end of the microwave regime, due to their unacceptably high losses at higher frequencies [7] . Despite their equal ability of miniaturizing antennas, these two types of materials demonstrate different effects on bandwidth reduction as a result of antenna size reduction. It has been reported that the antennas miniaturized by using high permittivity materials suffer more bandwidth reduction compared to the ones miniaturized by using high permeability materials or magneto-dielectric materials [8] [9].

## II. Geometry and Shape Modification

An antenna can also be miniaturized by increasing the surface current path, while keeping the antenna physical dimensions unchanged. For planar antennas such as microstrip patch antennas, a longer current path can be obtained by properly modifying the shape of the antenna, such as adding slots to the antenna and inserting slits on the non-radiating edges of the antenna. Slots reduce the antenna size by inducing a meandering surface current, and thus their shape can be very flexible. It has been reported that microstrip antennas can be effectively miniaturized by adding rectangular [10], circular [11], triangular slots [12] or fractal slots [13], to the radiating patch, or by inserting single [14] [15] or multiple slits [16] on the non-radiating edges of the antenna. Many well-known miniaturized microstrip antennas, such as ring-shaped, U-shaped, and H-shaped patch antennas, are designed by using this ideology [17].

## III. Using Ground Planes and Short Circuits

As shown in [18], placing a vertical electric dipole above a ground plane (electric conductor) will create a virtual image of the electric dipole in the same direction, while placing a horizontal magnetic dipole above the ground plane will create a virtual image of the magnetic dipole in the same direction. This behavior is well known as the image theory and has been widely used to make the antenna smaller. By removing the lower arm of a vertical dipole and placing the upper arm on a ground plane, a monopole that resonates at $\lambda/4$ instead of $\lambda/2$ is formed [19].

Similar to using ground planes, adding shorting walls or shorting posts can also effectively reduce the antenna size. This miniaturization technique was first proposed by Waterhouse [20].

3

The theoretical analysis [21] suggests that the shorting post is actually acting as an inductance in series with the capacitance of the patch antenna such that the antenna size reduction is achieved. The planar inverted-L antenna (PIL) and planar inverted-F antenna (PIFA) are two well-known compact antennas designed using this technique [22]. Not only can this technique be applied to microstrip antennas, but it has also been widely used on dielectric resonator antennas (DRAs) [23] [24].

## IV. Lumped Element Loading

A miniaturized antenna ($L < \lambda_0/2$) exhibits either a strong inductance (e.g., small loop antenna) or a strong capacitance (e.g., small dipole antenna). In order to compensate for such a strong reactance, lumped element loading, such as the addition of a capacitor or inductor, is usually one of the easiest ways to make the antenna operate at a lowered frequency [19]. Similar to the shorting pin loading technique, it is proposed in [25] that an antenna can also be miniaturized by loading the antenna with a chip resistor of low resistance. A more compact antenna with a much wider bandwidth can be obtained by simply replacing the shorting pin with a $1\Omega$ chip resistor [25]. In [26], a miniaturized patch antenna with both chip resistor and chip capacitor loadings is presented, which shows that the addition of the chip capacitor to the chip-resistor loaded patch can result in more size reduction and a slight change in bandwidth. In addition to resistors and capacitors, inductors can also make an antenna smaller as reported in [27].

## V. Metamaterial Loading

Similar to the material loading with the existing high-permittivity/permeability materials, metamaterials with the engineered material properties, such as high permittivity and/or high permeability, can also be used to reduce the size of an antenna. By employing appropriate metallic inclusions, the properties of a metamaterial can be customized based on one's design requirements [28]:

- One can enhance the permittivity in a host dielectric.

- One can induce permeability in an otherwise non-magnetic material.

Unlike natural magnetic materials, engineered high-permeability materials have moderately low loss in the microwave region [29], and thus are great candidates for low-loss microwave applications [7]. In [30], a miniaturized artificial magneto-dielectric resonator antenna based on split ring resonators is proposed. The antenna was 1.8 times miniaturized and operated in the microwave region with a radiation efficiency of 88%. The authors of this paper further improved the antenna miniaturization performance in [31] by varying the inclusion parameters and arrangements, and a miniaturization level of 15.35x and a radiation efficiency of 90.19% were obtained.

Moreover, a metamaterial can also provide permittivity and permeability that are not available in a natural material at its normal state, such as negative permittivity, negative permeability, and near-zero permittivity, which can result in some exciting possibilities in antenna miniaturization. In [32], a subwavelength circular patch partially loaded with a μ-negative (MNG) metamaterial, as shown in Figure 1.1, is proposed. The μ-negative material is later obtained in [33] by employing spiral resonators (SRs) whose axes are aligned with the magnetic field. In [34], a miniaturized horn antenna loaded with embedded epsilon near zero (ENZ) metamaterial is

reported. A similar miniaturized horn antenna loaded with epsilon positive-epsilon near zero (EPS-ENZ) metamaterial is proposed in [35]. Compared to the one loaded with full-ENZ, the EPS-ENZ loaded horn antenna exhibits an even improved gain and bandwidth [35]. In [36], a miniaturized probe antenna with epsilon negative near zero (ENNZ) liner is investigated and a resonant frequency well below its natural cut-off frequency is observed.
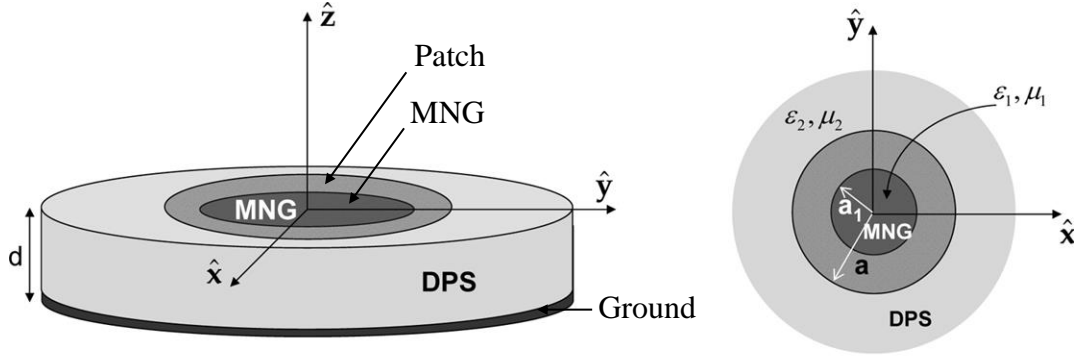


Figure 1.1 A circular patch antenna loaded with a radially inhomogeneous substrate. [32]

## 1.3 Summary

In this chapter, the advantages and disadvantages of having a small antenna were briefly discussed in the first section. In the second section, current available antenna miniaturization techniques were reviewed. Among the different miniaturization techniques, artificial high-μ loading is of specific interest of the authors due to the following reasons:

- High-μ can provide wider bandwidth than high-ε.

- Artificial high-μ is less lossy than natural high-μ at microwave frequencies.

In the following chapter, the realization of such an artificial high-μ material will be discussed.

# Chapter 2

# Artificial Magneto-Dielectric Material

As previously stated, although both high-permittivity (high-ε) and high-permeability (high-μ) materials are capable of antenna miniaturization, materials with $\mu_r > 1$ can provide wider impedance bandwidth than pure dielectric materials ($\mu_r = 1, \varepsilon_r \geq 1$) [8] [9]. Since natural magnetic materials are unusable at microwave frequencies due to their unacceptably high loss [7], there is a need for developing an alternative material that replicates the magnetic behavior of a natural magnetic material, but not its loss mechanisms. To do this, the following two steps need to be taken:

1. The causes of high-permeability in a natural magnetic material need to be understood in order to replicate the magnetic behavior.

2. The loss mechanisms in a natural magnetic material need to be understood in order to minimize the losses in an engineered magnetic material.

## 2.1 Magnetization Mechanisms

The high permeability in a natural magnetic material is mainly due to the circulating currents caused by the orbiting electrons around nuclei and spinning electrons around their own axes [37]. The circulating currents in turn create magnetic dipole moments along their axes. Therefore, if such orbital currents can be created in a medium, permeability can be induced. In order to maximize the induced permeability, the magnetic field should be aligned with the axes of the

7

current loops [38], as shown in Figure 2.1. The induced magnetic dipole moment and the induced permeability are given by

$$M = NIA \qquad (2.1)$$

$$\chi = M/H \qquad (2.2)$$

$$\mu_r = 1 + \chi \qquad (2.3)$$

where $M$ is the magnetic dipole moment, $N$ is the number of loops, $I$ is the orbital current, $A$ is the area enclosed by the loop, $\chi$ is the magnetic susceptibility, $H$ is the magnetic field intensity, and $\mu_r$ is the relative permeability [39].
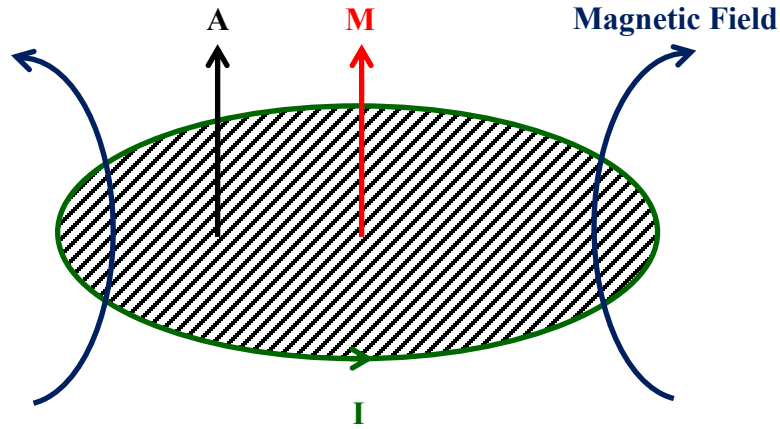


Figure 2.1 Inducing magnetic dipole moment on a current loop.

From the above equations, it is clear that one has to increase the magnetic dipole moment in order to increase the permeability. The increase in the magnetic dipole moment can be achieved by increasing the number of loops, the orbital current, or the loop area based on ( 2.1 ).

## 2.2    Artificial Magneto-dielectric Material

Since the key to successful induction of permeability is circulating currents, theoretically the magnetic behavior can be replicated in an otherwise non-magnetic material if such circulating currents can be created [28]. The geometry of the current carrier can be very flexible, as long as it is loop-like such that circulating currents can flow in it. A variety of such loops has been reported, such as split ring resonator (SRR), complementary split ring resonator (CSRR), multiple split ring resonator (MSRR), spiral resonator (SR), and extended split ring resonator [28] [40] [41]. Among these designs, the split ring resonator is the simplest and also the foundation of the other designs. Thus, it will be used as the design unit for the artificial magneto-dielectric material in this work. The effectiveness of such engineered high-permeability materials will be later verified and demonstrated through their capability of miniaturizing dielectric resonator antennas.

Figure 2.2 shows the front and side views of a split ring resonator unit cell. The ring, made of copper, is embedded in a low-permittivity dielectric material, Rogers RT/duroid 5880 ($\varepsilon_r = 2.2, \tan\delta = 0.0009$). According to ( 2.1 ), the permeability of such an SRR unit cell can be adjusted by varying the split ring parameters. However, it is worth mentioning that the equation ( $M = NIA$) can only be used to roughly estimate how the permeability may change with the ring parameters. In order to have a better understanding of the effects of each SRR unit cell parameter on material properties, parametric studies on the SRR unit cell are performed. The simulation is carried out in ANSYS HFSS, a finite element solver, for its powerful meshing and solver technologies [42]. The Maximum Delta S, namely the maximum change in the magnitude of the

S-parameters between two consecutive passes, is set to 0.01 [43]. The material properties are retrieved by using the S-parameter method given in [44] and [45]:

$$n = \frac{1}{kt} \cos^{-1}[\frac{1}{2S_{21}}(1 - S_{11}{}^2 + S_{21}{}^2)] \quad\quad (2.4)$$

$$z = \sqrt{\frac{(1 + S_{11})^2 - S_{21}{}^2}{(1 - S_{11})^2 - S_{21}{}^2}} \quad\quad (2.5)$$

$$\varepsilon = n/z \quad\quad (2.6)$$

$$\mu = n * z \quad\quad (2.7)$$

where $n$ is the refractive index, $z$ is the input impedance, $\varepsilon$ is the permittivity, $\mu$ is the permeability, $k$ is the wave number, $t$ is the unit cell thickness, $S_{11}$ is the reflection coefficient and $S_{21}$ is the transmission coefficient.

Here, the parameters of interest include the ring length ( $l$ ), unit cell length ( $a$ ), ring trace width ( $w$ ), ring gap width ( $g$ ), and spacing between adjacent ring layers/unit cell thickness ( $t$ ). Since the spacing between adjacent rings in the y-z plane will remain the same in this work, i.e. $a - l = 0.4\ mm$, the following study on the length of the ring is represented by the study on the length of the unit cell, $a$. Since the split rings will be evenly placed along the axis of the ring (x-axis), the study on the spacing between adjacent ring layers is represented by the study on the unit cell thickness, $t$.
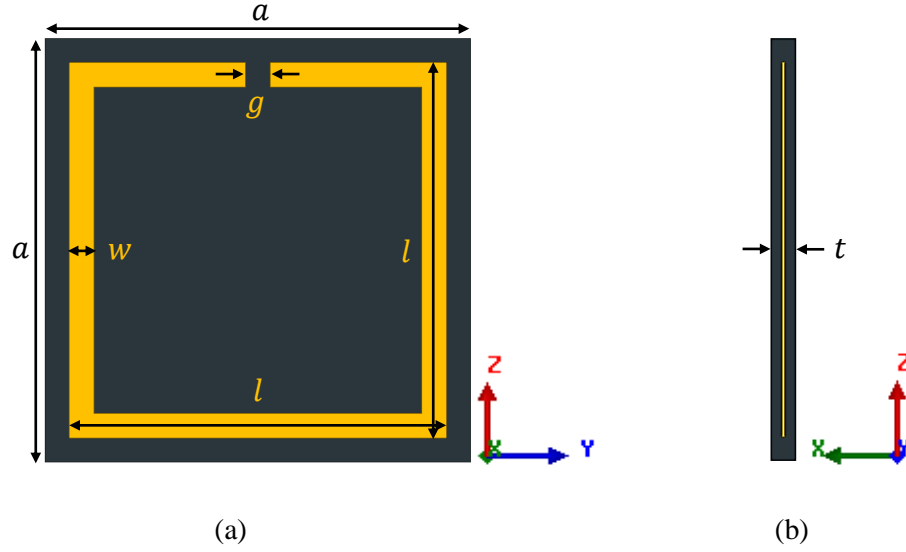
Figure 2.2 (a) The front view and (b) the side view of a split ring resonator unit cell. The orange is the split ring and the gray-blue is the supporting dielectric.

The results of the parametric studies on the SRR unit cells with varying parameters (see Table 2.1) are shown in Figure 2.3. Since the split rings are mainly responsible for inducing permeability, only the permeability curves are shown here. The two major characteristics of this engineered material, namely, peak permeability and resonant frequency, can be observed from the Frequency-Relative Permeability curves. The peak permeability simply means the strongest magnetic strength of the engineered material, while the resonant frequency indicates in which frequency range this material will be functioning [28].

Table 2.1 Ring Parameters for Split Ring Resonator Unit Cell Parametric Studies

| Para. Study on \ Para. | a (mm) | | | w (mm) | | | g (mm) | | | t (mm) | | |
|---|---|---|---|---|---|---|---|---|---|---|---|---|
| a | 2.5 | 3.0 | 3.5 | | 0.2 | | | 0.2 | | | 0.2 | |
| | 4.0 | 4.5 | 5.0 | | | | | | | | | |
| w | | 3.5 | | 0.2 | 0.4 | 0.6 | | 0.2 | | | 0.2 | |
| | | | | 0.8 | 1.0 | 1.2 | | | | | | |
| g | | 3.5 | | | 0.2 | | 0.2 | 0.7 | 1.2 | | 0.2 | |
| | | | | | | | 1.7 | 2.2 | 2.7 | | | |
| t | | 3.5 | | | 0.2 | | | 0.2 | | 0.2 | 0.7 | 1.2 |
| | | | | | | | | | | 1.7 | 2.2 | 2.7 |
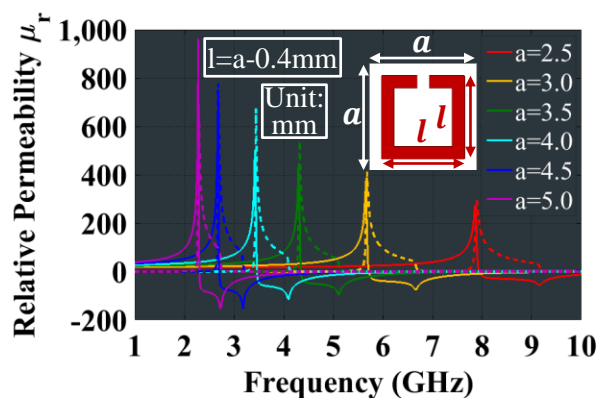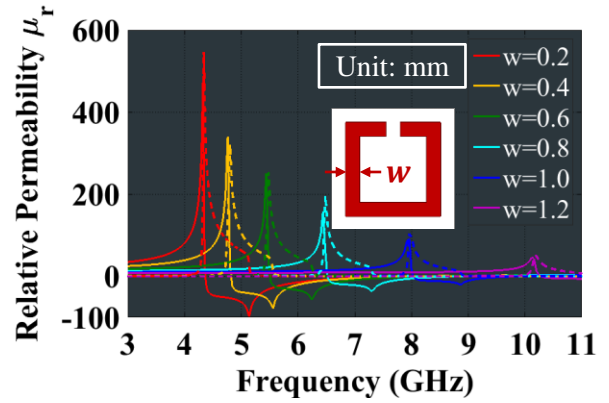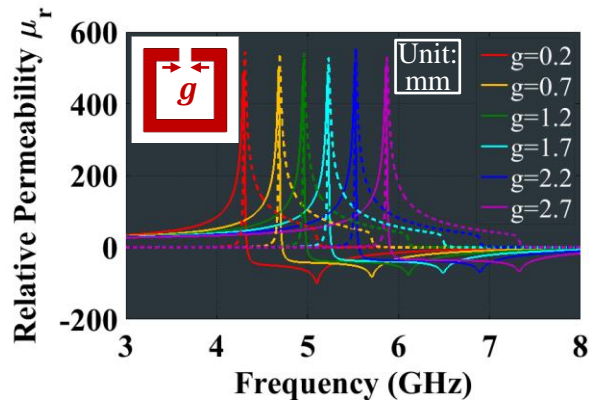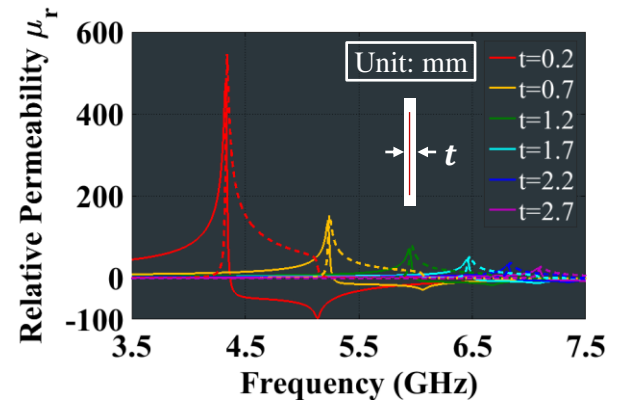


Figure 2.3 Permeability of split ring unit cells with (a) various unit cell length, $a$, (b) various ring trace width, $w$, (c) various ring gap width, $g$, and (d) various unit cell thickness, $t$. Solid curves: Real ($\mu_r$), Dashed curves: Imaginary ($\mu_r$). The inset in each figure is an SRR unit cell and the corresponding parameter studied is marked in each figure: the red and the white represent SRR and dielectric, respectively.

As can be seen, the variations in the ring length, $l$, width, $w$, and unit cell thickness, $t$, can lead to both frequency shifts and variations in the peak permeability, while the change in the ring gap, $g$, only has an impact on the resonant frequency of the SRR unit cell (Table 2.2). More detailed results corresponding to each unit cell parameter and brief explanations are given below.

Table 2.2 Effects of Unit Cell Length, Ring Trace Width, Ring Gap Width, and Unit Cell Thickness on the Resonant Frequency and Peak Permeability of the SRR Unit Cell

|  | a ↑ | w ↑ | g ↑ | t ↑ |
|---|---|---|---|---|
| $f_r$ | ↓ | ↑ | ↑ | ↑ |
| $\mu_r$ | ↑ | ↓ | − | ↓ |

As the unit cell length, $a$, (or ring length, $l$) increases, the resonant frequency shifts down and the peak permeability increases, as illustrated in Figure 2.3 (a), both of which are expected for the following two reasons:

- An increase in the physical length of the ring will lead to an increase in its electrical length and thus a reduced frequency ($a\uparrow \ \rightarrow l\uparrow \ \rightarrow \ f\downarrow$).

- A longer ring length also means a larger effective ring area, $A$, which is responsible for the increased peak permeability ($\mu = NIA$, $a\uparrow \ \rightarrow l\uparrow \ \rightarrow A\uparrow \ \rightarrow \ \mu\uparrow$).

On the contrary, an increase in the ring width, $w$, leads to an increased resonant frequency and reduced peak permeability (see Figure 2.3 (b)). The increase in the frequency is due to the decrease in the ring inductance as the ring becomes wider; and the decrease in the permeability is caused by the reduced effective ring area, $A$, as a result of increasing the ring width.

13

Varying the ring gap width, $g$, (Figure 2.3 (c)) modifies the resonant length of the ring and thus leads to a frequency shift, i.e. a larger gap means a shorter ring length and thus a higher resonant frequency. Since the variation in the ring gap does not have any effect on the factors that affect the permeability, the peak permeability remains constant as the ring gap varies, as expected.

Figure 2.3 (d) demonstrates the effects of the unit cell thickness, $t$, i.e. the spacing between adjacent SRR layers, on the material properties. As the unit cell thickness increases, an increase in the resonant frequency is observed. This is expected because the capacitance between SRR layers reduces as the SRR layers are placed farther apart from each other. The increase in the unit cell thickness also leads to a reduced number of unit cells per unit volume, $N$. As a result, the peak permeability decreases as the unit cell thickness increases, as observed.

Since the above parametric studies have proven that the material properties of such engineered high-permeability materials can be modified by varying the ring parameters, an antenna based on such materials should be able to achieve different miniaturization capabilities just by varying the ring parameters. For example, if a larger miniaturization capability is required, one can achieve it by increasing the ring length, reducing the ring width, reducing the gap width, and/or reducing the spacing between ring layers (i.e. unit cell thickness).

## 2.3   Magnetic Loss Mechanisms

### I. Loss Mechanisms in Natural Magnetic Materials

The losses in a magnetic material are mainly due to the hysteresis loss and eddy current loss [46] [47]. Unlike non-magnetic materials, magnetic materials (ferromagnetic materials) are non-linear and history-dependent, i.e. the magnetization is not only dependent on the applied magnetic field, but also dependent on the previous state of the material, as shown in Figure 2.4. The energy loss due to hysteresis in a magnetic cycle is determined by the area of the hysteresis loop: the smaller the area, the lower the loss [48]. Hysteresis loops (B-H curves) vary from material to material, and thus can be changed by modifying the material compositions, such as adding new elements to the materials or partially replacing elements in the materials [49] [50] [51]. The hysteresis loss can be expressed by [48] [52]

$$P_h = k_h B_{max}{}^{1.6} f V \qquad\qquad (\,2.8\,)$$

where $k_h$ is the Steinmetz hysteresis constant of the material, $B_{max}$ is the maximum magnetic flux density, $f$ is the frequency, and $V$ is the volume of the material. As can be seen from ( 2.8 ), the hysteresis loss is proportional to the operating frequency, which explains why the magnetic loss in natural magnetic materials is more significant at higher frequencies.
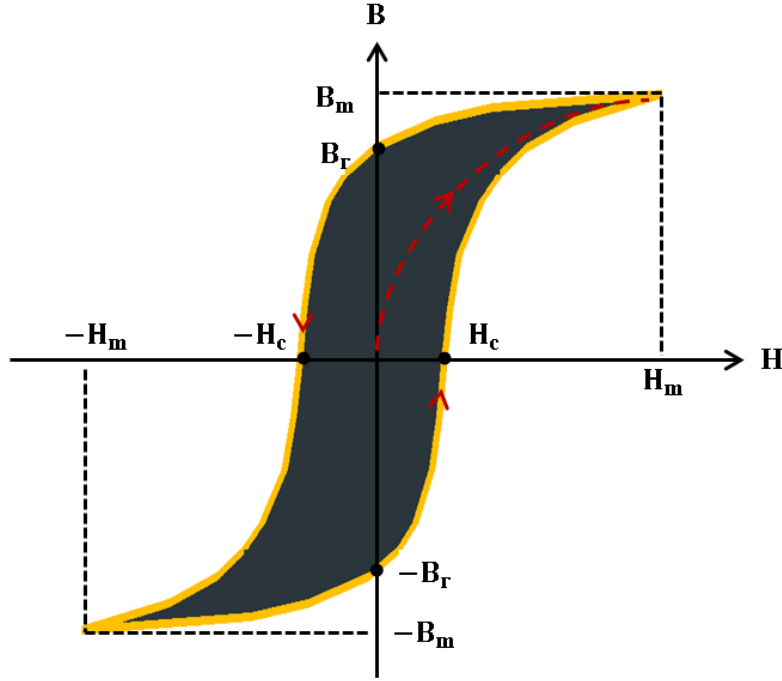
Figure 2.4 Hysteresis loop of a natural magnetic material. Plot data is from [53].

When an alternating magnetic field is applied to a magnetic material, alternating current loops (eddy currents) are induced in the material to create a magnetic field that opposes the original applied field according to Lenz's law. The eddy currents are responsible for the eddy current loss which can be expressed by the equation [54]

$$P_e = k_e B_{max}{}^2 f^2 V \qquad (2.9)$$

where $k_e$ is the eddy current coefficient, $B_{max}$ is the maximum flux density, $f$ is the frequency, and $V$ is the volume of the material. It is clear that the eddy current loss also increases with the increase in the frequency. A common way of reducing the eddy current loss is to use insulated laminations such that the eddy currents are restrained to only flow within each thin layer instead of the entire bulk material [55].

16

Although there are ways of reducing both hysteresis loss and eddy current loss and the usable frequencies for inherently magnetic materials have been moving up, pushing these natural magnetics to work efficiently at microwave frequencies is still considerably difficult and also technically demanding. Since the artificial magneto-dielectric material in this work does not contain any naturally occurring magnetics, the two loss mechanisms, i.e. hysteresis loss and eddy current loss, have been successfully avoided. However, dielectric and conductor losses are introduced in such an engineered material. In order to minimize the losses in an artificial magneto-dielectric material, a brief explanation on the two types of losses are given in the following section.

## II. Loss Mechanisms in Artificial Magneto-dielectric Materials

### i. Dielectric Loss

The polarization of electric dipoles in a dielectric is always trying to align with that of an applied alternating electric field. However, due to the non-zero imaginary part of the permittivity, the electric dipoles cannot keep up with the alternating electric field and such a phase lag will result in energy dissipation in the dielectric, i.e. dielectric loss [56] [57]. The dielectric loss per unit volume can be expressed by [57]

$$P_{diel} = \omega E^2 \varepsilon_0 \varepsilon_r'' = \omega E^2 \varepsilon_0 \varepsilon_r' tan\delta$$

( 2.10 )

where $\omega$ is the angular frequency, $E$ is the applied electric field, $\varepsilon_0$ is the permittivity of air, $\varepsilon_r'$ and $\varepsilon_r''$ are the real and imaginary parts of the relative permittivity of the dielectric material,

17

respectively, and $tan\delta = \frac{\varepsilon_r''}{\varepsilon_r'}$ is the dielectric loss tangent. It should be noted that existing dielectric materials with higher dielectric constants tend to have higher dielectric losses. Thus, in order to reduce the dielectric loss in the engineered material, a low-permittivity dielectric material should be used. Ideally, foam (air) is the best candidate, in terms of providing a low dielectric loss, due to its low permittivity ($\varepsilon_{r\_air} = 1$) and zero-loss tangent.

**ii. Conductor Loss**

In addition to the dielectric loss, conductor loss is another important form of energy dissipation in an artificial magneto-dielectric material, which can be expressed by

$$P_{cond} = P_{ac} = P_{dc} + P_{skin} + P_{prox}$$

( 2.11 )

$$P_{dc} = I^2 R_{dc} = I^2 \frac{\rho l}{A_{dc}}$$

( 2.12 )

$$P_{ac} = I^2 R_{ac} = I^2 \frac{\rho l}{A_{ac}}$$

( 2.13 )

where $P$, $R$ and $A$ are the power loss, resistance, and cross-sectional area of the conductor, respectively, and the subscripts *ac*, *dc*, *skin* and *prox* indicate alternating current, direct current, skin effect, and proximity effect. From ( 2.11 ), it is obvious that the AC conductor loss would be the same as the DC conductor loss (achievable minimum conductor loss) if the skin effect and proximity effect could be somehow eliminated. To do this, the skin effect and proximity effect will be briefly explained first.

As shown in Figure 2.5 (a) and (b), DC currents ($f = 0$ Hz) are uniformly distributed in a conductor, while AC currents only flow near the surface of the conductor at a certain depth ( skin depth, $\delta = \sqrt{\frac{1}{\pi f \mu \sigma}}$ ) and this phenomenon is called skin effect. Since the skin depth is inversely proportional to $\sqrt{f}$, the skin effect becomes more significant as the operating frequency increases. The skin effect is only destructive for those conductors with a thickness more than $2\delta$, because it essentially makes the inner part of the conductor useless, leading to a reduced effective cross-sectional area, $A_{ac}$, (the shaded red area in Figure 2.5 (b)) and an increased resistance, $R_{ac}$, and thus more power loss.



(a)                              (b)                              (c)
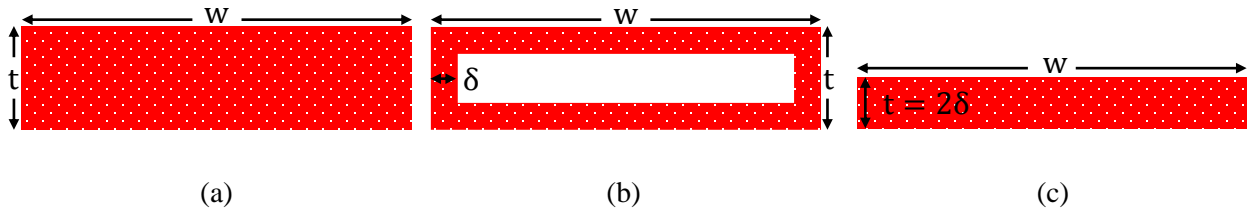
Figure 2.5 The current distribution on the cross-section of a rectangular conductor at (a) $f = 0$ Hz (DC current), (b) $f > 0$ Hz (AC current), $t > 2\delta$ and (c) $f > 0$ Hz (AC current), $t = 2\delta$. The currents mainly flow in the red zones.

The effective DC and AC cross-sectional areas of a rectangular conductor can be expressed by

$$A_{dc} = w * t \qquad\qquad (2.14)$$

$$A_{ac} = w * t - (w - 2\delta)(t - 2\delta) = 2\delta w + 2\delta t - 4\delta^2 \quad (t > 2\delta) \qquad (2.15)$$

$$A_{ac} = w * t \qquad\qquad (t \leq 2\delta) \qquad (2.16)$$

where $w$ and $t$ are the width and thickness of the conductor. For a conductor, made of a specific material and operating at a certain frequency, its skin depth is fixed and the only way to minimize the loss due to the skin effect is to optimize the geometry of the conductor to increase

19

its effective cross-sectional area. As can be seen from ( 2.15 ), the AC effective cross-sectional area can be increased by increasing the width and/or the thickness of the conductor. The above method applies when one chooses not to modify the configuration of the conductor, i.e. to maintain the structure of the single-layer conductor, and is able to increase the overall cross-sectional area of the conductor. On the other hand, if changing the configuration of the conductor is an option, such as using multi-layer conductor if it is a rectangular conductor or using Litz wire if it is a cylindrical conductor (i.e. splitting the conductor into multiple layers/strands of conductors with smaller cross-sectional area), the thickness of each single conductor should be at least reduced to $2\delta$ [58] [59] such that the currents are (near-) uniformly distributed across the cross-section of each conductor unit (Figure 2.5 (c)). By doing this, the same effective cross-sectional area as it is with DC currents can be achieved without increasing either the width or the thickness of the conductor. Finally, it is also worth mentioning that although a conductor with a thickness less than $2\delta$ does not suffer from skin effect, there is no benefit of reducing the conductor thickness to be less than $2\delta$ in terms of reducing conductor loss.

In addition to the skin effect, the proximity effect is another source of the AC conductor loss. When two or more conductors are closely placed, the electromagnetic interactions between neighboring conductors will change the current distribution in each individual conductor, causing uneven current distribution as shown in Figure 2.6. This effect, called proximity effect, is a function of frequency and spacing between conductors [60]. It causes the conductor to have a higher resistance because it reduces the effective size of the conductor by pushing currents to mainly flow in only one side of the conductor and, therefore, results in more power dissipation. The proximity effect can be reduced by increasing the ratio of the conductor spacing to the

thickness of the conductor, i.e. s/t [61]. Thus, one could either increase the spacing between conductors or reduce the thickness of the conductor to reduce the proximity effect.
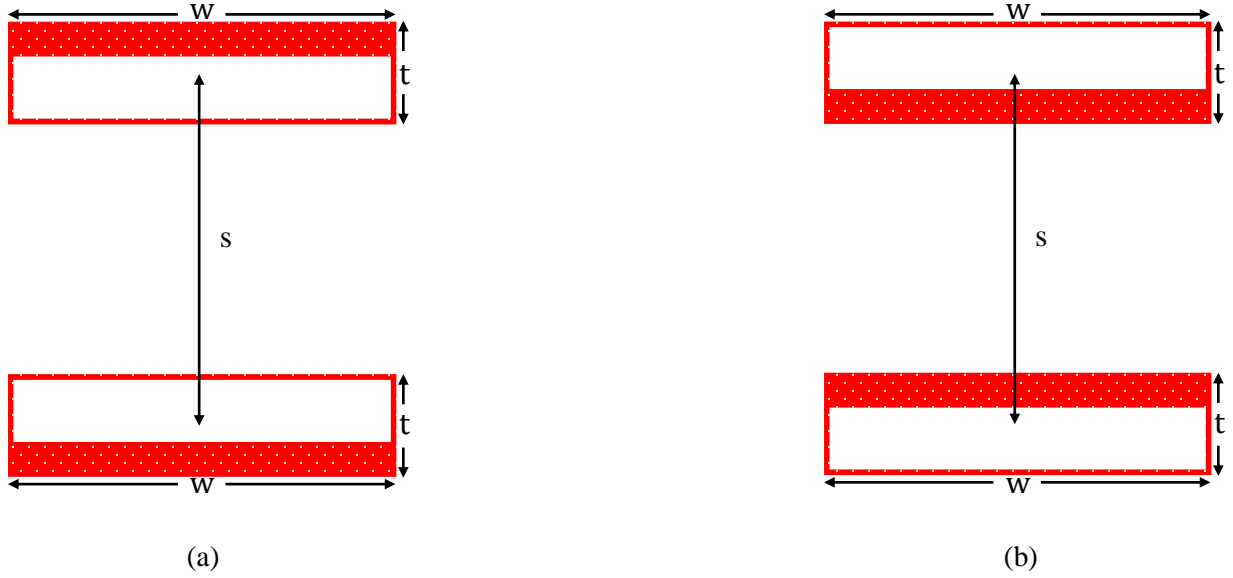


Figure 2.6 Proximity effect on the current distribution of two adjacent conductors when currents in two conductors are (a) in the same direction and (b) in the opposite direction [61].

## 2.4    Summary

The first section of this chapter discussed how to induce permeability in a non-magnetic material by replicating the magnetization mechanism of natural magnetic materials. The second section demonstrated the successful induction of permeability in a dielectric material by using split ring resonators. The parametric studies were performed, and the results showed that the material properties, such as permeability and resonant frequency of the engineered material, can be modified by adjusting the SRR unit cell parameters. The third section discussed the loss mechanisms in both natural magnetic materials and artificial magneto-dielectric materials. It was shown that the artificial magneto-dielectric materials do not replicate the loss mechanisms of the natural magnetic materials (i.e. hysteresis loss and eddy current loss) that are responsible for the

unacceptably high losses at higher frequencies; instead they have their own loss mechanisms, i.e. dielectric loss and conductor loss. The causes of the losses and possible ways of loss reduction in artificial magneto-materials were discussed.

Since such artificial magneto-dielectric materials can have high permeability and relatively low loss, they can be used for antenna miniaturization, especially in the microwave regime where natural magnetic materials are too lossy to be used. This will be demonstrated through the dielectric resonant antenna miniaturization in the following chapter.

# Chapter 3

# Split Ring Loaded Dielectric Resonator Antennas

Dielectric resonator antennas (DRAs) have been of great interest due to their relatively wide bandwidth and high radiation efficiency. A conventional DRA is made of a pure dielectric material and can be miniaturized by either increasing the permittivity or the permeability of the material. Just like any other miniaturized antenna, a miniaturized DRA also suffer from a deteriorated bandwidth and radiation efficiency. However, the degree of deterioration also varies with the method of miniaturization. It has been reported that high-permeability/magneto-dielectric materials ($\mu_r > 1$) are able to provide a wider bandwidth than their pure-dielectric counterparts ($\mu_r = 1$) while miniaturizing antennas [8] [9]. Although both natural and artificial magneto-dielectric materials can provide high permeability, the natural ones are too lossy to be used for low-loss microwave applications [7], such as antennas in this work. Therefore, using the engineered high-permeability materials to miniaturize DRAs seems to be a very promising and much needed approach.

In this chapter, a probe-fed rectangular dielectric resonator antenna based on the engineered magneto-dielectric material is proposed and investigated. The antenna is made of an array of split ring resonator unit cells that are arranged in such a way that the applied magnetic field aligns with the axes of the rings. The host dielectric resonator antenna (host DRA) can be of a very low permittivity or relatively high permittivity. In this work, a very low-permittivity dielectric material, Rogers RT/duroid 5880 with $\varepsilon_r = 2.2$ and $\tan\delta = 0.0009$, is used. As for the split ring resonator material, copper is chosen because it has good conductivity, is inexpensive, and is easy

to fabricate by using PCB fabrication techniques. In order to verify the miniaturization capability of the proposed antenna, an evaluation method is defined in the first section of this chapter. Unlike high-permittivity based DRAs, the low-permittivity dielectrics may not resonate or otherwise resonate at frequencies well above the resonant frequencies of their feeding probes. In other words, if a low-permittivity dielectric does resonate, the first observed resonance may not be from the DRA, instead it is from the feeding probe. Since the probe also has higher order modes at higher frequencies, it is more complicated to find the resonance from the host DRA. Although the resonance of the DRA can be differentiated by looking into radiation patterns, it may need to take a few tries to find it since it may not necessarily be the second, or third, or even fourth resonance depending on the dielectric constant and the dimensions of the DRA and the dimensions of the feeding probe. This makes the miniaturization capability evaluation of a low-permittivity based artificial magneto-dielectric resonator antenna (AMDRA) slightly more complicated than that of a high-permittivity based AMDRA. Both of the evaluation methods will be defined in the first section of this chapter. In the second section, artificial magneto-dielectric resonator antennas with split ring resonators of six different ring arrangements are investigated. Since the induced permeability is controlled by the ring parameters (see Section 2.2, Chapter 2), varying miniaturization capabilities should be expected from these six antennas. Parametric studies on the split rings, feeding probe, and ground plane are performed on one of the antennas to demonstrate how the antenna performance is affected by each part of the antenna, and thus to provide a general design guideline for such type of antennas. In order to experimentally verify the designs, a split ring loaded DRA is fabricated and tested in the final section of this chapter.

## 3.1 Miniaturization Capability Evaluation Methods

In this section, the miniaturization capability (MC) evaluation methods of both low and high-permittivity based AMDRAs are given. Since the first modes of both unloaded and loaded high-permittivity based DRAs are their first resonances, the miniaturization capability of a high-permittivity based AMDRA can be simply obtained by comparing the two resonances, which can be expressed as:

$$Miniaturization\ Capability\ = \frac{f_{r\_unloaded\ DRA}}{f_{r\_loaded\ DRA}} = \frac{f_{host\ DRA}}{f_{AMDRA}} \qquad (3.1)$$

where the subscripts *unloaded DRA* and *DRA* refer to the same thing, namely, the unloaded DRA, host DRA or host dielectric; the subscripts *loaded DRA* and *AMDRA* also refer to the same thing, namely, the split ring loaded DRA or artificial magneto-dielectric resonator antenna (AMDRA).

However, the first resonance of a very low permittivity based DRA is not necessarily its first mode, and thus, an extra procedure, namely comparing radiation patterns, is needed to be taken in order to first find the resonance of the DRA. This makes the traditional method of frequency comparison less convenient for these low-permittivity based DRAs. Therefore, a new evaluation method has to be developed specifically for the low-permittivity based AMDRAs.

In addition to comparing frequencies, miniaturization capability can also be obtained by comparing the refractive indices of the loaded and unloaded DRAs. Unlike the frequency comparison method, the refractive index comparison method needs a second reference antenna,

which in this case is an unloaded pure dielectric based equivalent high-ε DRA with the exact same dimensions and resonant frequency as the loaded DRA, in order to find the refractive index of the loaded antenna. More specifically, the refractive index of the loaded DRA, $n_{loaded\_DRA}$, is equal to the refractive index of the equivalent DRA, $n_{equivalent}$. And the equivalent refractive index is simply the square root of the equivalent permittivity, i.e. $n_{equivalent} = \sqrt{\varepsilon_{r\_equivalent}}$, in which the equivalent permittivity, $\varepsilon_{r\_equivalent}$, can be found by using the same simulation method, i.e. HFSS. Since the refractive index of the unloaded DRA is also known, i.e. $n_{unloaded\ DRA} = \sqrt{\varepsilon_{r\_host\ DRA}}$, the miniaturization capability can be easily determined by comparing the refractive indices of the loaded and unloaded DRAs. A more detailed procedure is given below:

$$\lambda \propto \frac{1}{\sqrt{\mu_r \varepsilon_r}} = \frac{1}{n} \tag{3.2}$$

$$f_{r\_loaded\ DRA} = f_{r\_equivalent\ DRA} \rightarrow \lambda_{loaded\ DRA} = \lambda_{equivalent\ DRA} \tag{3.3}$$

$$n_{loaded\ DRA} = n_{equivalent} = \sqrt{\varepsilon_{r\_equivalent} \cdot \mu_{r\_equivalent}} = \sqrt{\varepsilon_{r\_equivalent}} \tag{3.4}$$

$$n_{unloaded\ DRA} = \sqrt{\varepsilon_{r\_host\ DRA} \cdot \mu_{r\_host\ DRA}} = \sqrt{\varepsilon_{r\_host\ DRA}} \tag{3.5}$$

$$Miniaturization\ Capability = \frac{n_{loaded\ DRA}}{n_{unloaded\ DRA}} = \frac{\sqrt{\varepsilon_{r\_equivalent}}}{\sqrt{\varepsilon_{r\_host\ DRA}}} \tag{3.6}$$

where $\lambda$, $n$, $\varepsilon_r$, $\mu_r$, and $f_r$ are the wavelength, refractive index, relative permittivity, relative permeability and resonant frequency, respectively; the subscripts *unloaded DRA* and *host DRA* refer to the host dielectric (e.g. Rogers RT/duroid 5880 in this work), while *loaded DRA* refers to the SRR loaded DRA, and *equivalent DRA* refers to the unloaded equivalent high-

permittivity based DRA. It is worth mentioning that this evaluation method can also be used for miniaturization capability calculation of high-permittivity based AMDRAs.

To make the above discussion clearer, the parameters of the above antennas involved and the two evaluation methods are summarized in Table 3.1 and Table 3.2, respectively. $L$, $H$, and $W$ are the length, height, and width of the host DRA, respectively; $f_{r1}$, and $n_1$ are the resonant frequency and refractive index of the host DRA, and $f_{r2}$ and $n_2$ are the resonant frequency and refractive index of both the loaded DRA and the unloaded equivalent high-ε DRA.

Table 3.1 Antennas Involved for Miniaturization Capability Calculation of Both High and Low-permittivity Based AMDRAs

|  | Unloaded DRA or Host DRA | Loaded DRA or AMDRA | Equivalent High-ε DRA |
|---|---|---|---|
| **With SRRs** | No | Yes | No |
| **Dimensions** | L*H*W | L*H*W | L*H*W |
| **$f_r$** | $f_{r1}$ | $f_{r2}$ | $f_{r2}$ |
| **Refractive Index** | $n_1 = \sqrt{\varepsilon_{r\_host\ DRA}}$ | $n_2$ | $n_2 = \sqrt{\varepsilon_{r\_equivalent}}$ |

Table 3.2 Reference Antennas and Calculation Equations Used for High and Low-ε Host DRAs

|  | **High-ε Host DRA** | **Low-ε Host DRA** |
|---|---|---|
| **Reference Antenna(s)** | Host DRA | Host DRA & Equivalent High-ε DRA |
| **Miniaturization Capability** | $\dfrac{f_{r\_host\ DRA}}{f_{r\_loaded\ DRA}}$ | $\dfrac{\sqrt{\varepsilon_{r\_equivalent}}}{\sqrt{\varepsilon_{r\_host\ DRA}}}$ |

## 3.2    Dielectric Resonator Antennas with Split Rings of Different Arrangements

The idea of loading a dielectric resonator antenna with split rings is to try to miniaturize the antenna by inducing an artificial permeability in the host dielectric. Since the induced permeability is a function of the number, $N$, current, $I$, and effective area, $A$, of split rings, any changes in these three factors will affect the antenna performance. However, two of the above parameters, namely the number of rings, $N$, and the effective ring area, $A$, counterbalance each other in a size-fixed host DRA. In other words, one can either have more rings in a smaller size or fewer rings in a larger size, but cannot have both at the same time. Therefore, it is important to find a good balance between them when designing such antennas in order to achieve the desired antenna performance. This issue can be easily investigated by loading the same host DRA, as illustrated in Figure 3.1, with split rings of different arrangements. The dielectric dimensions, material properties, and the feeding probe dimensions are given in Table 3.1. The length, width, and height of the host DRA are 15 mm, 0.254 mm and 7.5 mm, respectively. Since the height of the probe and the size of the ground plane will have some effect on the antenna performance, their dimensions cannot be determined at this stage and will be investigated later in this chapter.
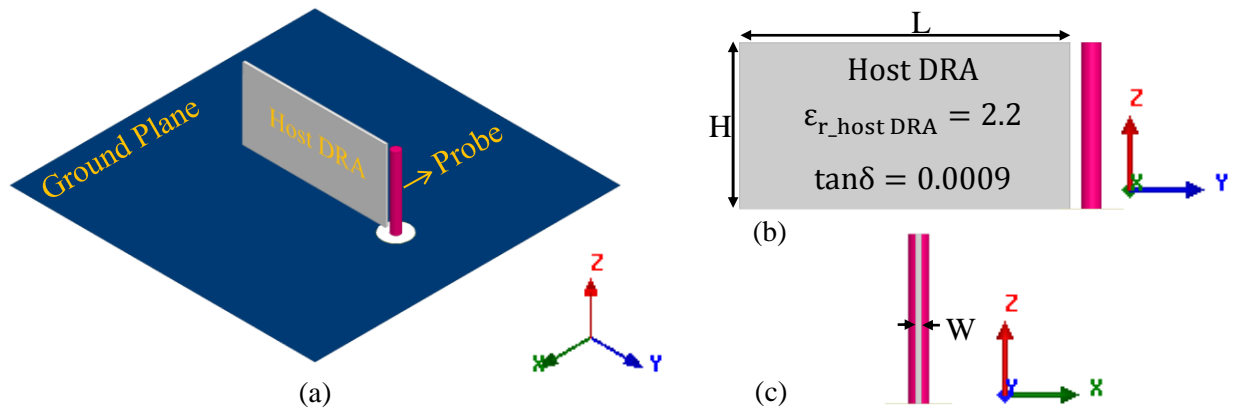


Figure 3.1 (a) 3-D view of a probe-fed host DRA placed on a square copper ground plane. (b) Front and (c) left side views of the host DRA (ground plane not shown in (b) and (c)).

Table 3.3 Parameters of the Host Dielectric Resonator Antenna

| DRA Dimensions (mm) | | | Probe Dimensions (mm) | | DRA Material | | |
|---|---|---|---|---|---|---|---|
| L | H | W | Pin Radius | Port Radius | $\varepsilon_{r\,host\,DRA}$ | $\mu_{r\,host\,DRA}$ | tanδ |
| 15 | 7.5 | 0.254 | 0.625 | 2 | 2.2 | 1 | 0.0009 |

In order to maximize the electromagnetic interaction between the split rings and the applied magnetic field, the axes of the rings have to be aligned with the magnetic field [7]. Since the magnetic field of the host DRA is along the x-axis, as shown in Figure 3.2 (b), the rings should be placed in the y-z plane. By varying the dimensions of the split rings, numerous ring arrangements can be obtained, six of which, as listed in Table 3.4, will be investigated. To simplify the analysis, the ring arrangement along the x-axis remains the same, and only varies in the y-z plane. In this study, a 3-layer configuration (i.e. $3\vec{x}$) is used, and these three identical layers of SRRs are place on the front, center, and back surfaces of the host DRA. For the sake of convenience, the six ring arrangements will be referred to as: $3\vec{x} \times 3\vec{y} \times 3\vec{z}$, $3\vec{x} \times 3\vec{y} \times 2\vec{z}$, $3\vec{x} \times 3\vec{y} \times 1\vec{z}$, $3\vec{x} \times 2\vec{y} \times 2\vec{z}$, $3\vec{x} \times 2\vec{y} \times 1\vec{z}$, and $3\vec{x} \times 1\vec{y} \times 1\vec{z}$, in which the numbers represent the number of split rings in three specific directions, namely, x-axis ($\vec{x}$), y-axis ($\vec{y}$), and z-axis ($\vec{z}$). The dimensions of the split ring unit cell in each arrangement are given in Table 3.2, which are calculated by using the following equations:

$$L = 15\ mm,\ H = 7.5\ mm \rightarrow L = 2H \qquad (3.7)$$

$$N_L = \frac{L}{L_{unit\ cell}}, N_H = \frac{H}{H_{unit\ cell}} \qquad (3.8)$$

$$\frac{N_L}{N_H} = \frac{L}{L_{unit\ cell}}\frac{H_{unit\ cell}}{H} = 2\frac{H_{unit\ cell}}{L_{unit\ cell}} \qquad (3.9)$$

29

$$N_L:N_H = 3:3, 2:2, \text{ and } 1:1 \rightarrow L_{unit\ cell} = 2H_{unit\ cell} \qquad (3.10)$$

$$N_L:N_H = 3:2 \rightarrow L_{unit\ cell} = \frac{4}{3}H_{unit\ cell} \qquad (3.11)$$

$$N_L:N_H = 3:1 \rightarrow L_{unit\ cell} = \frac{2}{3}H_{unit\ cell} \qquad (3.12)$$

$$N_L:N_H = 2:1 \rightarrow L_{unit\ cell} = 1H_{unit\ cell} \qquad (3.13)$$

$$s = 0.4\ mm \qquad (3.14)$$

$$L_{SRR} = L_{unit\ cell} - s \qquad (3.15)$$

$$H_{SRR} = H_{unit\ cell} - s \qquad (3.16)$$

where $N_L$ and $N_H$ are ring numbers along the y and z-axes, respectively, $s$ is the spacing between adjacent split rings in the y-z plane. $L_{SRR}$ and $L_{unit\ cell}$ are the lengths of the split ring resonator (SRR) and SRR unit cell along the y-axis, respectively, and $H_{SRR}$ and $H_{unit\ cell}$ are the heights of the SRR and SRR unit cell along the z-axis, respectively.



(a)            (b)
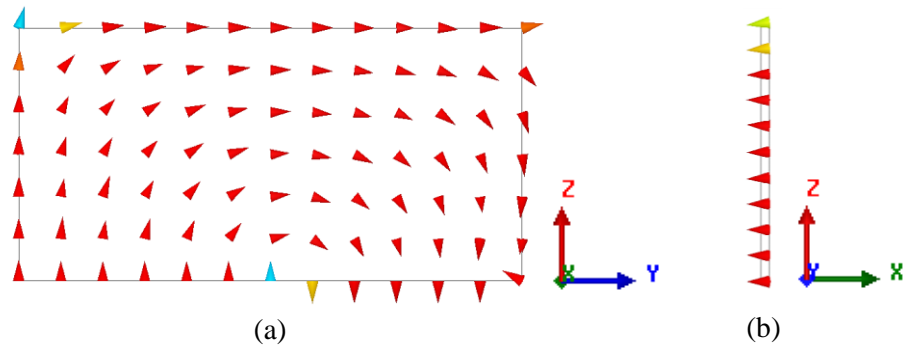
Figure 3.2 Field distribution in the host DRA: (a) Electric field, and (b) magnetic field. Notice that the magnetic field, i.e. H-field, is along the x-axis.

Table 3.4 Split Ring Arrangements and the Corresponding SRR Unit Cell Dimensions

| Arrangement | Geometry (Front View) | $L_{unit\ cell}$ (mm) | $H_{unit\ cell}$ (mm) | $L_{SRR}$ (mm) | $H_{SRR}$ (mm) | N*A (mm$^2$) | $C_{SRR}$ (mm) |
|---|---|---|---|---|---|---|---|
| $3\vec{y} \times 3\vec{z}$ | | 5 | 2.5 | 4.6 | 2.1 | 225.72 | 12.4 |
| $3\vec{y} \times 2\vec{z}$ | | 5 | 3.75 | 4.6 | 3.35 | 249.48 | 14.9 |
| $3\vec{y} \times 1\vec{z}$ | | 5 | 7.5 | 4.6 | 7.1 | 273.24 | 22.4 |
| $2\vec{y} \times 2\vec{z}$ | | 7.5 | 3.75 | 7.1 | 3.35 | 260.82 | 19.9 |
| $2\vec{y} \times 1\vec{z}$ | | 7.5 | 7.5 | 7.1 | 7.1 | 285.66 | 27.4 |
| $1\vec{y} \times 1\vec{z}$ | | 15 | 7.5 | 14.6 | 7.1 | 298.08 | 42.4 |

The miniaturization capability is controlled by two parameters of the unit cell, namely, the peak relative permeability and the resonant frequency of the unit cell. The resonant frequency roughly sets the operating frequency range of the material [28], and the peak relative permeability simply determines how strong the magnetic strength of the material is. In order to improve the miniaturization capability, one should either reduce the resonant frequency of the unit cell or increase the peak relative permeability of the unit cell, or preferably both.

The resonant frequency of the unit cell is inversely proportional to the circumference of the split ring. And the peak relative permeability, as stated in Chapter 2, is proportional to the product of the ring number, current, and effective ring area, *NIA*. Since the width of the rings in different arrangements remains the same, i.e. $w = 0.2\ mm$, the current could be assumed to be approximately the same in all six cases, which means the only term that makes a difference in the peak relative permeability of the engineered materials with different ring arrangements is *NA*. As can be seen from Table 3.4, both the term *NA* and the circumference of the SRR, $C_{SRR}$, vary with the ring arrangement, which means both the resonant frequency and the peak relative permeability of the unit cell vary with the ring arrangement. By varying the ring arrangement, both the resonant frequency of the unit cell and the peak relative permeability can be changed. More specifically, as the ring arrangement changes from $3\vec{x} \times 3\vec{y} \times 3\vec{z}$, $3\vec{x} \times 3\vec{y} \times 2\vec{z}$, $3\vec{x} \times 3\vec{y} \times 1\vec{z}$, $3\vec{x} \times 2\vec{y} \times 2\vec{z}$, $3\vec{x} \times 2\vec{y} \times 1\vec{z}$, to $3\vec{x} \times 1\vec{y} \times 1\vec{z}$, the resonant frequency, $f_{uc}$, and the peak relative permeability, $\mu_r$, of the unit cell follow the following sequential orders, respectively:

$$f_{uc\_3\vec{x}\times3\vec{y}\times3\vec{z}} > f_{uc\_3\vec{x}\times3\vec{y}\times2\vec{z}} > f_{uc\_3\vec{x}\times2\vec{y}\times2\vec{z}} > f_{uc\_3\vec{x}\times3\vec{y}\times1\vec{z}} > f_{uc\_3\vec{x}\times2\vec{y}\times1\vec{z}} > f_{uc\_3\vec{x}\times1\vec{y}\times1\vec{z}}$$

$$\mu_{r\_3\vec{x}\times3\vec{y}\times3\vec{z}} < \mu_{r\_3\vec{x}\times3\vec{y}\times2\vec{z}} < \mu_{r\_3\vec{x}\times2\vec{y}\times2\vec{z}} < \mu_{r\_3\vec{x}\times3\vec{y}\times1\vec{z}} < \mu_{r\_3\vec{x}\times2\vec{y}\times1\vec{z}} < \mu_{r\_3\vec{x}\times1\vec{y}\times1\vec{z}}.$$

Therefore, the miniaturization capabilities (MCs) of the antennas with the six ring arrangements should be in the order of:

$$MC_{3\vec{x}\times3\vec{y}\times3\vec{z}} < MC_{3\vec{x}\times3\vec{y}\times2\vec{z}} < MC_{3\vec{x}\times2\vec{y}\times2\vec{z}} < MC_{3\vec{x}\times3\vec{y}\times1\vec{z}} < MC_{3\vec{x}\times2\vec{y}\times1\vec{z}} < MC_{3\vec{x}\times1\vec{y}\times1\vec{z}},$$

which will be verified later in this chapter through simulations.

### 3.2.1   Dielectric Resonator Antenna with $3\vec{x} \times 3\vec{y} \times 3\vec{z}$ Split Rings

The dielectric resonator antenna with $3\vec{x} \times 3\vec{y} \times 3\vec{z}$ split rings is shown in Figure 3.3. The three layers of SRRs are placed on the back, center, and front of the host DRA, respectively. Each layer consists of $3\vec{y} \times 3\vec{z}$ SRRs that are made of copper. In order to investigate the effect of SRR parameters on the performance of the loaded DRA, DRAs with various SRR trace widths and gap widths are studied. As previously discussed, the axes of the split rings should be in the same direction as the magnetic field in order to obtain the maximum electromagnetic induction. However, for a split ring with fixed axis, there are numerous possibilities for its gap (slit) position. Due to the asymmetry of the gap position with respect to the probe and ground plane, the gap position might have an effect on antenna performance. Therefore, antennas with various gap positions are also studied. Moreover, since the antenna is capacitively coupled to the feeding probe, the height of the probe might also have an effect on antenna performance. Thus, antennas with different probe heights are also investigated. All the simulations involved in the following context are carried out in ANSYS HFSS with the Maximum Delta S set to 0.02.

(a)

(b)

**Slit Position: -Z**

$L_{SRR}$

$H_{SRR}$

w

g

H

L

$h_{probe}$

(c)
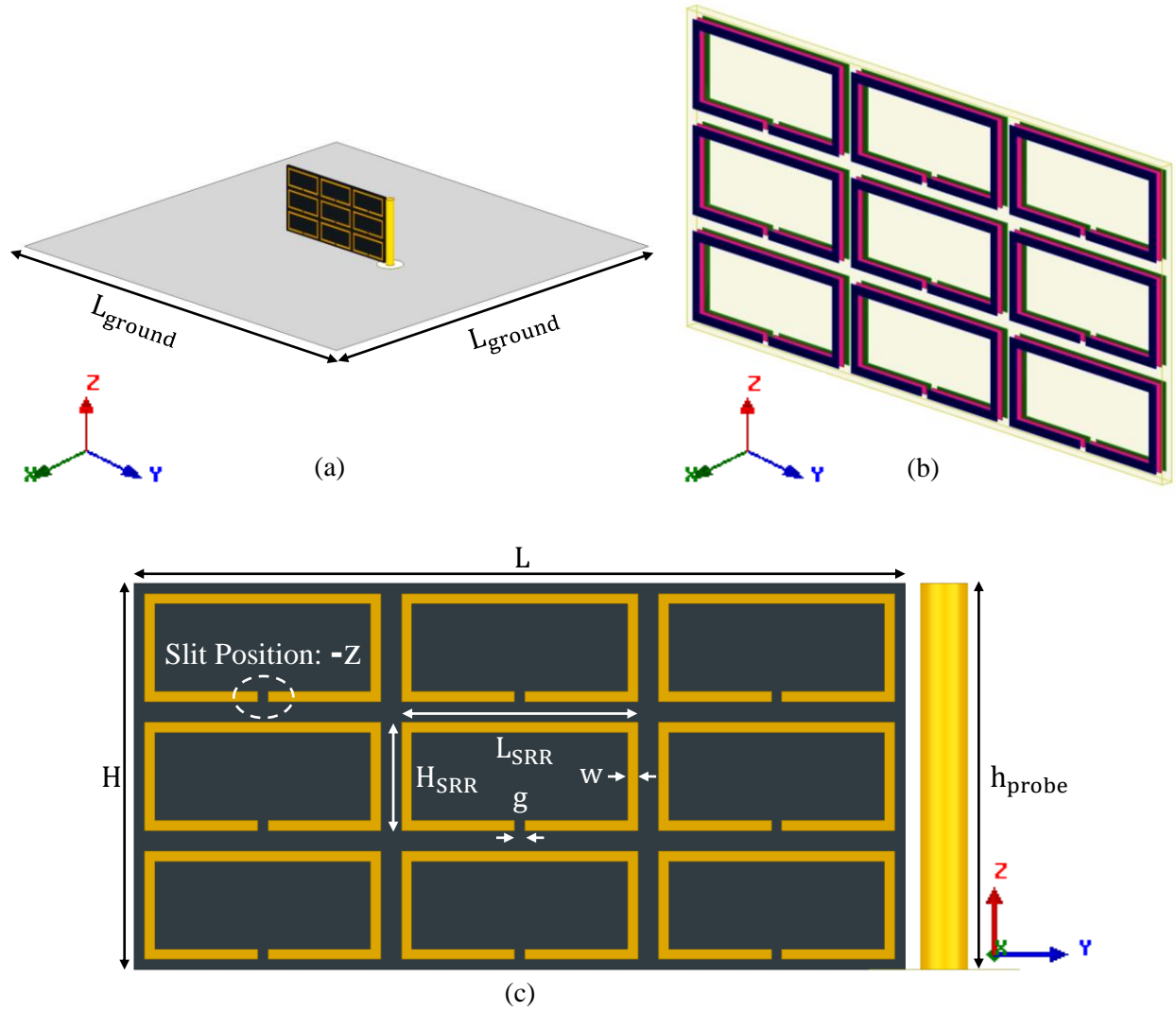
Figure 3.3 (a) 3-D view of a dielectric resonator antenna with $3\vec{x} \times 3\vec{y} \times 3\vec{z}$ split rings (█ Host DRA; █ SRRs and Probe; █ Ground Plane). (b) Zoomed-in view of the ring arrangement in the host DRA (different colors are used to demonstrate different layers of SRRs). The three identical layers of SRRs are placed on the front (█ navy), center (█ pink), and back (█ green) surfaces of the host DRA. (c) Zoomed-in front view of the SRR loaded DRA with dimensions as marked.

## I. Parametric Study on the Probe Height

The proposed antenna can be matched by adjusting the probe height and the spacing between the probe and the antenna. An increase in the height of the probe leads to more resistance and

inductance, which can be counterbalanced by increasing the spacing between the probe and the antenna, and vice versa. In order to investigate the effect of the probe height, an antenna with three different probe heights, i.e. $h_{probe} = 5.5$ mm, $h_{probe} = 6.5$ mm and $h_{probe} = 7.5$ mm, is studied. The dimensions of the antenna are given in Table 3.5.

Table 3.5 Antenna Parameters for Probe Height Study

| SRR Arrangement | Host DRA (mm) | | | SRR (mm) | | | | Slit Position | $h_{probe}$ (mm) |
|---|---|---|---|---|---|---|---|---|---|
| | W | H | L | $L_{SRR}$ | $H_{SRR}$ | w | g | | |
| $3\vec{x} \times 3\vec{y} \times 3\vec{z}$ | 15 | 7.5 | 0.254 | 4.6 | 2.1 | 0.2 | 0.2 | -z | 5.5, 6.5, 7.5 |

The performance of the antenna with various probe heights is given in Table 3.6 and the radiation patterns are shown in Figure 3.4. It shows that an increase in the probe height can result in more size reduction and much wider bandwidth, however, at the expanse of a reduced directivity and increased cross-polarization. For example, by increasing the probe height, $h_{probe}$, from 5.5 mm to 7.5 mm, the resonant frequency of the antenna shifts down by 0.218 GHz and the bandwidth increases by 2.85%, but the gain drops by 1.51 dB and the cross-polarization increases by 5.45 dB. High cross-polarization is always unwanted and low directivity can be desirable or undesirable depending on applications:

- Low directivity is desirable in mobile applications where the relative position of transmitters and receivers is uncertain and changing. However, for point to point applications where the relative position of transmitters and receivers is stable, an antenna with high directivity is preferred.

- The cross-polarization level, the difference between the intended antenna polarization, i.e. co-polarization, and the orthogonal polarization to the co-polarization, is a measure of the polarization purity of an antenna [62]. The higher the cross-polarization level, the worse the polarization isolation. In order to reduce the interference from the unwanted signals, high polarization isolation is needed, especially for applications that use dual-polarization communication techniques, such as MIMO (Multiple Input Multiple Output) and satellite antennas [62] [63]. Thus, for such applications, the challenge at this stage is to resolve the issue of low directivity and high cross-polarization while maintaining the wide bandwidth and compactness.

The antenna in this work is aimed to work as a directional antenna, instead of an omnidirectional antenna. But compactness and wide bandwidth are also preferred. Therefore, the probe height of 7.5 mm will be used for the following antenna designs, and the challenge at this stage is to improve the gain and reduce the cross-polarization.

Table 3.6 Antenna Performance vs. Probe Heights (only H-plane peak X-pol level is shown because E-plane X-pol level is below -50 dB for all three probe heights and thus not of interest)

| $h_{probe}$ (mm) | $f_r$ (GHz) | BW (%) | η (%) | Gain (dBi) | Peak X-pol (dB) | Dir (dBi) |
|---|---|---|---|---|---|---|
| 5.5 | 7.073 | 8.24 | 97.57 | 6.60 | -12.32 | 6.71 |
| 6.5 | 6.961 | 10.31 | 98.34 | 5.89 | -9.37 | 5.97 |
| 7.5 | 6.855 | 11.09 | 99.15 | 5.09 | -6.87 | 5.13 |
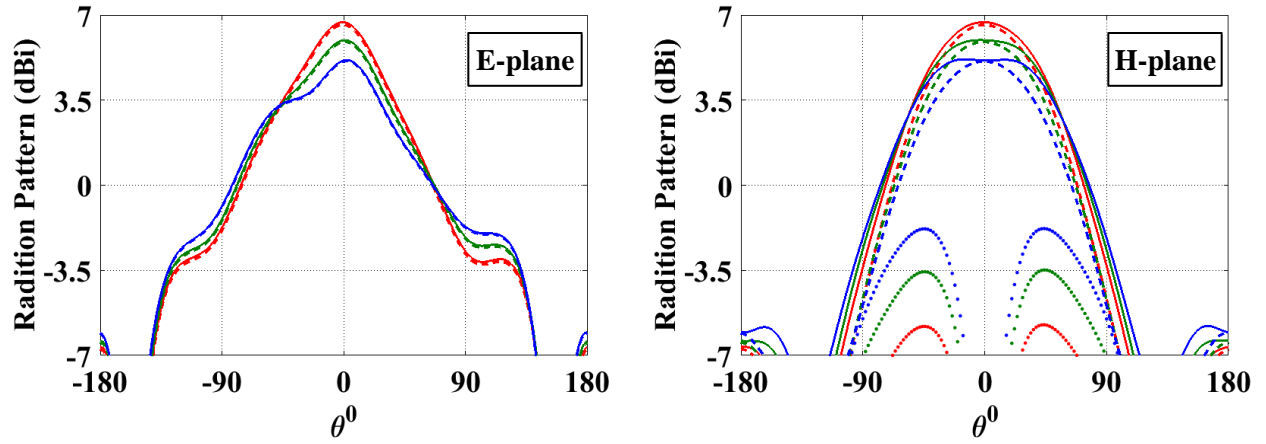
Figure 3.4 E and H-plane radiation patterns of the $3\vec{x} \times 3\vec{y} \times 3\vec{z}$ SRR loaded DRA with various probe heights: $h_{probe}$ = 5.5 mm, 6.5 mm and 7.5 mm. Dir, Co-pol, and X-pol refer to directivity, co-polarization and cross-polarization, respectively. E-plane cross-polarizations are well below -40 dBi, so they are not visible in the plot.

## II. Parametric Study on the Ground Plane

### i. Effect of the Side Wall Height

In [64], a U-shaped ground plane is reported to be able to reduce the cross-polarization and increase the directivity of a patch antenna. It is worth noting that the bent vertical plates of the U-shaped ground plane have to be placed on the two radiating edges of the ground plane for this technique to work [64]. In order to verify if this technique can be applied to a split ring loaded dielectric resonator antenna, the conventional planar square ground plane, as shown in Figure 3.5 (a), of the proposed antenna is replaced by a U-shaped ground plane (Figure 3.5 (b)). Different side wall heights will be investigated in order to find out the effect of the side wall height on the antenna performance. The parameters of the antenna used for the U-shaped ground plane study are given in Table 3.7.

37
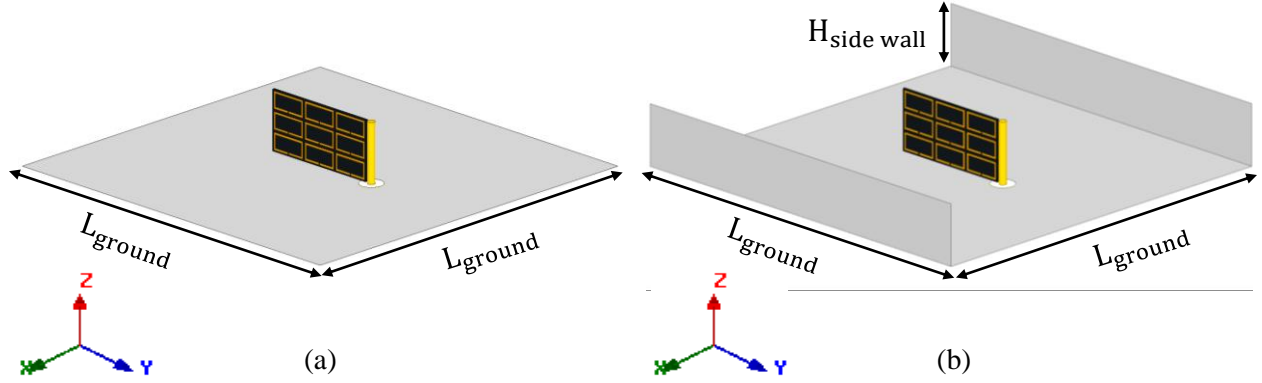
Figure 3.5 The split ring loaded dielectric resonator antenna with a (a) conventional planar ground plane and (b) U-shaped ground plane.

Table 3.7 Antenna Parameters for U-shaped Ground Plane Study

| SRR Arrangement | Host DRA (mm) | | | SRR (mm) | | | | Slit Position | $h_{probe}$ (mm) | $H_{side\ wall}$ (mm) |
|---|---|---|---|---|---|---|---|---|---|---|
| | W | H | L | $L_{SRR}$ | $H_{SRR}$ | w | g | | | |
| $3\vec{x} \times 3\vec{y} \times 3\vec{z}$ | 15 | 7.5 | 0.254 | 4.6 | 2.1 | 0.2 | 0.2 | -z | 7.5 | 5, 7.5, 10, 12.5, 15 |

The performance of the split ring loaded antenna with U-shaped ground planes of various side wall heights, $H_{side\ wall}$, is shown in Table 3.8. It is obvious that both directivity and gain increase, and the cross-polarization decreases with the increase in the side wall height with an upper limit of 15 mm (~0.349λ) (Figure 3.6). However, a further increase in the side wall height beyond 15 mm leads to an increase in the cross-polarization level, and decrease in the gain and cross-polarization. From a conventional planar ground plane ($H_{side\ wall} = 0$) to a U-shaped ground plane of $H_{side\ wall} = 15$ mm, both directivity and gain increase by around 2.7 dB, while the cross-polarization decreases by 10.25 dB. More importantly, such an improvement is achieved with only 0.38% bandwidth drop and 1.74% resonant frequency shift.

Table 3.8 Antenna Performance vs. U-shaped Side Wall Heights

| $L_{ground}$ (mm) | $H_{side\ wall}$ (mm) | $H_{side\ wall}$ /λ | $f_r$ (GHz) | BW (%) | η (%) | Gain (dBi) | X-pol (dB) | Dir (dBi) |
|---|---|---|---|---|---|---|---|---|
| 48 | 0 | 0 | 6.8550 | 11.09 | 99.15 | 5.09 | -6.87 | 5.13 |
| 48 | 5.0 | 0.116 | 6.8985 | 11.24 | 98.59 | 5.99 | -9.39 | 6.05 |
| 48 | 7.5 | 0.173 | 6.9243 | 11.22 | 98.55 | 6.63 | -11.53 | 6.69 |
| 48 | 10.0 | 0.231 | 6.9426 | 11.08 | 98.52 | 7.22 | -14.12 | 7.29 |
| 48 | 12.5 | 0.290 | 6.9568 | 10.91 | 98.36 | 7.56 | -16.20 | 7.64 |
| 48 | 15.0 | **0.349** | 6.9743 | 10.71 | 98.33 | 7.77 | -17.12 | 7.85 |
| 48 | 17.5 | 0.407 | 6.9812 | 10.57 | 98.20 | 7.78 | -17.01 | 7.86 |
| 48 | 20.0 | 0.465 | 6.9759 | 10.38 | 98.34 | 7.72 | -16.24 | 7.79 |
| 48 | 22.5 | 0.524 | 6.9814 | 10.19 | 98.35 | 7.50 | -15.16 | 7.57 |



| $H_{side\ wall}$ | 0 mm | 5 mm | 7.5 mm | 10 mm | 12.5 mm | 15 mm |
|---|---|---|---|---|---|---|
| Directivity | —— | —— | —— | —— | —— | —— |
| Co-pol | - - - - | - - - - | - - - - | - - - - | - - - - | - - - - |
| X-pol | ● | ● | ● | ● | ● | ● |
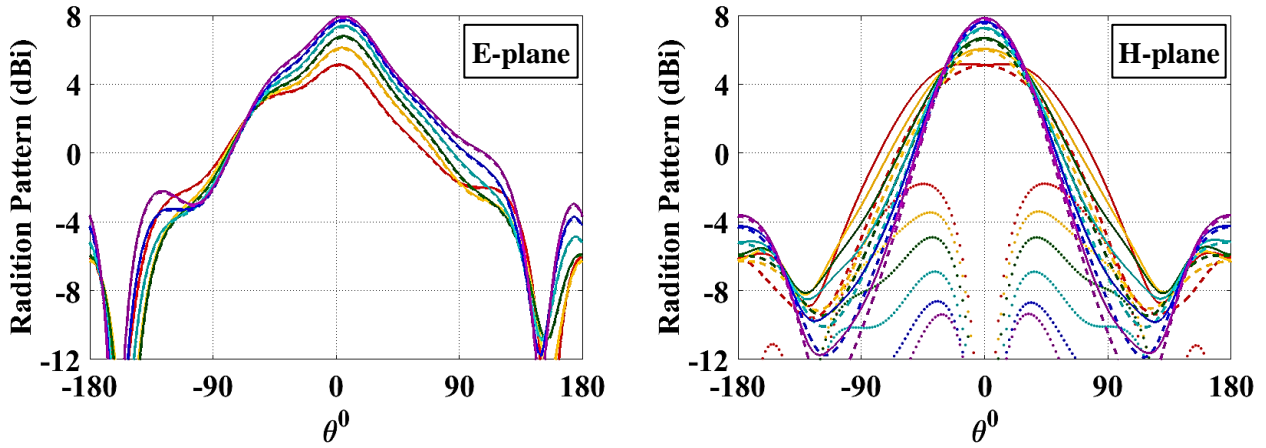
Figure 3.6 E and H-plane radiation patterns of the $3\vec{x} \times 3\vec{y} \times 3\vec{z}$ SRR loaded DRA with U-shaped ground planes of various side wall heights: $H_{side\ wall}$ = 0 mm, 5 mm, 7.5 mm, 10 mm, 12.5 mm, and 15 mm. E-plane cross-polarizations are not visible in the plot because they are below -40 dBi at all side wall heights.

In order to investigate the reason behind such an improvement, current distributions on both conventional and U-shaped ground planes are plotted in Figure 3.7. Since the antenna is y-polarized, the cross-polarization is mainly caused by the x-directed current component [62]. It is worth noticing that the current distribution on the horizontal part of the U-shaped ground plane (x-y plane) is almost the same as that of the conventional ground plane. Thus, the polarization improvement is due to the additional currents on the two side walls. As demonstrated in Figure 3.7 (b1), the currents on the side walls only have $\hat{\imath}_y$ and $\hat{\imath}_z$ components, which is also expected because the side walls are placed in the y-z plane. And the y-directed currents are the ones responsible for the co-polarized radiation, while the z-directed currents have little negative compact on the cross-polarization.
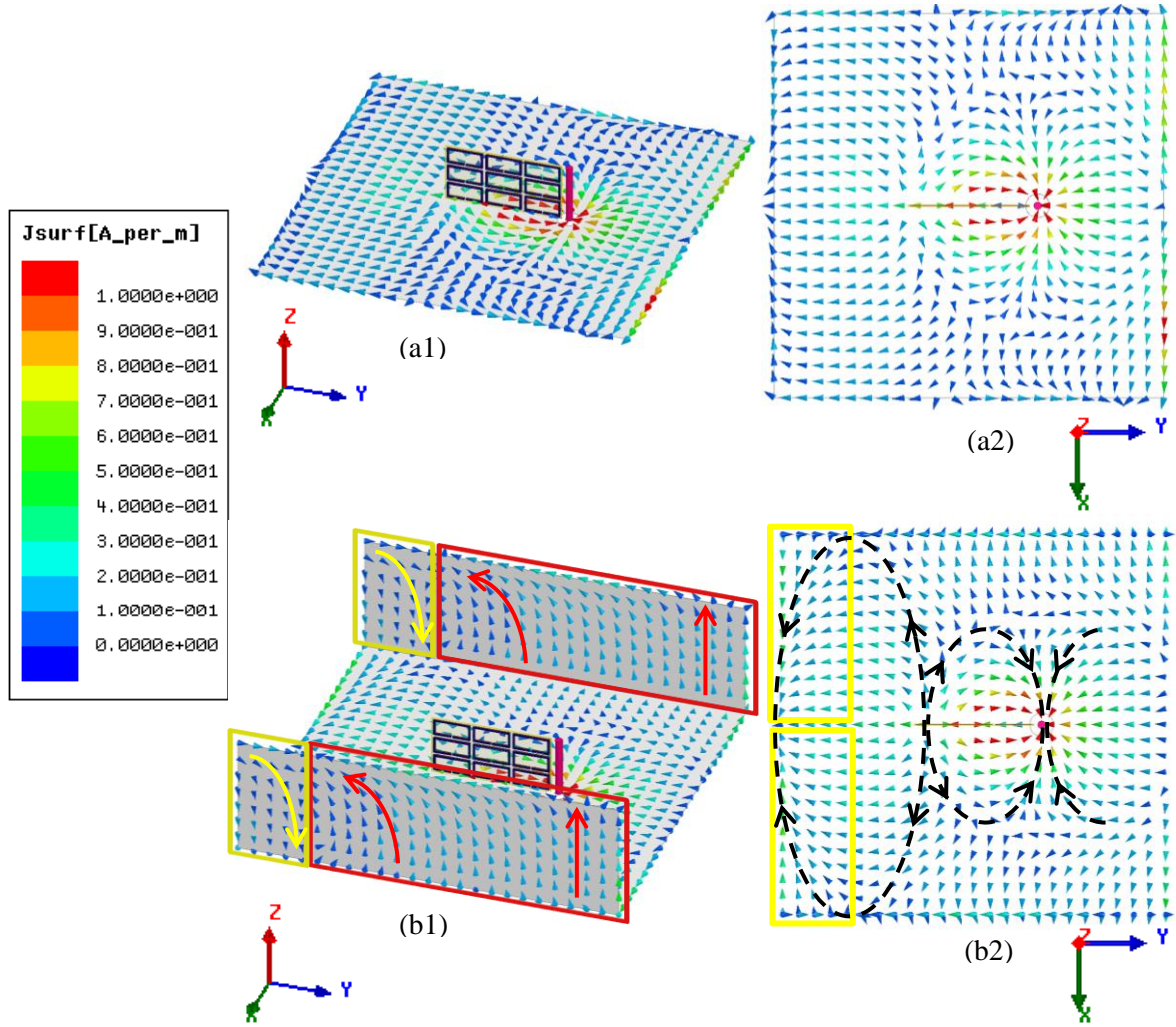
Figure 3.7 Current distributions on the (a) conventional ground plane and (b) U-shaped ground plane. (a1) and (b1) are 3-D views, and (a2) and (b2) are top views. The color key is the same in both cases.

## ii. Effect of the Ground Plane Length

In addition to the height of the side walls, the effect of the length of the ground plane, $\mathbf{L_{ground}}$, is also investigated. Here the ground plane length is varied from 36 mm * 36 mm (~0.79λ * 0.79λ) to 60 mm * 60 mm (~1.40λ * 1.40λ) with an increment of 4 mm * 4mm (~0.1λ * 0.1λ). Figure 3.8 demonstrates the simulated S11 and H-plane radiation pattern (H-plane pattern is chosen because it has higher cross-polarization which can be used to show the impact of the ground

plane length on the cross-polarization level). It shows that as the ground plane length increases from 36 mm (0.79λ) to 52 mm (1.22λ), the resonant frequency goes up and the bandwidth decreases, and both gain and directivity increase while cross-polarization decreases. However, a further increase in the ground plane length can lead to gain and directivity drop, and increase in cross-polarization. Therefore, one has to choose a ground plane size based on their applications, namely, a smaller ground if a wide bandwidth is preferable to high gain/directivity and low cross-polarization, or a larger ground (up to 1.22λ) if high gain and directivity, and low cross-polarization are more desirable than a wide bandwidth.

Table 3.9 Antenna Performance vs. Different Ground Plane Lengths

| $H_{side\ wall}$ (mm) | $L_{ground}$ (mm) | $L_{ground}/\lambda$ | $f_r$ (GHz) | BW (%) | η (%) | Gain (dBi) | X-pol (dB) | Dir (dBi) |
|---|---|---|---|---|---|---|---|---|
| 15 | 36 | 0.79 | 6.6146 | 16.13 | 99.41 | 4.75 | -9.65 | 4.78 |
| 15 | 40 | 0.90 | 6.7672 | 14.85 | 99.29 | 6.24 | -13.24 | 6.28 |
| 15 | 44 | 1.01 | 6.8665 | 12.29 | 98.53 | 7.05 | -16.05 | 7.11 |
| 15 | 48 | 1.12 | 6.9743 | 10.71 | 98.33 | 7.77 | -17.12 | 7.85 |
| 15 | 52 | **1.22** | 7.0342 | 9.65 | 98.19 | 7.86 | -17.37 | 7.94 |
| 15 | 56 | 1.31 | 7.0170 | 9.58 | 98.27 | 7.40 | -17.43 | 7.48 |
| 15 | 60 | 1.40 | 7.0201 | 9.47 | 98.22 | 6.62 | -15.95 | 6.70 |
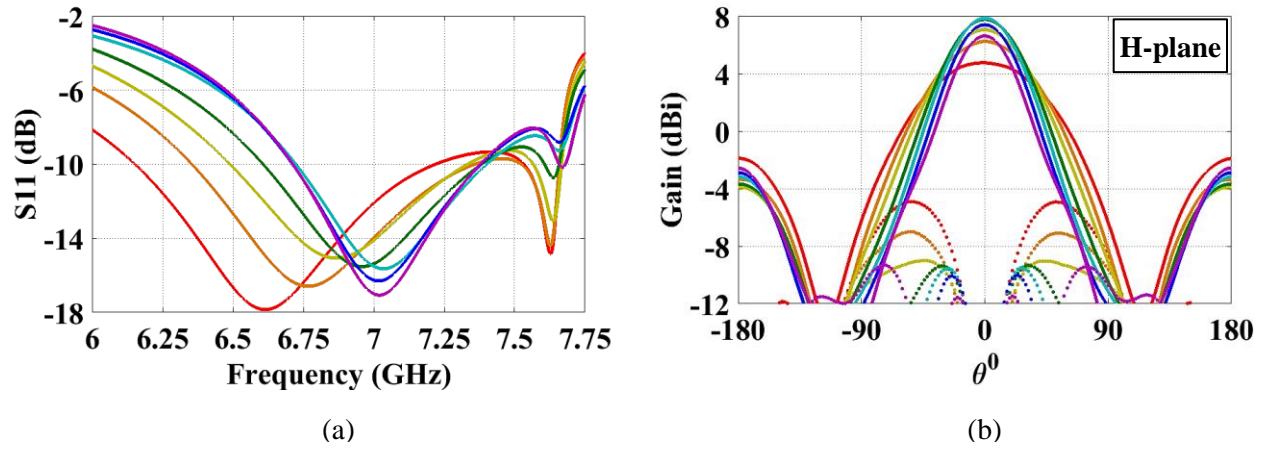
Figure 3.8 (a) Return loss and (b) H-plane radiation patterns of the $3\vec{x} \times 3\vec{y} \times 3\vec{z}$ SRR loaded DRA with U-shaped ground planes of various ground plane lengths: $L_{ground}$ = 36 mm, 40 mm, 44 mm, 48 mm, 52 mm, 56 mm and 60 mm. E-plane radiation patterns are not shown because the cross-polarizations are well below -40 dBi.

## III. Effect of the SRR Slit Position

Figure 3.9 demonstrates four slit positions to be studied, i.e., at the top (+z), bottom (-z), left (-y), and right (+y) sides of the SRR when viewed from the front (positive x-axis). The antenna parameters for the SRR slit position study are given in Table 3.10. From the simulated S11 results (Figure 3.10), because the one with the slit position at –z provides the most miniaturization, it should be used for the miniaturization purpose. It is worth mentioning that all the resonances shown in Figure 3.10 have the same radiation pattern (i.e. broadside radiation pattern) at all four slit positions. Although the one with the slits at the top of the SRRs (+z) provides the least miniaturization, it has the widest bandwidth among all other slit positions, and thus is a good candidate for wideband applications. It is also worth mentioning that although the

merged resonances are observed with the given antenna parameters, it is not always true when the antenna parameters are altered.



(a) -z

(b) +z

(c) -y

(d) +y
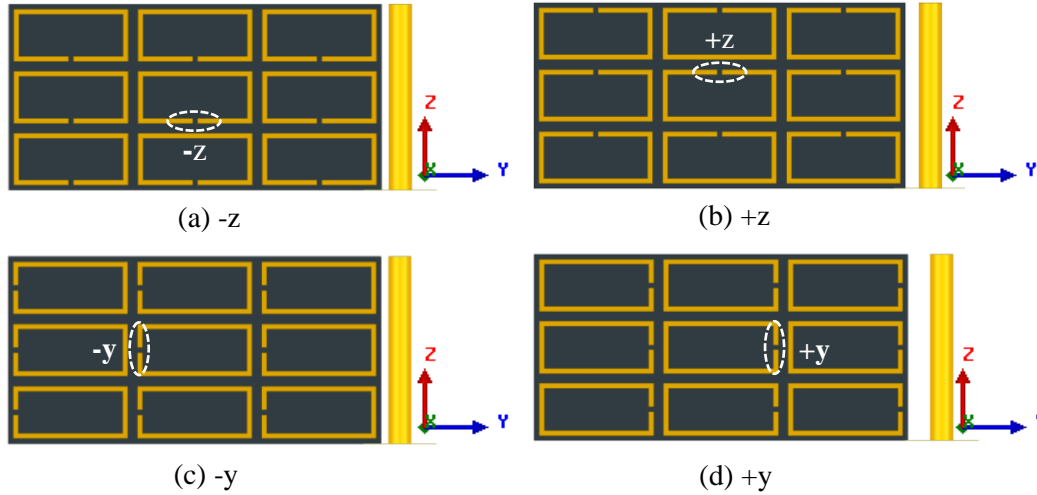
Figure 3.9 SRR slit positions: (a) +z, (b) –z, (c) –y, and (d) +y.

Table 3.10 Antenna Parameters for SRR Slit Position Study

| SRR Arrangement | Host DRA (mm) | | | SRR (mm) | | | | Slit Position | $h_{probe}$ (mm) |
|---|---|---|---|---|---|---|---|---|---|
| | W | H | L | $L_{SRR}$ | $H_{SRR}$ | w | g | | |
| $3\vec{x} \times 3\vec{y} \times 3\vec{z}$ | 15 | 7.5 | 0.254 | 4.6 | 2.1 | 0.2 | 0.2 | -z, +z, -y, +y | 7.5 |
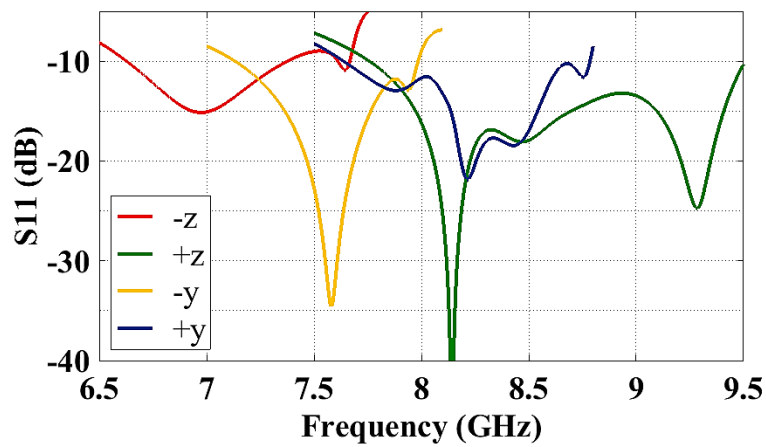


Figure 3.10 S11 plots of the $3\vec{x} \times 3\vec{y} \times 3\vec{z}$ SRR loaded DRA with different slit positions.

44

## IV. Parametric Study on the SRR Trace Width

A group of SRR trace widths, varied from 0.2 mm to 0.8 mm with an increment of 0.1 mm, are studied. The antenna parameters for the trace width study are shown in Table 3.11. Since both effective ring area, $A_{ring}$, and effective ring cross-sectional area, $A_{cross-section}$, are functions of the trace width, the variation in the trace width will lead to different miniaturization capability (resonant frequency shift) and conductor loss (radiation efficiency). The effective ring area and cross-sectional area can be expressed by:

$$A_{ring} = (L_{SRR} - \frac{1}{2}w) \cdot (H_{SRR} - \frac{1}{2}w) \tag{3.17}$$

$$A_{cross-section} = w * t - (w - 2\delta)(t - 2\delta) = 2\delta w + 2\delta t - 4\delta^2 \tag{3.18}$$

where $L_{SRR}$, $H_{SRR}$, $w$, $t$, and $\delta$ are the ring length, ring height, ring width, ring thickness, and skin depth, respectively, as demonstrated in Figure 3.11. It can be seen that the effective ring area, $A_{ring}$ is inversly proportional to the ring width, $w$, while the effective cross-sectional area, $A_{cross-section}$ is proportional to the ring width, $w$. Therefore, a wider trace will result in less miniaturization due to a reduced ring area ($A_{ring} \downarrow \rightarrow \mu \downarrow \rightarrow f_r \uparrow$), and less conductor loss due to an increased cross-sectional area ($A_{cross-section} \uparrow \rightarrow R \downarrow \rightarrow P_{cond} \downarrow$), while a thinner trace will result in more miniaturization due to an increased effective ring area ($A_{ring} \uparrow \rightarrow \mu \uparrow \rightarrow f_r \downarrow$), and more conductor loss due to a reduced effective cross-sectional area ($A_{cross-section} \downarrow \rightarrow R \uparrow \rightarrow P_{cond} \uparrow$).

Table 3.11 Antenna Parameters for SRR Trace Width Study

| SRR Arrangement | Host DRA Dimensions (mm) | | | SRR Dimensions (mm) | | | | Slit Position | $h_{probe}$ (mm) |
| | W | H | L | $L_{SRR}$ | $H_{SRR}$ | w | g | | |
|---|---|---|---|---|---|---|---|---|---|
| $3\vec{x} \times 3\vec{y} \times 3\vec{z}$ | 15 | 7.5 | 0.254 | 4.6 | 2.1 | 0.2, 0.3, 0.4, 0.5, 0.6, 0.7, 0.8 | 0.2 | -z | 7.5 |
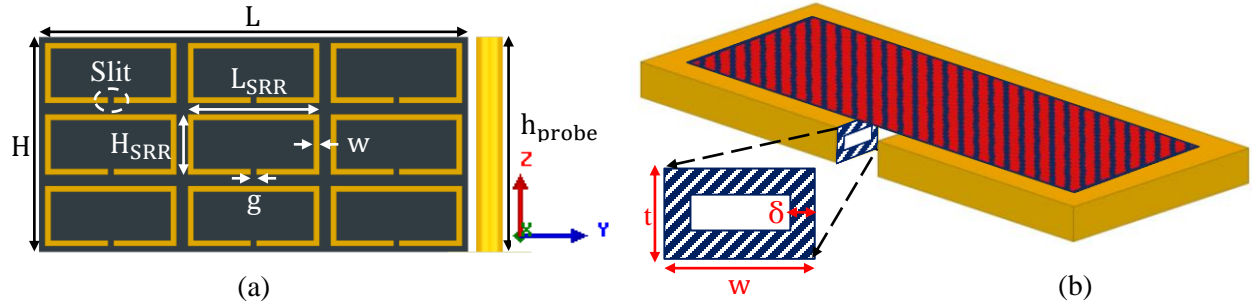


Figure 3.11 (a) Front view of the $3\vec{x} \times 3\vec{y} \times 3\vec{z}$ SRR loaded DRA. (b) Effective ring area (red and blue shaded area ▨), $A_{ring}$, and effective cross-sectional area (white and blue shaded area ▨), $A_{cross-section}$.

Figure 3.12 demonstrates the simulation results of the trace width study. The more detailed antenna performance at different ring widths is shown in Table 3.11. As expected, the resonant frequency goes up (less miniaturization), and the efficiency ($\eta = $ Dir/Gain) increases (less conductor loss) with the increase in the ring trace width, $w$. As the ring width increases from 0.2 mm to 0.8 mm, the resonant frequency increases from 6.9743 GHz to 8.3764 GHz, and the efficiency increases from 98.33% to 99.35%. Since the conductor loss in antennas with the SRR arrangement of $3\vec{x} \times 3\vec{y} \times 3\vec{z}$ is already very low, the efficiency improvement by increasing the ring width is not very obvious.
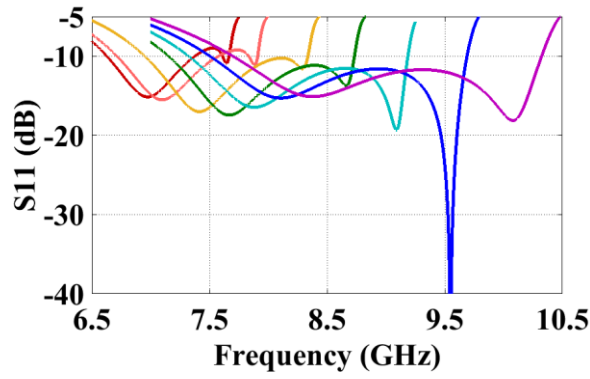
(a)
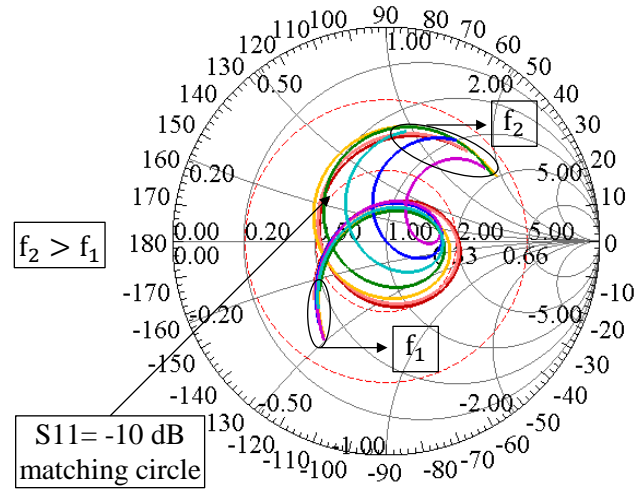
(b)
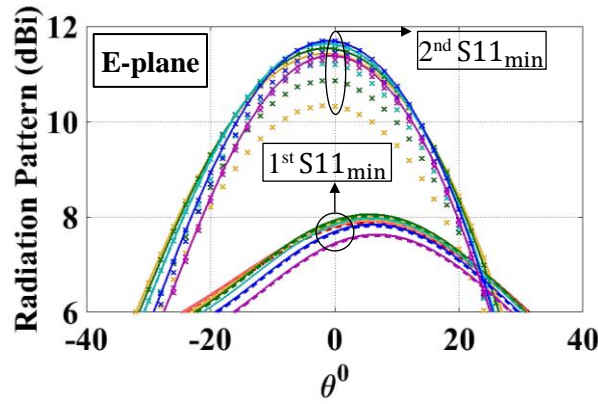
(c)
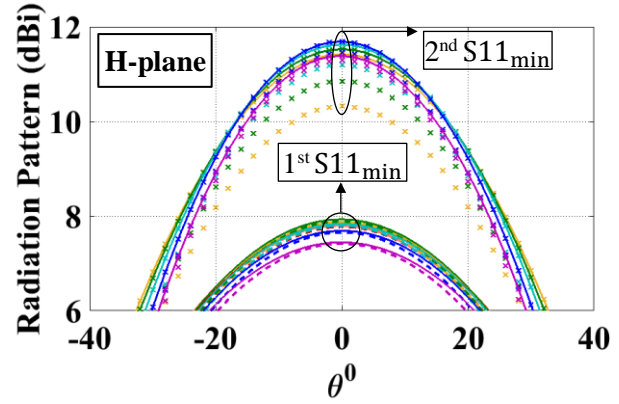
(d)

| w = 0.2 mm | w = 0.3 mm | w = 0.4 mm | w = 0.5 mm | w = 0.6 mm | w = 0.7 mm | w = 0.8 mm |
|---|---|---|---|---|---|---|

Figure 3.12 (a) Return loss, (b) Smith Chart, and (c) E-plane and (d) H-plane radiation patterns of the $3\vec{x} \times 3\vec{y} \times 3\vec{z}$ SRR loaded DRA with various trace widths, $w$. S11 & Smith Chart: Solid line; Directivity and Gain of the $1^{st}$ $S11_{min}$: solid line and dashed line, respectively; Directivity and Gain of the $2^{nd}$ $S11_{min}$: solid line with cross and cross, respectively.

It is interesting to notice that the first two dips in S11 curves (i.e. $f_{r1}$ and $f_{r2}$, or $1^{st}$ $S11_{min}$ and $2^{nd}$ $S11_{min}$), both with broadside radiation patterns, start to merge into a wide band as the trace width increases to w ≥ 0.4 mm. The bandwidth increases rapidly from 10.71% at w = 0.2 mm to 29.15% at w = 0.8 mm, however, at the expense of a large center frequency shift (2.2535

47

GHz). It is more obvious to see from the Smith chart that the impedance loop becomes smaller as the trace width increases, which makes it easier to form a wide bandwidth, as illustrated in Figure 3.12 (b). With a smaller impedance loop, more frequencies are able to fall into the -10 dB matching circle (red dashed inner circle), leading to a much wider bandwidth. By varying the spacing between the probe and the antenna, the loop can be moved within the matching circle. As demonstrated on the Smith Chart, frequencies increase from $f_1$ to $f_2$. Thus, in order to have more miniaturization while maintaining a wide bandwidth, the loop should move in such a way that more frequencies from the $f_1$ side fall into the matching circle. Since input impedances in the $f_1$ region are capacitive and have small resistances ($< 50\ \Omega$), this can be achieved by reducing the spacing between the probe and the antenna. However, a too small probe gap can also move some frequencies on the $f_2$ side out of/farther away from the matching circle. Therefore, there is a critical probe distance from the antenna for the best performance of both miniaturization and bandwidth. Figure 3.12 (c) and (d) illustrate the E and H-plane radiation patterns of the antenna. Since the second minimum in S11 at w = 0.2 mm  does not merge with the first mode to form a wide band, the radiation patterns of  $2^{\text{nd}}$ $S11_{\text{min}}$ at w = 0.2 mm are not shown. It shows that the gain and directivity of the first S11 minimum increase as the trace width, $w$, increases from 0.2 mm to 0.5 mm, and decrease as the trace width is $>$ 0.5 mm. Similarly, there is a critical trace width ($w = 0.7\ mm$) for the highest gain and directivity of the second S11 minimum. It is also worth noticing that the directivity of the second S11 minimum is much higher than that of the first S11 minimum at any given width. For example, at w = 0.7 mm, a 4 dB difference in directivities of the first and second S11 minimums  is observed, with $\text{Dir}_1$ = 7.7 dBi and $\text{Dir}_2$ = 11.7 dBi.

Table 3.12 Antenna Performance vs. Ring Width

| w (mm) | BW (%) | 1$^{st}$ S11$_{min}$ | | | | | 2$^{nd}$ S11$_{min}$ | | | | |
|---|---|---|---|---|---|---|---|---|---|---|---|
| | | $f_{r1}$ (GHz) | $\eta_1$ (%) | Gain$_1$ (dBi) | X-pol (dB) | Dir$_1$ (dBi) | $f_{r2}$ (GHz) | $\eta_2$ (%) | Gain$_2$ (dBi) | X-pol (dB) | Dir$_2$ (dBi) |
| 0.2 | 10.71 | 6.9743 | 98.33 | 7.77 | -17.12 | 7.85 | - | - | - | - | - |
| 0.3 | 12.17 | 7.0973 | 99.16 | 7.81 | -17.01 | 7.84 | - | - | - | - | - |
| 0.4 | 18.15 | 7.4142 | 98.88 | 7.83 | -16.86 | 7.88 | 8.2913 | 77.66 | 10.34 | -19.23 | 11.43 |
| 0.5 | 19.90 | 7.6673 | 99.14 | 7.89 | -16.68 | 7.93 | 8.6620 | 85.55 | 10.86 | -19.48 | 11.54 |
| 0.6 | 22.59 | 7.8819 | 99.20 | 7.8 | -16.18 | 7.84 | 9.0897 | 90.54 | 11.21 | -19.74 | 11.64 |
| 0.7 | 25.44 | 8.1058 | 99.24 | 7.66 | -15.56 | 7.69 | 9.5488 | 94.74 | 11.46 | -20.14 | 11.69 |
| 0.8 | 29.15 | 8.3764 | 99.35 | 7.42 | -14.78 | 7.45 | 10.0792 | 97.89 | 11.29 | -19.97 | 11.39 |

## V. Parametric Study on the SRR Gap Width

Similarly, a parametric study on the SRR gap width, *g*, is performed. The gap width is varied from 0.2 mm to 4.2 mm with an increment of 1 mm, while other antenna parameters remain the same, as shown in Table 3.13. The gap width controls the circumference of the ring and thus controls the resonant frequency of the ring. In other words, the resonant frequency of the ring shifts up as the ring gap increases, leading to less miniaturization. And also, the increase in the ring gap can lead to less polarization-directed currents $(\vec{\iota_y})$ cancellation in rings due to a shortened path that carries the out-of-phase currents, resulting in higher efficiency. The simulation results are shown in Table 3.14 and agree well with the above analysis. A similar phenomenon of the first two resonances merging is also observed as the gap width increases. But compared to the case with an increased ring trace width, increasing gap width seems to be able to

provide more miniaturization while achieving the same bandwidth. For example, the bandwidths of the antenna with trace width of 0.7 mm and the antenna with gap width of 2.2 mm are 25.44% and 25.52%, respectively, while their center frequencies are 8.8273 GHz and 8.2966 GHz, respectively. Therefore, increasing gap width is a more efficient way of improving both bandwidth and efficiency in this case, without compromising as much miniaturization as increasing the trace width.

Table 3.13 Antenna Parameters for the SRR Gap Width Study

| SRR Arrangement | Host DRA (mm) | | | SRR (mm) | | | | Slit Location | $h_{probe}$ (mm) |
|---|---|---|---|---|---|---|---|---|---|
| | W | H | L | $L_{SRR}$ | $H_{SRR}$ | w | g | | |
| $3\vec{x} \times 3\vec{y} \times 3\vec{z}$ | 15 | 7.5 | 0.254 | 4.6 | 2.1 | 0.2 | 0.2, 1.2, 2.2, 3.2, 4.2 | -z | 7.5 |

Table 3.14 Antenna Performance vs. Gap Width

| g (mm) | BW (%) | $1^{st}$ $S11_{min}$ | | | | $2^{nd}$ $S11_{min}$ | | | |
|---|---|---|---|---|---|---|---|---|---|
| | | $f_{r1}$ (GHz) | $\eta_1$ (%) | $Gain_1$ (dBi) | $Dir_1$ (dBi) | $f_{r2}$ (GHz) | $\eta_2$ (%) | $Gain_2$ (dBi) | $Dir_2$ (dBi) |
| 0.2 | 10.71 | 6.9743 | 98.33 | 7.77 | 7.85 | - | - | - | - |
| 1.2 | 14.20 | 7.2376 | 100 | 7.77 | 7.77 | - | - | - | - |
| 2.2 | 25.52 | 7.5884 | 100 | 7.76 | 7.76 | 9.0048 | 89.51 | 11.52 | 12.00 |
| 3.2 | 31.86 | 7.9086 | 99.57 | 7.60 | 7.62 | 9.8642 | 98.43 | 12.00 | 12.07 |
| 4.2 | 31.64 | 8.212 | 100 | 7.63 | 7.63 | 10.06 | 100 | 11.43 | 11.43 |

### 3.2.2 Dielectric Resonator Antenna with Split Rings of Different Arrangements

In the previous section, the host dielectric resonator antenna loaded with three layers of $3\vec{y} \times 3\vec{z}$ SRRs $(3\vec{x} \times 3\vec{y} \times 3\vec{z})$ was studied. In this section, the effect of SRR arrangements will be investigated. Figure 3.13 shows the host dielectric loaded with three identical layers of split rings in six different arrangements. Ring parameters, such as trace width ($w$), gap width ($g$), and spacing between adjacent SRRs ($s$), probe and ground plane dimensions remain the same in all cases, as illustrated in Table 3.15.



(a) $3\vec{x} \times 3\vec{y} \times 3\vec{z}$     (b) $3\vec{x} \times 3\vec{y} \times 2\vec{z}$     (c) $3\vec{x} \times 3\vec{y} \times 1\vec{z}$

(d) $3\vec{x} \times 2\vec{y} \times 2\vec{z}$     (e) $3\vec{x} \times 2\vec{y} \times 1\vec{z}$     (f) $3\vec{x} \times 1\vec{y} \times 1\vec{z}$
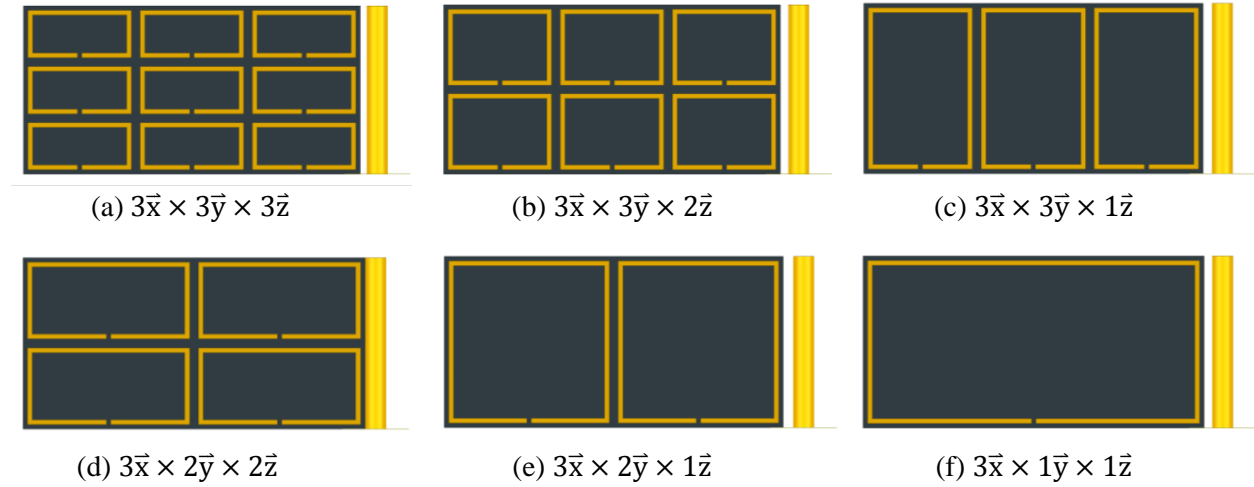
Figure 3.13 Front views of the six different split ring arrangements: (a) $3\vec{x} \times 3\vec{y} \times 3\vec{z}$, (b) $3\vec{x} \times 3\vec{y} \times 2\vec{z}$, (c) $3\vec{x} \times 3\vec{y} \times 1\vec{z}$, (d) $3\vec{x} \times 2\vec{y} \times 2\vec{z}$, (e) $3\vec{x} \times 2\vec{y} \times 1\vec{z}$, and (f) $3\vec{x} \times 1\vec{y} \times 1\vec{z}$. The three identical layers of SRRs are placed at the center, back and front surfaces of the dielectric.

Table 3.15 Parameters of Split Rings in Different Arrangements

| Arrangement | SRR | | | | | $h_{probe}$ (mm) | Ground Plane | |
|---|---|---|---|---|---|---|---|---|
| | $L_{SRR}$ (mm) | $H_{SRR}$ (mm) | w (mm) | g (mm) | s (mm) | | $L_{ground}$ (mm) | $L_{ground}$ (mm) |
| $3\vec{y} \times 3\vec{z}$ | 4.6 | 2.1 | | | | | | |
| $3\vec{y} \times 2\vec{z}$ | 4.6 | 3.35 | | | | | | |
| $3\vec{y} \times 1\vec{z}$ | 4.6 | 7.1 | 0.2 | 0.2 | 0.4 | 7.5 | $1.1\lambda$ | 15 |
| $2\vec{y} \times 2\vec{z}$ | 7.1 | 3.35 | | | | | | |
| $2\vec{y} \times 1\vec{z}$ | 7.1 | 7.1 | | | | | | |
| $1\vec{y} \times 1\vec{z}$ | 14.6 | 7.1 | | | | | | |

As expected, the resonant frequency varies with different arrangements, as illustrated in Figure 3.14, and the miniaturization capability (MC) follows the same order as predicted at the beginning of this section. As mentioned earlier, the SRR unit cell that has the lowest resonant frequency and highest peak permeability allows for the highest miniaturization capability; and the unit cell that has the highest resonant frequency and lowest peak permeability allows for the lowest miniaturization capability. In this case, the arrangements $3\vec{x} \times 1\vec{y} \times 1\vec{z}$ and $3\vec{x} \times 3\vec{y} \times 3\vec{z}$ should be the ones that provide the highest and the lowest miniaturization capabilities, respectively. And this is verified in Figure 3.14, where it shows that the resonant frequency of the $3\vec{x} \times 1\vec{y} \times 1\vec{z}$ SRR loaded DRA is the lowest and that of the $3\vec{x} \times 3\vec{y} \times 3\vec{z}$ SRR loaded DRA is the highest among the six arrangements.
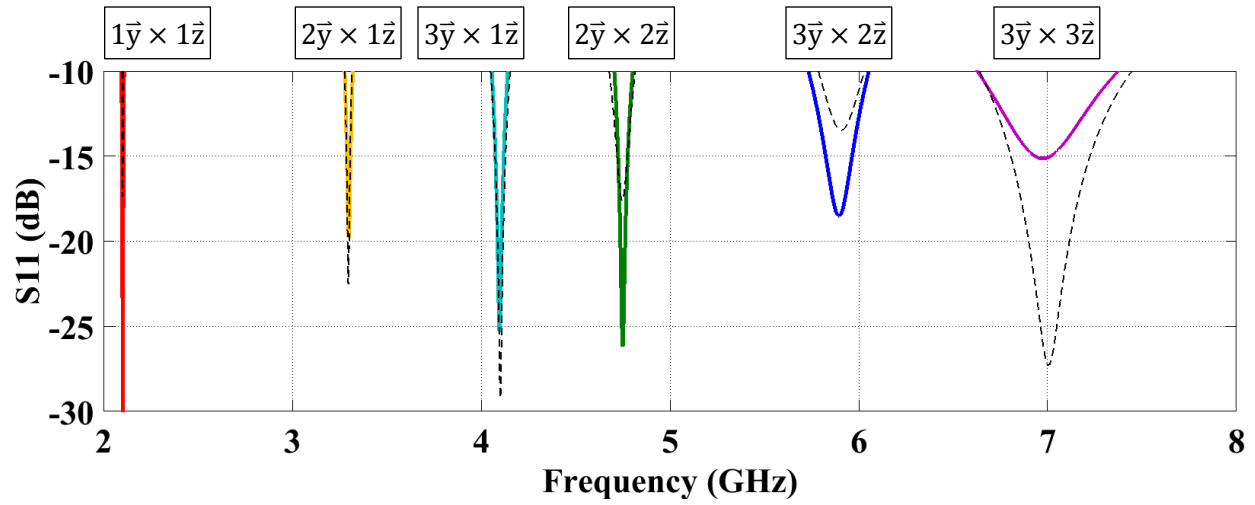
| Arrangement | $3\vec{x} \times 1\vec{y} \times 1\vec{z}$ | $3\vec{x} \times 2\vec{y} \times 1\vec{z}$ | $3\vec{x} \times 3\vec{y} \times 1\vec{z}$ | $3\vec{x} \times 2\vec{y} \times 2\vec{z}$ | $3\vec{x} \times 3\vec{y} \times 2\vec{z}$ | $3\vec{x} \times 3\vec{y} \times 3\vec{z}$ |
|---|---|---|---|---|---|---|
| SRR Loaded DRA | —— | —— | —— | —— | —— | —— |
| Unloaded Equivalent DRA | - - - - | - - - - | - - - - | - - - - | - - - - | - - - - |
| $\varepsilon_{r\_equivalent}$ | 1390 | 540 | 333.5 | 242 | 146.5 | 96 |

Figure 3.14 S11 plots of SRR loaded DRAs with different ring arrangements.

In order to estimate the miniaturization capability of each arrangement, six unloaded equivalent DRAs based on pure high-permittivity materials that resonate at the same frequencies as the split ring loaded DRAs with the six arrangements are also studied in HFSS. The permittivity values obtained from the simulations agree well with the calculated ones by using the method stated in [65]. The miniaturization capabilities of the AMDRAs with SRRs of $3\vec{x} \times 3\vec{y} \times 3\vec{z}$, $3\vec{x} \times 3\vec{y} \times 2\vec{z}$, $3\vec{x} \times 2\vec{y} \times 2\vec{z}$, $3\vec{x} \times 3\vec{y} \times 1\vec{z}$, $3\vec{x} \times 2\vec{y} \times 1\vec{z}$, and $3\vec{x} \times 1\vec{y} \times 1\vec{z}$ are 6.61x, 8.16x, 10.49x, 12.31x, 15.67x, and 25.14x, respectively; and the permittivities required for pure dielectric based DRAs to resonate at the same frequencies are 96, 146.5, 242, 333.5, 540, and 1390, respectively. As the antennas become more miniaturized, an efficiency/gain drop and/or a reduced bandwidth are expected due to the fundamental limitations of small antennas, which are observed in Table 3.16. However, it is interesting to notice that, compared to the $3\vec{x} \times 2\vec{y} \times 2\vec{z}$ SRR loaded DRA,

53

the one with $3\vec{x} \times 3\vec{y} \times 1\vec{z}$ SRRs, despite being more miniaturized (14.78% more miniaturization, or frequency shifting down by 0.6521 GHz), has higher efficiency ($\Delta\eta =$ +6.89%), higher gain ($\Delta$Gain = +1.14 dB), lower cross-polarization ($\Delta$Xpol = −9.63 dB) and almost the same bandwidth ($\Delta$BW = +0.01%).

Table 3.16 Antenna Performance of Split Ring Loaded Dielectric Resonator Antennas with Different Ring Arrangements

| Arrangement | $f_r$ (GHz) | BW (%) | $\eta$ (%) | Gain (dBi) | X-pol (dB) | Dir (dBi) | Calculated $\varepsilon_{r\_equivalent}$ | Simulated $\varepsilon_{r\_equivalent}$ | MC |
|---|---|---|---|---|---|---|---|---|---|
| $3\vec{x} \times 3\vec{y} \times 3\vec{z}$ | 6.9743 | 10.71 | 98.33 | 7.77 | -17.12 | 7.85 | 98.2 | 96 | 6.61 |
| $3\vec{x} \times 3\vec{y} \times 2\vec{z}$ | 5.8948 | 5.46 | 96.05 | 7.89 | -19.86 | 8.06 | 143.3 | 146.5 | 8.16 |
| $3\vec{x} \times 3\vec{y} \times 1\vec{z}$ | 4.0976 | 2.08 | 83.75 | 7.13 | -23.51 | 7.90 | 313 | 333.5 | 12.31 |
| $3\vec{x} \times 2\vec{y} \times 2\vec{z}$ | 4.7497 | 2.07 | 76.86 | 5.99 | -13.88 | 7.13 | 229 | 242 | 10.49 |
| $3\vec{x} \times 2\vec{y} \times 1\vec{z}$ | 3.2987 | 1.31 | 75.90 | 6.64 | -22.93 | 7.84 | 488 | 540 | 15.67 |
| $3\vec{x} \times 1\vec{y} \times 1\vec{z}$ | 2.1022 | 0.66 | 48.77 | 4.25 | -17.48 | 7.37 | 1220 | 1390 | 25.14 |

In the previous section, it has been proven that the efficiency of a $3\vec{x} \times 3\vec{y} \times 3\vec{z}$ loaded DRA can be improved by increasing the ring width or the gap width. Although the SRR arrangement varies, the loss mechanisms in those antennas remain the same, i.e. conductor loss and dielectric loss. Therefore, one should expect an efficiency improvement in a DRA loaded with SRRs of any arrangements by increasing either the ring width or the gap width, or both, providing there is conductor loss in the antenna. In order to verify the hypothesis, wider ring widths and gap widths are applied to the DRAs with $3\vec{x} \times 3\vec{y} \times 1\vec{z}$, $3\vec{x} \times 2\vec{y} \times 2\vec{z}$, $3\vec{x} \times 2\vec{y} \times 1\vec{z}$, and $3\vec{x} \times 1\vec{y} \times 1\vec{z}$ SRRs. The above four arrangements are chosen because their radiation efficiencies are below 90% and still have some room for potential improvements, unlike the other two arrangements

having efficiencies above 96%. As can be seen from Figure 3.15~Figure 3.18 (see more detailed data in Table 3.17~Table 3.20), increasing ring width can more effectively improve the efficiency of the antennas in all four cases with less sacrifice of miniaturization capability (larger $\eta - f_r$ slope), while increasing gap width can more effectively increase the bandwidth (larger $BW - f_r$ slope). It is interesting to notice that, in Figure 3.18, as the gap width, $g$, increases from 8.2 mm to 12.2 mm, instead of observing an improvement in efficiency, a rapid efficiency drop (from 62.42% to 22.65%) is observed; instead of a more smooth improvement in bandwidth as observed in other cases, the bandwidth surges from 1.21% to 5.99%. This is caused by the resonance separation and merging as shown in Figure 3.19.

Figure 3.15 The effect of the ring width, $w$, and gap width, $g$, on the performance of the $3\vec{x} \times 3\vec{y} \times 1\vec{z}$ SRR loaded DRA.

Table 3.17 Efficiency Improvements of the $3\vec{x} \times 3\vec{y} \times 1\vec{z}$ SRR Loaded DRA

| Arrangement | w (mm) | g (mm) | $f_r$ (GHz) | BW (%) | η (%) | Gain (dBi) | X-pol (dB) | Dir (dBi) |
|---|---|---|---|---|---|---|---|---|
| $3\vec{x} \times 3\vec{y} \times 1\vec{z}$ | 0.2 | 0.2 | 4.0976 | 2.08 | 83.75 | 7.13 | -23.51 | 7.90 |
| | 0.4 | 0.2 | 4.2317 | 2.29 | 89.91 | 7.42 | -23.1 | 7.88 |
| | 0.6 | 0.2 | 4.3927 | 2.54 | 92.29 | 7.60 | -23.31 | 7.95 |
| | 0.8 | 0.2 | 4.5587 | 2.77 | 93.89 | 7.66 | -23.18 | 7.93 |
| | 0.2 | 1.2 | 4.3525 | 2.52 | 86.69 | 7.33 | -21.94 | 7.95 |
| | 0.2 | 2.2 | 4.5758 | 2.96 | 89.50 | 7.44 | -20.61 | 7.92 |
| | 0.2 | 3.2 | 4.83 | 3.51 | 91.75 | 7.61 | -19.31 | 7.98 |
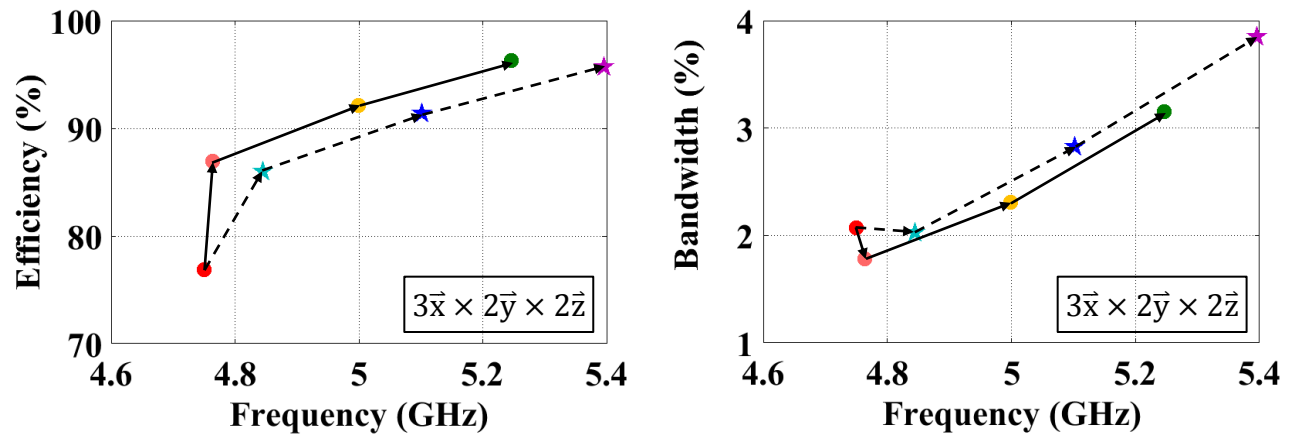
Figure 3.16 The effect of the ring width, $w$, and gap width, $g$, on the performance of the $3\vec{x} \times 2\vec{y} \times 2\vec{z}$ SRR loaded DRA.

Table 3.18 Efficiency Improvements of the $3\vec{x} \times 2\vec{y} \times 2\vec{z}$ SRR Loaded DRA

| Arrangement | w (mm) | g (mm) | $f_r$ (GHz) | BW (%) | η (%) | Gain (dBi) | X-pol (dB) | Dir (dBi) |
|---|---|---|---|---|---|---|---|---|
| | 0.2 | 0.2 | 4.7497 | 2.07 | 76.86 | 5.99 | -13.88 | 7.13 |
| | 0.4 | 0.2 | 4.764 | 1.78 | 86.93 | 7.43 | -19.51 | 8.04 |
| | 0.6 | 0.2 | 4.9991 | 2.31 | 92.11 | 7.70 | -19.2 | 8.06 |
| $3\vec{x} \times 2\vec{y} \times 2\vec{z}$ | 0.8 | 0.2 | 5.2464 | 3.15 | 96.33 | 7.96 | -19.18 | 8.12 |
| | 0.2 | 1.2 | 4.8443 | 2.03 | 85.99 | 7.31 | -18.96 | 7.97 |
| | 0.2 | 2.2 | 5.1016 | 2.83 | 91.42 | 7.62 | -18.36 | 8.01 |
| | 0.2 | 3.2 | 5.3954 | 3.85 | 95.69 | 7.92 | -18.36 | 8.11 |

Figure 3.17 The effect of the ring width, $w$, and gap width, $g$, on the performance of the $3\vec{x} \times 2\vec{y} \times 1\vec{z}$ SRR loaded DRA.

Table 3.19 Efficiency Improvements of the $3\vec{x} \times 2\vec{y} \times 1\vec{z}$ SRR Loaded DRA

| Arrangement | w (mm) | g (mm) | $f_r$ (GHz) | BW (%) | η (%) | Gain (dBi) | X-pol (dB) | Dir (dBi) |
|---|---|---|---|---|---|---|---|---|
| $3\vec{x} \times 2\vec{y} \times 1\vec{z}$ | 0.2 | 0.2 | 3.2987 | 1.31 | 75.90 | 6.64 | -22.93 | 7.84 |
| | 0.4 | 0.2 | 3.3922 | 1.38 | 83.98 | 7.07 | -23.08 | 7.83 |
| | 0.6 | 0.2 | 3.4859 | 1.48 | 88.33 | 7.35 | -23.13 | 7.89 |
| | 0.8 | 0.2 | 3.5953 | 1.60 | 90.50 | 7.46 | -22.86 | 7.90 |
| | 0.2 | 1.2 | 3.4831 | 1.55 | 79.92 | 6.90 | -22.22 | 7.87 |
| | 0.2 | 2.2 | 3.6361 | 1.77 | 83.38 | 7.11 | -20.83 | 7.90 |
| | 0.2 | 3.2 | 3.8214 | 2.03 | 85.32 | 7.26 | -20.28 | 7.95 |

| w = 0.2 mm<br>g = 0.2 mm | w = 0.9 mm<br>g = 0.2 mm | w = 1.6 mm<br>g = 0.2 mm | w = 2.3 mm<br>g = 0.2 mm | w = 0.2 mm<br>g = 4.2 mm | w = 0.2 mm<br>g = 8.2 mm | w = 0.2 mm<br>g = 12.2 mm |
|---|---|---|---|---|---|---|
| ● | ● | ● | ● | ★ | ★ | ★ |
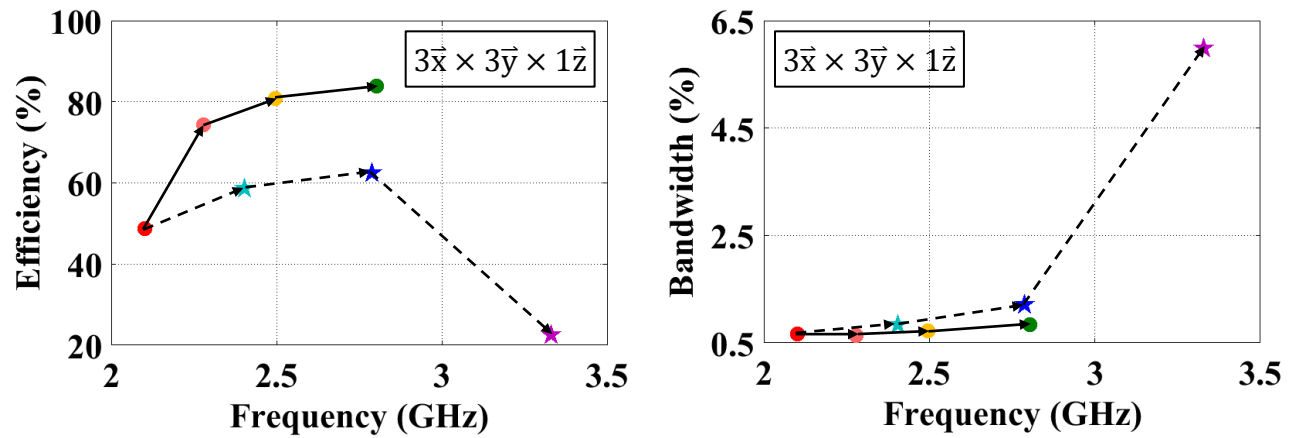
Figure 3.18 The effect of the ring width, $w$, and gap width, $g$, on the performance of the $3\vec{x} \times 1\vec{y} \times 1\vec{z}$ SRR loaded DRA.

Table 3.20 Efficiency Improvements of the $3\vec{x} \times 1\vec{y} \times 1\vec{z}$ SRR Loaded DRA

| Arrangement | w<br>(mm) | g<br>(mm) | $f_r$<br>(GHz) | BW<br>(%) | η<br>(%) | Gain<br>(dBi) | X-pol<br>(dB) | Dir<br>(dBi) |
|---|---|---|---|---|---|---|---|---|
| | 0.2 | 0.2 | 2.1022 | 0.66 | 48.77 | 4.25 | -21.73 | 7.37 |
| | 0.9 | 0.2 | 2.2793 | 0.64 | 74.29 | 6.16 | -21.93 | 7.45 |
| | 1.6 | 0.2 | 2.4961 | 0.72 | 80.85 | 6.69 | -21.91 | 7.61 |
| $3\vec{x} \times 1\vec{y} \times 1\vec{z}$ | 2.3 | 0.2 | 2.8032 | 0.84 | 83.85 | 6.95 | -21.48 | 7.71 |
| | 0.2 | 4.2 | 2.4038 | 0.84 | 58.72 | 5.21 | -20.37 | 7.53 |
| | 0.2 | 8.2 | 2.788 | 1.21 | 62.42 | 5.53 | -18.69 | 7.58 |
| | 0.2 | 12.2 | 3.32965 | 5.99 | 22.65 | 1.52 | -14.89 | 7.97 |

| $f_r = 3.2664$ GHz | | $f_r = 3.32965$ GHz | | $f_r = 3.3869$ GHz | |
|---|---|---|---|---|---|
| —— $\text{Dir}_{H-plane}$ | ---- $\text{Dir}_{E-plane}$ | —— $\text{Dir}_{H-plane}$ | ---- $\text{Dir}_{E-plane}$ | —— $\text{Dir}_{H-plane}$ | ---- $\text{Dir}_{E-plane}$ |
| + $\text{Gain}_{H-plane}$ | • $\text{Gain}_{E-pane}$ | + $\text{Gain}_{H-plane}$ | • $\text{Gain}_{E-pane}$ | + $\text{Gain}_{H-plane}$ | • $\text{Gain}_{E-pane}$ |
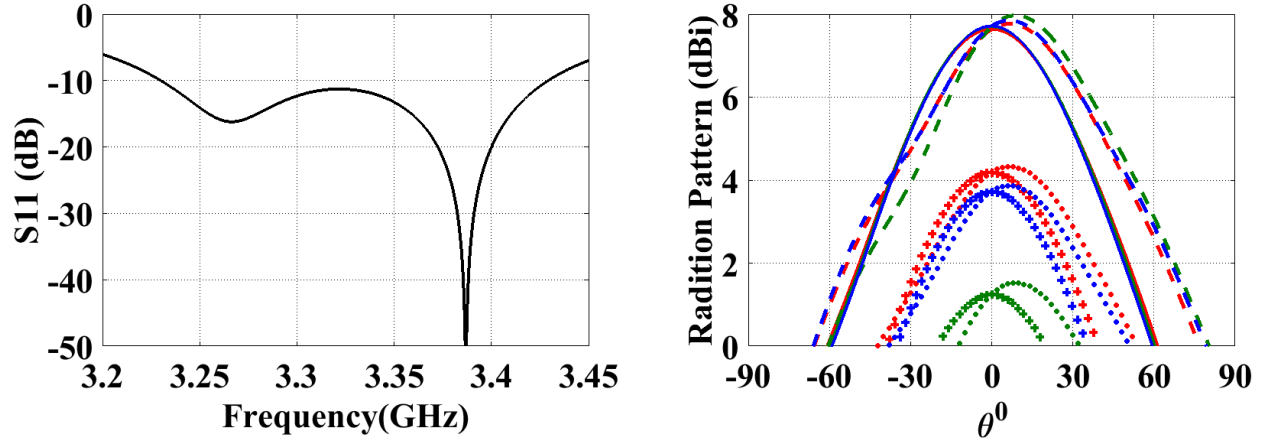
Figure 3.19 Resonance separation in the $3\vec{x} \times 1\vec{y} \times 1\vec{z}$ SRR loaded DRA at g = 12.2 mm.

## 3.3   Fabrication and Measurement Results

In order to experimentally verify the above discussion, a split ring loaded dielectric resonator antenna, as shown in Figure 3.20, was fabricated and tested. The dimensions of the antenna are given in Table 3.21. The antenna is based on the same low-permittivity dielectric material that is used throughout this work, i.e. Rogers RT/duroid 5880 ($\varepsilon_r = 2.2, \tan\delta = 0.0009$). The ring arrangement of $1\vec{x} \times 1\vec{y} \times 1\vec{z}$ is chosen because of the following reasons: first, based on the previous discussions, the ring arrangement $1\vec{y} \times 1\vec{z}$ in the y-z plane can provide the highest miniaturization capability among all the arrangements that have been studied; second, the thickness of the dielectric chosen for this study, i.e. 0.127 mm, is too thin to hold a double sided pattern with the available fabrication facilities; and finally, the intended multi-layer stacking can cause large performance offset because the thickness of the adhesive layer becomes comparable to that of the host dielectric. The ground plane is made of an aluminum plate with a thickness of

0.79375 mm (1/32 in) and the 90 degree tilting angle is achieved by folding the plate. However, during the measurement, it was found that even a slight movement of the antenna could shift the resonant frequency because the ground plane was not strong enough to restrain the movement of the probe. Thanks to the fabrication team, this problem was solved by adding a thick aluminum plate to the bottom of the ground plane, as shown in Figure 3.20 (d).
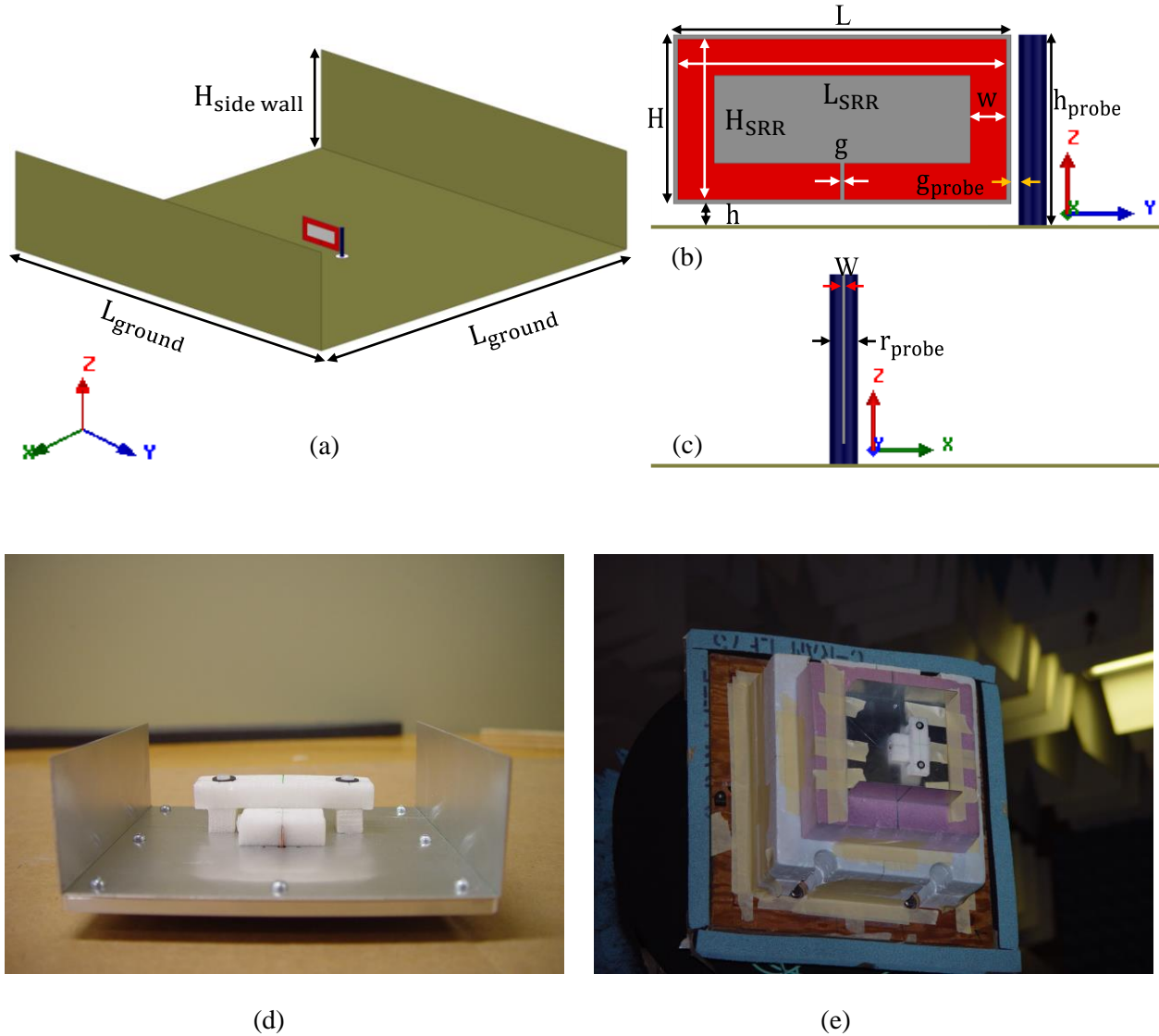


Figure 3.20 1-layer $1\vec{y} \times 1\vec{z}$ split ring loaded dielectric resonator antenna. The SRR is placed on the front surface of the dielectric. Each color represents one part of the antenna: ▬ Host DRA; ▬ SRR; ▬ Probe; ▬ Ground Plane). (a) 3-D view of the simulated antenna. (b) Front and (c) side views of the simulated antenna. (d) 3-D view of the fabricated antenna, and (e) the fabricated antenna under test in the anechoic chamber at the University of Manitoba.

Table 3.21 Dimensions of the Fabricated 1-layer $1\vec{y} \times 1\vec{z}$ Split Ring Loaded Dielectric Resonator Antenna

| Host DRA (mm) | | | SRR (mm) | | | | Probe (mm) | | | Air Gap (mm) | U-shaped Ground (mm) | |
|---|---|---|---|---|---|---|---|---|---|---|---|---|
| L | H | W | $L_{SRR}$ | $H_{SRR}$ | w | g | $r_{probe}$ | $h_{probe}$ | $g_{probe}$ | h | $L_{ground}$ | $H_{side\ wall}$ |
| 15 | 7.5 | 0.127 | 14.6 | 7.1 | 1.6 | 0.2 | 0.625 | 7.5 | 0.35 | 0 | 124 | 40 |

Table 3.22 and Figure 3.21 show the comparison of the simulation and measurement results of the fabricated antenna. The S11 results (Figure 3.21 (a)) indicate that there is a resonant frequency offset of 0.1462 GHz between the two resonant frequencies (solid black and dashed black curves). More specifically, the measured resonant frequency is at 2.9370 GHz while the simulated resonant frequency is at 2.7908 GHz. Since the resonant frequency of this type of antenna also varies with the matching condition, the resonant frequency of this antenna can be slight shifted if the matching condition is altered, which means the resonant frequency of an antenna with a return loss of -20 dB is different from that of the same antenna with a return loss of -30 dB. And thus, the different matching quality observed from the simulated (black solid curve) and the measured (black dashed curve) S11 plots is one of the reasons for the resonant frequency offset, but not a significant reason. Many other factors, such as simulation errors, measurement errors, and fabrication errors, that can all contribute to the resonant frequency offset. Here, the case of fabrication errors will be demonstrated to show how such a frequency offset can be caused by minor fabrication imperfections. The resonant frequency of this antenna is sensitive to many antenna parameters, such as ring length ($L_{SRR}$), ring height ($H_{SRR}$), ring width ($w$), gap width ($g$), probe height ($h_{probe}$), spacing between the probe and the edge of the dielectric ($g_{probe}$), and the air gap between the host dielectric and the ground plane ($h$). Here, only three parameters, namely, ring width, $w$, gap width, $g$, and air gap, $h$, will be investigated.

Ideally, the host dielectric should be directly placed on the ground plane and there should be no air gap between the dielectric and the ground plane, namely, h = 0 mm. However, this is not feasible in reality and there will always be an air gap, i.e. h > 0 mm. It is found that an air gap of 0.126 mm (red solid curve) is enough to cause the observed resonant frequency offset. Similarly, small variations in the ring width or gap width can also lead to the same degree of frequency offset. The blue solid curve suggests that a slightly wider ring with a ring width of 1.95 mm instead of 1.6 mm is enough to cause the offset, and a slightly larger slit with a gap width of 0.95 mm instead of 0.2 mm is enough to provide the observed frequency shift. It is worth noting that the fabrication imperfections can happen to any antenna parameters and are not only limited to the above three parameters, and the frequency offset is caused by a combination of fabrication imperfections in multiple parameters in addition to the simulation and measurement errors.

Figure 3.21 (b) demonstrates the comparison of the simulated and measured E and H-plane radiation patterns. It is clear that the measured gain (7.15 dB) is about 0.70 dB lower than the simulated gain (7.85 dBi). Apart from the simulation and measurement errors, there are also many other factors that can contribute to such difference. The reduced gain indicates that there is higher loss in the fabricated antenna than the simulated antenna. And this is expected because there are indeed new losses that are introduced into the fabricated antenna but not considered in simulations, such as losses from the tape, foam, and nylon screws that are used for stabilizing the antenna. Such losses can be reduced if the host dielectric is thick enough to stand on its own, or less lossy materials can be used for supporting the antenna.

Table 3.22 Simulation and Measurement Results of the Fabricated 1-layer $1\vec{y} \times 1\vec{z}$ Split Ring Loaded Dielectric Resonator Antenna

| | Antenna Parameters (mm) | | | $f_r$ (GHz) | BW (%) | Gain (dBi) | X-pol (dB) |
|---|---|---|---|---|---|---|---|
| | Air Gap, $h$ | Ring Width, $w$ | Gap Width, $g$ | | | | |
| **Simulation** | 0 | 1.6 | 0.2 | 2.7908 | 0.96 | 7.85 | -26.31 |
| **Measurement** | 0+error | 1.6+error | 0.2+error | 2.9370 | 2.21 | 7.15 | -22.68 |
| **Simulation** | 0.126 | 1.6 | 0.2 | 2.9379 | 1.07 | 8.12 | -26.13 |
| **Simulation** | 0 | 1.95 | 0.2 | 2.929 | 1.01 | 8.17 | -26.46 |
| **Simulation** | 0 | 1.6 | 0.95 | 2.936 | 1.07 | 8.01 | -26.65 |



Simulated, h=0 mm, w=1.6 mm, g=0.2 mm
Measured, h=0 mm, w=1.6 mm, g=0.2 mm
Simulated, h=0.126 mm, w=1.6 mm, g=0.2 mm
Simulated, h=0 mm, w=1.95 mm, g=0.2 mm
Simulated, h=0 mm, w=1.6 mm, g=0.95 mm

Simulated H-plane Gain
Simulated E-plane Gain
Measured H-plane Gain
Measured E-plane Gain
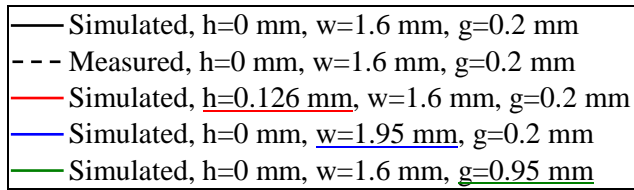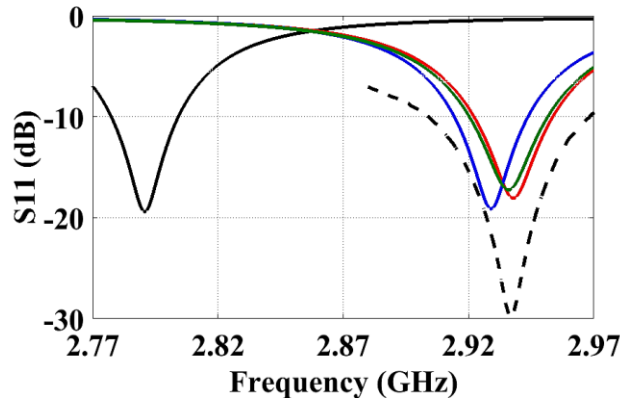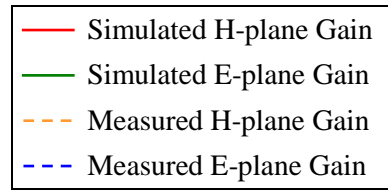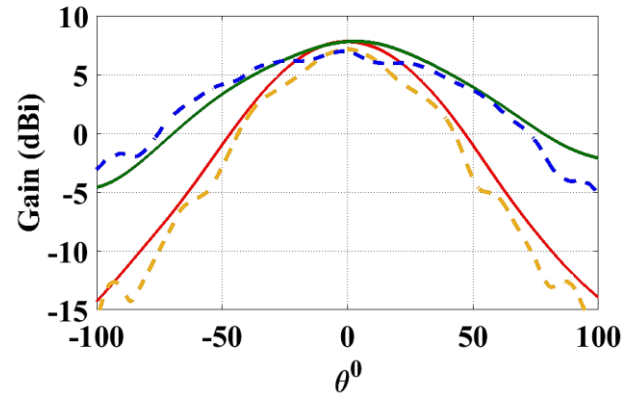
(a)                                                    (b)

Figure 3.21 The comparison of the simulated and measured results of the fabricated split ring loaded dielectric resonator antenna: (a) S11, (b) E and H-plane radiation patterns (Simulated at 2.7908 GHz and Measured at 2.9370 GHz).

## 3.4 Summary

The previous chapter has demonstrated that high permeability can be induced in a dielectric material by properly arranging SRRs. And thus, dielectric resonator antennas are expected to be miniaturized if such SRRs are employed. In order to evaluate the miniaturization capability of such SRR loaded DRAs, two evaluation methods for both high and low-permittivity based antennas were presented in the first section of this chapter. In the second section, the effects of SRR parameters and SRR arrangements on the antenna performance were studied. Since the ring arrangement can affect the two material properties that determine the miniaturization capability of the loaded DRAs, i.e. resonant frequency and peak permeability, different miniaturization capabilities are expected from different SRR arrangements. The simulations verified that the miniaturization capability indeed varies with the ring arrangement, and the arrangement $3\vec{x} \times 1\vec{y} \times 1\vec{z}$ allows for the most miniaturization. As the loaded DRAs became more miniaturized, reduced radiation efficiencies and narrowed impedance bandwidths were observed. In order to improve the efficiency and the bandwidth of the miniaturized antennas, two enhancement methods were applied: increasing the ring width, $w$, and the gap width, $g$. In the third section of this chapter, a $1\vec{x} \times 1\vec{y} \times 1\vec{z}$ SRR loaded DRA was fabricated and measured. The measurement results and the simulation results were compared, and the possible causes for the disagreements between the two results were analyzed.

From these studies, we summarized the following general design guidelines for this type of antenna:

1. For more miniaturization, one should increase the SRR length, $L_{SRR}$, and height, $H_{SRR}$, and decrease the SRR width, *w*, and gap width, *g*.

2. By varying SRR length and height, different SRR arrangements can be obtained. Miniaturization capability varies with ring arrangements, and the arrangement $1\vec{y} \times 1\vec{z}$ provides the most miniaturization.

3. The miniaturized DRAs with SRRs of different arrangements suffer from different degrees of performance deterioration, such as efficiency and bandwidth drop, both of which can be improved by properly increasing the ring trace width, *w*, and gap width, *g*.

4. A 3-D U-shaped ground plane enables gain and directivity enhancement and cross-polarization reduction in a split ring loaded DRA.

Metallization of different sides of DRA has been reported to be able to miniaturize unloaded conventional DRAs [23] [66]. The possibility of further miniaturizing SRR loaded DRAs by applying metallization on their surfaces will be investigated in the following chapter.

# Chapter 4

# Metallization of Split Ring Loaded Dielectric Resonator Antennas

It has been reported that adding metallic plates on the surfaces, such as top or side, of a conventional dielectric resonator antenna can reduce the size of the antenna [23] [66]. However, unlike a conventional DRA with an inherently dielectric material, an artificial magneto-dielectric resonator antenna is dependent on the interaction of metallic loops with the magnetic field to create artificial magnetism. Thus, it is crucial to have metallization that does not change the magnetic field distribution in the loaded DRA in order to maintain such electromagnetic interaction. According to the boundary condition of a perfect electric conductor (PEC), the normal component of the magnetic field is zero and there is only tangential component at the PEC boundary. In this case, since the magnetic field is in the x-axis Figure 4.1 (a), the magnetic field will not be affected as long as there is no metallization in the y-z plane, i.e. front and back surfaces of the DRA. In other words, the metallic plates can be placed on the top, bottom, left, and right side surfaces of the DRA, but not on the front and back surfaces of the DRA. By combining two or more of these metallic plates, different metallization configurations can be obtained. Among these combinations, two ring-shaped, namely U-shaped and split-ring-shaped, metallization configurations, as shown in Figure 4.1, are of particular interest and will be investigated in this chapter.
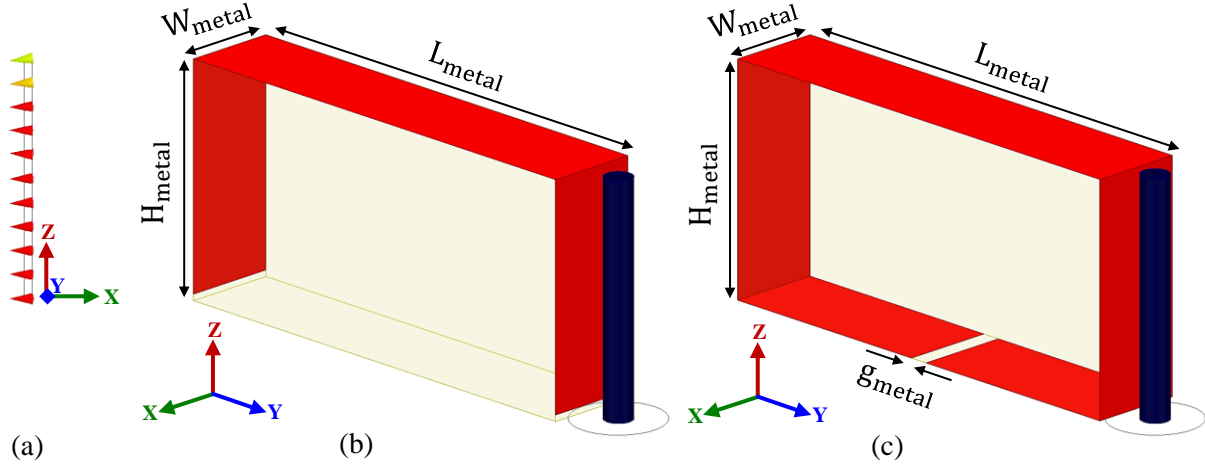
Figure 4.1 (a) Left side view of the magnetic field in both SRR loaded and unloaded DRAs. (b) U-shaped and (c) split-ring-shaped metallization on the host DRA: ▭ Host DRA (0.9 transparency); ▬ Metallization; ▬ Probe. $L_{metal} = L = 15$ mm, $H_{metal} = H - 0.2$ mm $= 7.3$ mm, $W_{metal} = W = 0.2$ mm, $g_{metal} = 0.2$ mm. Note that figure (b) and (c) are not to the scale.

Unlike traditional one or two sided metallic coatings, such ring-shaped metallization, just like the split ring inclusions, are capable of inducing permeability within the medium they enclose. Since there might be electromagnetic coupling and interactions between the SRR inclusions and the ring shaped metallization, the effect of them in a metallized SRR loaded DRA might be different than when they are individually applied to the host DRA. In order to find out such coupling effects, the host dielectric resonator antenna, loaded with only SRRs, only metallization, and the combination of both SRRs and metallization, is studied and compared with each other. In order to make the above discussion clearer, the possible antenna configurations are listed below:

① Host DRA

② Host DRA + SRRs

③ Host DRA + Metallization

④ Host DRA + SRRs + Metallization

By comparing ① with ②, and ① with ③, the independent miniaturization capability of the SRR

inclusions and the ring shaped metallization on the host DRA (conventional pure dielectric based

DRA) can be determined, respectively. By comparing ② with ④, the miniaturization capability

of the ring shaped metallization on the SRR loaded DRA can be found, while by comparing ③

with ④, the miniaturization capability of the SRR inclusions on the metallized DRA can be

found. The combined miniaturization capability of the SRR inclusions and ring shaped

metallization can be determined by comparing ① with ④. The first section of this chapter will

focus on the SRR loaded DRAs with U-shaped metallization, and the second section of this

chapter will discuss the SRR loaded DRAs with split-ring-shaped metallization.

**4.1    Split Ring Loaded Dielectric Resonator Antennas with U-shaped Metallization**

**I. Metallized Dielectric Resonator Antennas with Split Rings of Different Arrangements**

Figure 4.2 demonstrates the six SRR loaded dielectric resonator antennas covered with the U-

shaped metallic plates. By using the miniaturization capability evaluation method, the combined

miniaturization capabilities of the SRR inclusions of different arrangements and U-shaped

metallization can be obtained. The individual miniaturization capabilities of the SRR inclusions

and the U-shaped metallization are also provided and compared with the combined

miniaturization capability to demonstrate the extra miniaturization capability gained from the

addition of the other miniaturization technique, i.e., the U-shaped metallization and the SRR

inclusions, respectively. The individual miniaturization capability of the U-shaped metallization capability is obtained by using the miniaturization capability evaluation method defined in Chapter 3, and the individual miniaturization capabilities of the SRRs of different arrangements have been obtained in Chapter 3. The trace width and gap width of the SRR inclusions remain the same in all six metallized and non-metallized cases, i.e., w = 0.2 mm and g = 0.2 mm. The material used for the host dielectric resonator antenna is the same as in the previous chapter, i.e. Roger RT/duroid 5880 with a dielectric constant of 2.2 and loss tangent of 0.0009, and the dimensions of the host DRA also remain the same (L = 15 mm, H = 7.5 mm, and W = 0.254 mm).
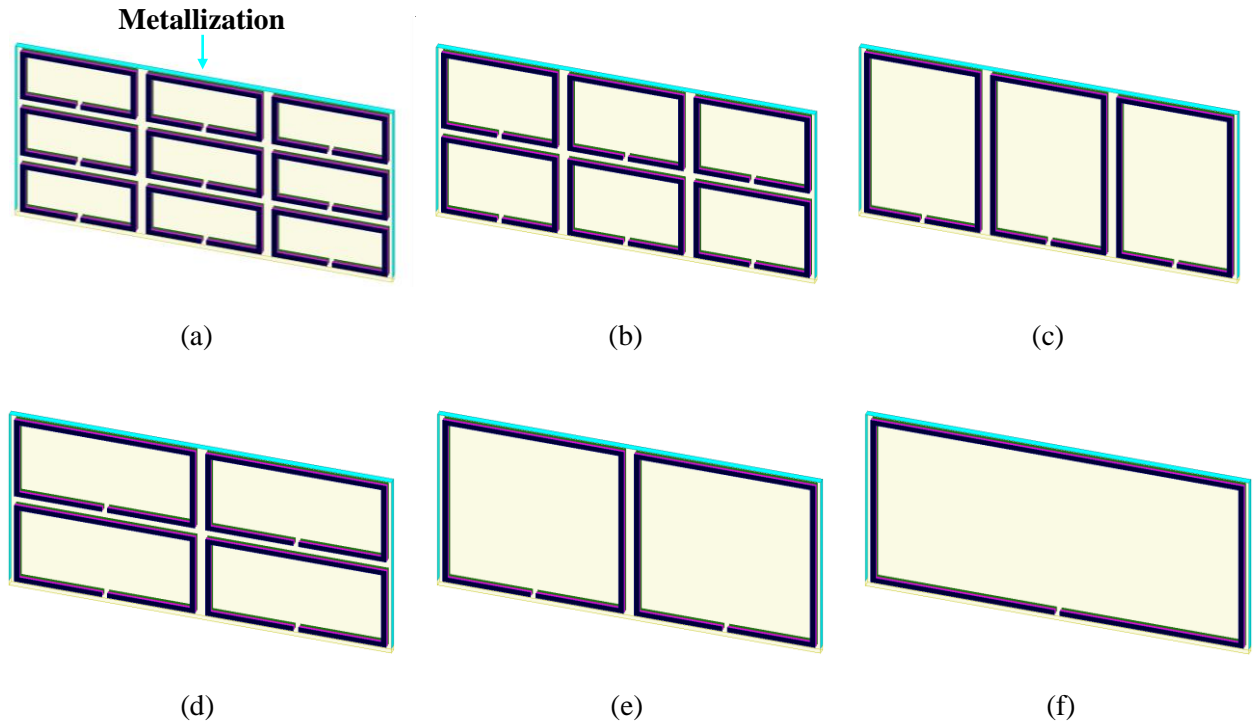


Figure 4.2 U-shaped metallization on split ring loaded DRAs: metallization ▬ ; host DRA ▬ (0.9 transparency); three identical layers of SRRs – front ▬, center ▬, and back ▬. (a) $3\vec{x} \times 3\vec{y} \times 3\vec{z}$, (b) $3\vec{x} \times 3\vec{y} \times 2\vec{z}$, (c) $3\vec{x} \times 3\vec{y} \times 1\vec{z}$, (d) $3\vec{x} \times 2\vec{y} \times 2\vec{z}$, (e) $3\vec{x} \times 2\vec{y} \times 1\vec{z}$, and (f) $3\vec{x} \times 1\vec{y} \times 1\vec{z}$.

Figure 4.3 illustrates the S11s of the metallized and non-metalized dielectric resonator antennas with SRR inclusions of different arrangements, and the metallized dielectric resonator antenna

without any SRRs. The black solid curve represents the U-shaped metallization coated host dielectric resonator antenna with no SRR inclusions, and it verifies that the U-shaped metallization can indeed miniaturize the conventional dielectric resonator antenna. The antenna performance comparisons of these metallized and non-metallized DRAs with different ring arrangements are demonstrated in Table 4.1.
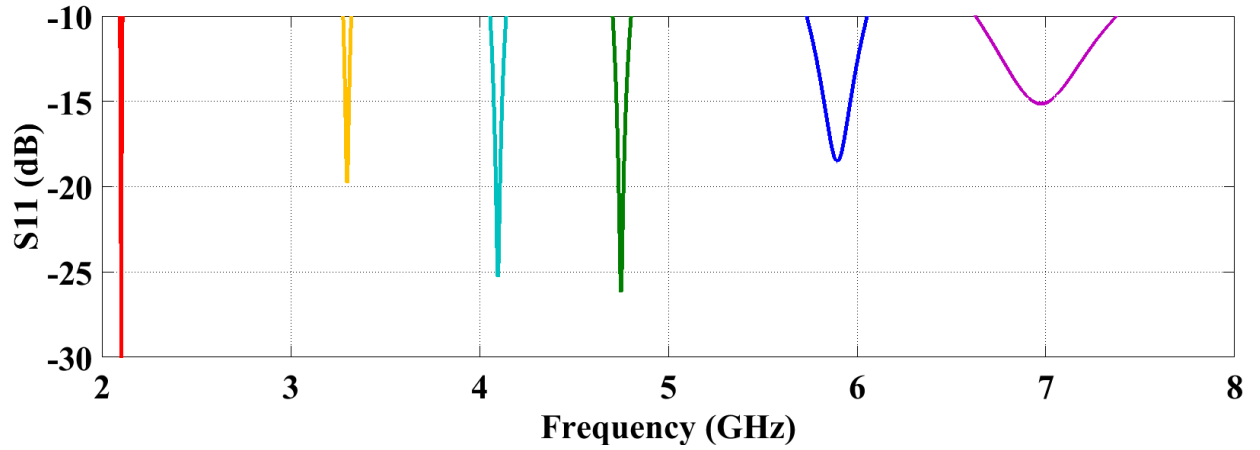


(a) Non-metalized
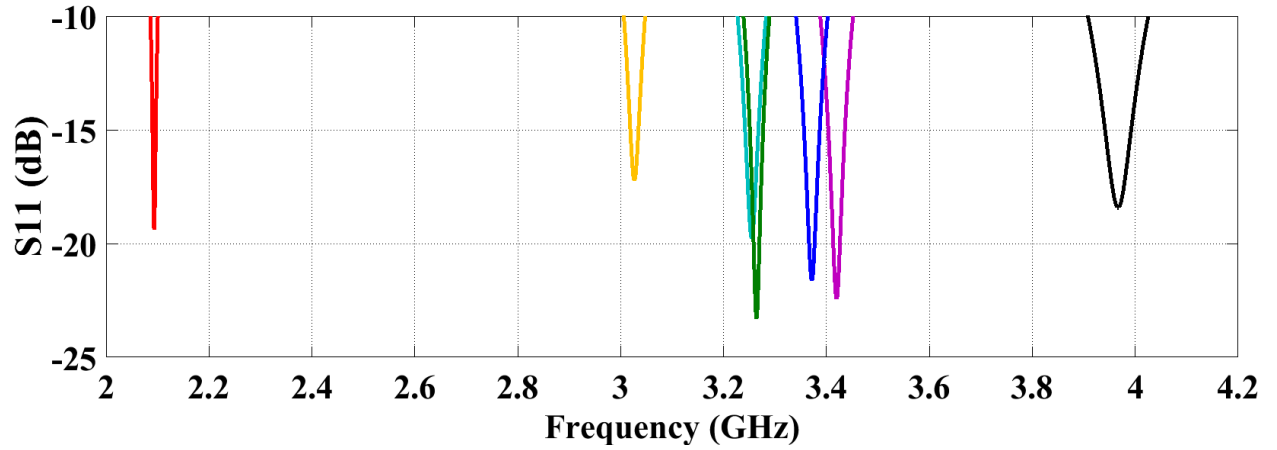


(b) Metalized

| | Metallization | $3\vec{x} \times 1\vec{y} \times 1\vec{z}$ | $3\vec{x} \times 2\vec{y} \times 1\vec{z}$ | $3\vec{x} \times 3\vec{y} \times 1\vec{z}$ | $3\vec{x} \times 2\vec{y} \times 2\vec{z}$ | $3\vec{x} \times 3\vec{y} \times 2\vec{z}$ | $3\vec{x} \times 3\vec{y} \times 3\vec{z}$ | No SRRs |
|---|---|---|---|---|---|---|---|---|
| (a) | No | — | — | — | — | — | — | |
| (b) | Yes | — | — | — | — | — | — | — |

Figure 4.3 S11 plots of the metallized and non-metallized split ring loaded DRAs with different SRR arrangements. (a) Non-metallized DRAs with SRRs. (b) Metallized DRAs with and without SRRs.

71

Table 4.1 Antenna Performance of the Metallized and Non-metallized DRAs with Different SRR Arrangements.

| SRR Arrangement | Metallization | w (mm) | g (mm) | $f_r$ (GHz) | BW (%) | η (%) | Gain (dBi) | X-pol (dB) | Dir (dBi) |
|---|---|---|---|---|---|---|---|---|---|
| No SRR | Yes | - | - | 3.9667 | 2.96 | 92.46 | 7.70 | -16.54 | 8.04 |
| $3\vec{x} \times 3\vec{y} \times 3\vec{z}$ | No | 0.2 | 0.2 | 6.9743 | 10.71 | 98.33 | 7.77 | -17.12 | 7.85 |
| | Yes | 0.2 | 0.2 | 3.4196 | 1.87 | 78.68 | 6.90 | -17.64 | 7.94 |
| $3\vec{x} \times 3\vec{y} \times 2\vec{z}$ | No | 0.2 | 0.2 | 5.8948 | 5.46 | 96.05 | 7.89 | -19.86 | 8.06 |
| | Yes | 0.2 | 0.2 | 3.3715 | 1.83 | 80.65 | 7.03 | -18.45 | 7.96 |
| $3\vec{x} \times 3\vec{y} \times 1\vec{z}$ | No | 0.2 | 0.2 | 4.0976 | 2.08 | 83.75 | 7.13 | -23.51 | 7.90 |
| | Yes | 0.2 | 0.2 | 3.2546 | 1.71 | 83.49 | 7.14 | -20.11 | 7.92 |
| $3\vec{x} \times 2\vec{y} \times 2\vec{z}$ | No | 0.2 | 0.2 | 4.861 | 2.20 | 79.43 | 6.59 | -16.02 | 7.59 |
| | Yes | 0.2 | 0.2 | 3.264 | 1.55 | 75.59 | 6.64 | -18.41 | 7.85 |
| $3\vec{x} \times 2\vec{y} \times 1\vec{z}$ | No | 0.2 | 0.2 | 3.2987 | 1.31 | 75.90 | 6.64 | -22.93 | 7.84 |
| | Yes | 0.2 | 0.2 | 3.0267 | 1.37 | 83.76 | 7.01 | -20.7 | 7.78 |
| $3\vec{x} \times 1\vec{y} \times 1\vec{z}$ | No | 0.2 | 0.2 | 2.1022 | 0.66 | 48.77 | 4.25 | -21.73 | 7.37 |
| | Yes | 0.2 | 0.2 | 2.0934 | 0.69 | 51.00 | 4.48 | -20.98 | 7.41 |

It shows that the addition of the U-shaped metallization to the unloaded host DRA is able to achieve slightly more miniaturization ($f_{r_{U\_metal}} = 3.9667$ GHz, $f_{r_{3\vec{x} \times 3\vec{y} \times 1\vec{z}}} = 4.0976$ GHz) than loading the host DRA with the SRRs of $3\vec{x} \times 3\vec{y} \times 1\vec{z}$ while providing a wider bandwidth ($BW_{U\_metal} = 2.96\%, BW_{3\vec{x} \times 3\vec{y} \times 1\vec{z}} = 2.08\%$) and higher radiation efficiency ($\eta_{U\_metal} = 92.46\%, \eta_{3\vec{x} \times 3\vec{y} \times 1\vec{z}} = 83.75\%$). The frequency shift between each pair of metallized and non-

metallized split ring loaded dielectric resonator antennas (i.e. same colored curves in Figure 4.3 (a) and (b)) indicates the extra miniaturization capability gained from the U-shaped metallization. It appears that the degree of frequency shift, i.e. the additional miniaturization capability (MC) gained from the addition of the U-shaped metallization, varies with SRR arrangements, and more specifically, is in the order of:

$$MC_{U\_metal@3\vec{x}\times3\vec{y}\times3\vec{z}} > MC_{U\_metal@3\vec{x}\times3\vec{y}\times2\vec{z}} > MC_{U\_metal@3\vec{x}\times2\vec{y}\times2\vec{z}} > MC_{U\_metal@3\vec{x}\times3\vec{y}\times1\vec{z}}$$

$$> MC_{U\_metal@3\vec{x}\times2\vec{y}\times1\vec{z}} > MC_{U\_metal@3\vec{x}\times1\vec{y}\times1\vec{z}}$$

where $MC_{U\_metal@3\vec{x}\times3\vec{y}\times3\vec{z}}$, $MC_{U\_metal@3\vec{x}\times3\vec{y}\times2\vec{z}}$, $MC_{U\_metal@3\vec{x}\times3\vec{y}\times1\vec{z}}$, $MC_{U\_metal@3\vec{x}\times2\vec{y}\times2\vec{z}}$, $MC_{U\_metal@3\vec{x}\times2\vec{y}\times1\vec{z}}$, and $MC_{U\_metal@3\vec{x}\times1\vec{y}\times1\vec{z}}$ are the extra miniaturization capabilities gained due to the U-shaped metallization at different SRR arrangements as indicated in their subscripts. It is interesting to notice that the miniaturization capability order of the U-shaped metallization on the split ring loaded dielectric resonator antennas is exactly the opposite of that of the non-metallized split ring loaded dielectric resonator antennas. In other words, the more the antenna is already miniaturized by the embedded SRRs, the less effective the U-shaped metallization will be at further miniaturizing the antenna. For instance, the non-metallized dielectric resonator antennas with the split rings of $3\vec{x}\times3\vec{y}\times3\vec{z}$ and $3\vec{x}\times1\vec{y}\times1\vec{z}$ have the lowest and highest miniaturization capabilities among the investigated six SRR arrangements, respectively, while the additions of the U-shaped metallization to the $3\vec{x}\times3\vec{y}\times3\vec{z}$ and $3\vec{x}\times1\vec{y}\times1\vec{z}$ split ring loaded dielectric resonator antennas provide the most and the least additional miniaturization, respectively. It is worth mentioning that although the additional miniaturization capability due to the U-shaped metallization reduces as the term *N\*A* increases while the miniaturization capability due to the SRR inclusions increases as the term *N\*A* increases, the overall

miniaturization capability of the combination of the metallization and the SRRs still increases as the term *N\*A* increases.

There are several possibilities that could lead to the situations stated above. In order to find the real reason, the current distributions of both metallized and non-metallized AMDRAs are plotted and compared, as shown in Figure 4.4. As can be seen, the additions of the U-shaped metallization increase the currents in the SRRs in all six antennas, but do not change the sequence of the magnitude of the currents. And the currents in the U-shaped metallic coatings indeed follow a decreasing sequence with respect to the term *N\*A*, and noticeably, the current in the metallization reduces to near-zero in the case of the one with $3\vec{x} \times 1\vec{y} \times 1\vec{z}$, which explains why the addition of the metallization is less effective as *N\*A* increases.



SRR Current Distribution    Metallization Current Distribution

(a1) Non-metallized    (a2) Metallized    (b1) Non-metallized    (b2) Metallized

(c1) Non-metallized    (c2) Metallized    (d1) Non-metallized    (d2) Metallized

(e1) Non-metallized      (e2) Metallized      (f1) Non-metallized      (f2) Metallized

(g) Metallized, no SRRs
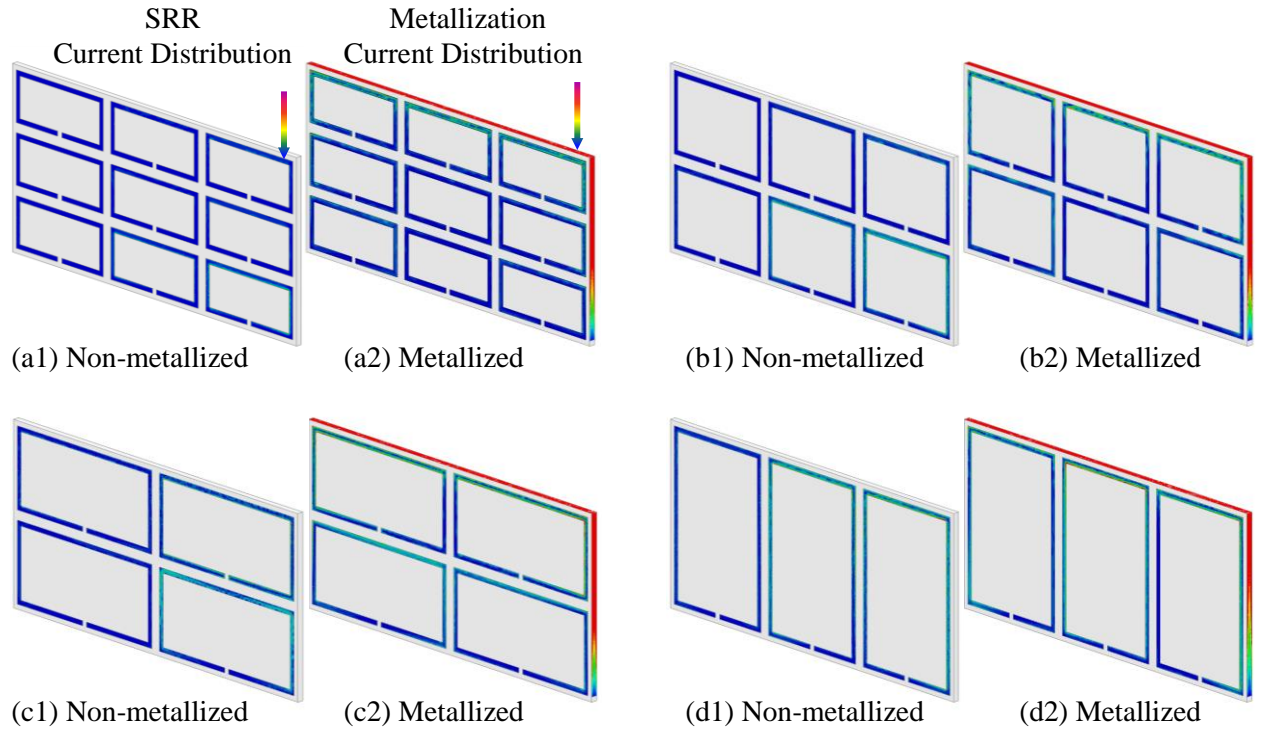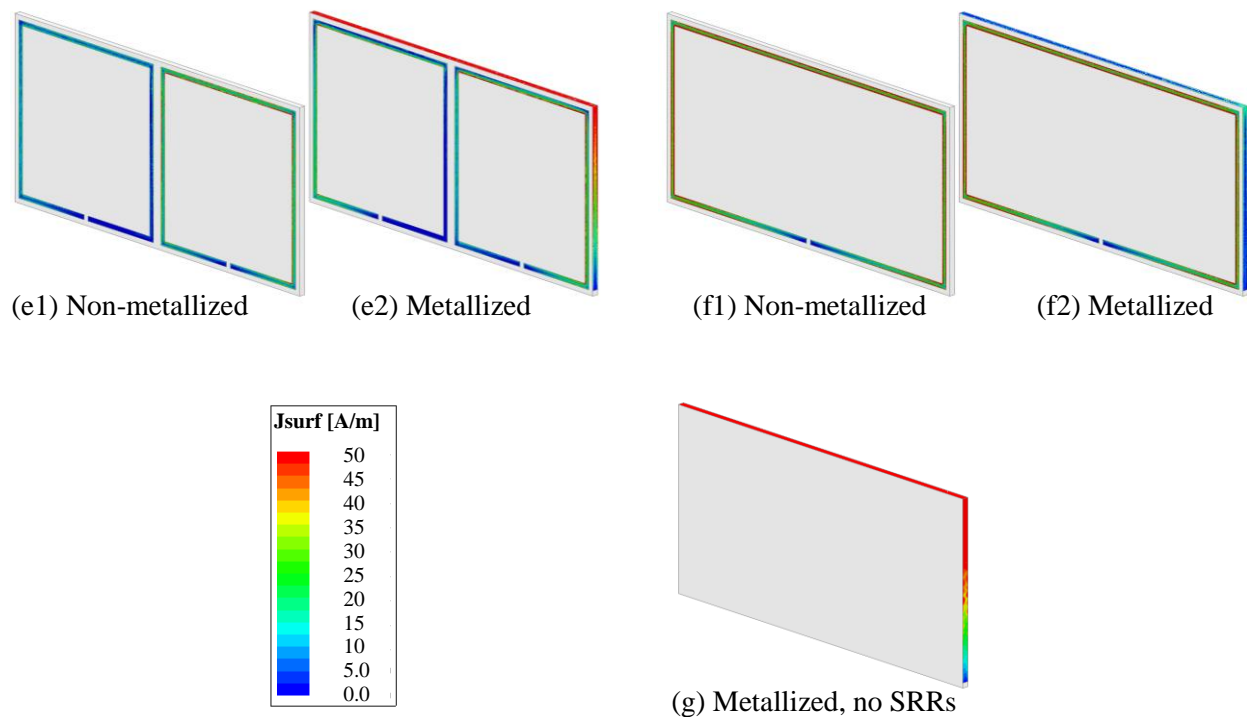
Figure 4.4 Current distribution on the SRRs and U-shaped metallization. (a1), (b1), (c1), (d1), (e1), and (f1) are non-metallized and (a2), (b2), (c2), (d2), (e2), and (f2) are metallized split ring loaded DRAs with split rings of $3\vec{x} \times 3\vec{y} \times 3\vec{z}$, $3\vec{x} \times 3\vec{y} \times 2\vec{z}$, $3\vec{x} \times 2\vec{y} \times 2\vec{z}$, $3\vec{x} \times 3\vec{y} \times 1\vec{z}$, $3\vec{x} \times 2\vec{y} \times 1\vec{z}$, and $3\vec{x} \times 1\vec{y} \times 1\vec{z}$, respectively. (g) The metallized DRA with no SRRs. The color key is shared by all the plots in this figure. The magnitude of the currents on the left side of the U-shaped metallization is the same as that of the right side in all cases, but is invisible because the host DRA is set to be opaque.

It is well known that the miniaturized antennas will suffer from deteriorated antenna performance, such as efficiency and bandwidth, due to the fundamental limitations of small antennas [1] [2]. However, interestingly enough, the addition of the U-shaped metallization does not necessarily degrade the antenna performance despite the antennas being successfully miniaturized. For example, the metallized DRA with $3\vec{x} \times 2\vec{y} \times 1\vec{z}$ SRRs is more miniaturized compared to the non-metallized DRA with the same ring arrangements, but has higher radiation efficiency and wider bandwidth (Figure 4.5). In order to demonstrate the effect of the U-shape metallization on the performance of the miniaturized antennas, the radiation efficiency and impedance bandwidth of both metallized and non-metallized DRAs with different ring

arrangements are plotted against the resonant frequency, as shown in Figure 4.5. More detailed comparisons of the performance of the metallized and non-metallized split ring loaded DRAs are given in Table 4.1.
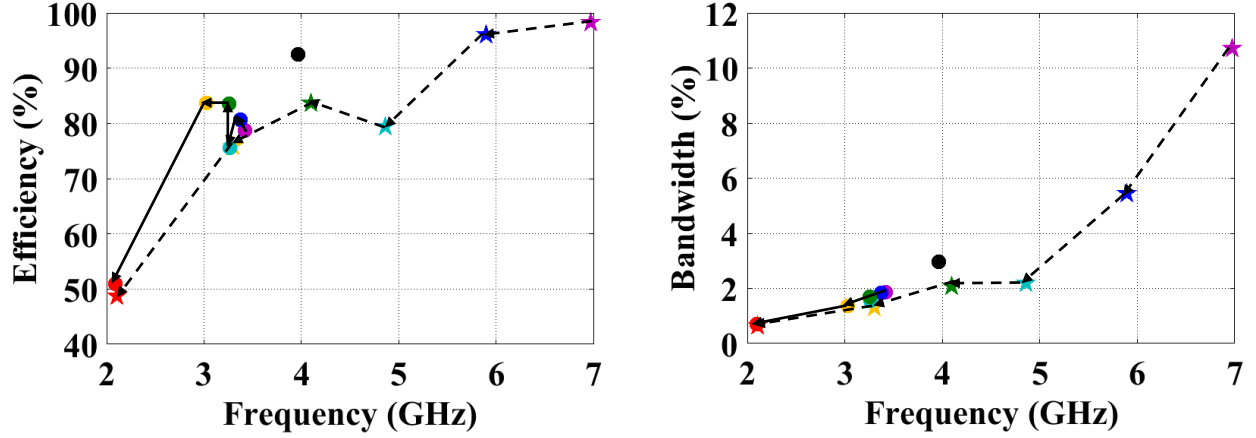


| | $3\vec{x} \times 1\vec{y} \times 1\vec{z}$ | $3\vec{x} \times 2\vec{y} \times 1\vec{z}$ | $3\vec{x} \times 3\vec{y} \times 1\vec{z}$ | $3\vec{x} \times 2\vec{y} \times 2\vec{z}$ | $3\vec{x} \times 3\vec{y} \times 2\vec{z}$ | $3\vec{x} \times 3\vec{y} \times 3\vec{z}$ | No SRRs |
|---|---|---|---|---|---|---|---|
| Non-metallized | ★ | ★ | ★ | ★ | ★ | ★ | |
| Metallized | ● | ● | ● | ● | ● | ● | ● |

Figure 4.5 Efficiency and bandwidth of the metallized and non-metallized DRAs with different SRR arrangements.

It is noted that the metallized DRA with $3\vec{x} \times 2\vec{y} \times 1\vec{z}$ SRRs provides the second largest miniaturization (MC=17.14x) with the best antenna performance in terms of efficiency ($\eta$=83.76%), while the one with $3\vec{x} \times 1\vec{y} \times 1\vec{z}$ SRRs provides the maximum miniaturization (MC=25.24x), but with a much lower radiation efficiency ($\eta$=51%). It has been shown in the previous chapter that the efficiency can be improved by increasing the SRR trace width, $w$, or the gap width, $g$, at the expanse of less miniaturization. However, one question still remains: will such sacrifice be small enough to maintain its best performance in terms of miniaturization capability while its efficiency is increased to be the same as that of the one with $3\vec{x} \times 2\vec{y} \times 1\vec{z}$ SRRs? In order to find the answer to the above question, a wider trace width is applied to the

metallized $3\vec{x} \times 1\vec{y} \times 1\vec{z}$ SRR loaded DRA such that the efficiency of the antenna reaches at least 83.76%. Through simulations, it is found that when the trace width is increased to 1.6 mm, the efficiency of the one with $3\vec{x} \times 1\vec{y} \times 1\vec{z}$ SRRs increases to 83.89 %, and the resonant frequency shifts up to 2.4793 GHz which is still much lower than that of the one with $3\vec{x} \times 2\vec{y} \times 1\vec{z}$ SRRs (Table 4.2). Therefore, it is reasonable to draw the conclusion that the metallized DRA with $3\vec{x} \times 1\vec{y} \times 1\vec{z}$ SRRs has the best performance among all six different SRR arrangements, as far as both miniaturization capability and efficiency are concerned. Although one should also notice that the bandwidth of the one with $3\vec{x} \times 1\vec{y} \times 1\vec{z}$ SRRs at trace width w = 1.6 mm is still narrower than that of the one with $3\vec{x} \times 2\vec{y} \times 1\vec{z}$ SRRs. Depending on applications, if a much wider bandwidth is preferred, one can continue increasing the trace width to meet the requirement, or choose other ring arrangements if the bandwidth is still not wide enough by increasing the trace width.

Table 4.2 Antenna Performance Comparison between the metallized DRAs loaded with 3 layers of $2\vec{y} \times 1\vec{z}$ SRRs and $1\vec{y} \times 1\vec{z}$ SRRs

| Arrangement | w (mm) | g (mm) | $f_r$ (GHz) | BW (%) | η (%) | Gain (dBi) | X-pol (dB) | Dir (dBi) | $\varepsilon_{r\_equivalent}$ | MC |
|---|---|---|---|---|---|---|---|---|---|---|
| $3\vec{x} \times 2\vec{y} \times 1\vec{z}$ | 0.2 | 0.2 | **3.0267** | 1.37 | **83.76** | 7.01 | -20.70 | 7.78 | 646 | **17.14** |
| $3\vec{x} \times 1\vec{y} \times 1\vec{z}$ | 1.6 | 0.2 | **2.4793** | 0.73 | **83.89** | 6.82 | -21.56 | 7.59 | 985 | **21.16** |

In the previous chapter, it was shown that the position of the SRR slit has an effect on the miniaturization capability of a split ring loaded DRA, and the slit position –z (bottom) allows for the most miniaturization among the four positions studied (i.e. +z (top), -z (bottom), -y (left), and +y (right)). However, it is uncertain if this statement is still true as the split ring loaded DRA is

covered with the U-shaped metallization. Thus, the following section will focus on the slit position study for the metallized split ring loaded DRAs.

**II. Metallized Split Ring Loaded Dielectric Resonator Antenna with Different Slit Positions**

The slit positions to be studied for the metallized split ring loaded DRAs are the same as in the non-metallized case, i.e. –z (bottom), +z (top), -y (left), and +y (right), as demonstrated in Figure 4.6. Since the relationship between the slit position and SRR arrangement has not been determined, the slit position study will be performed for all six different SRR arrangements.
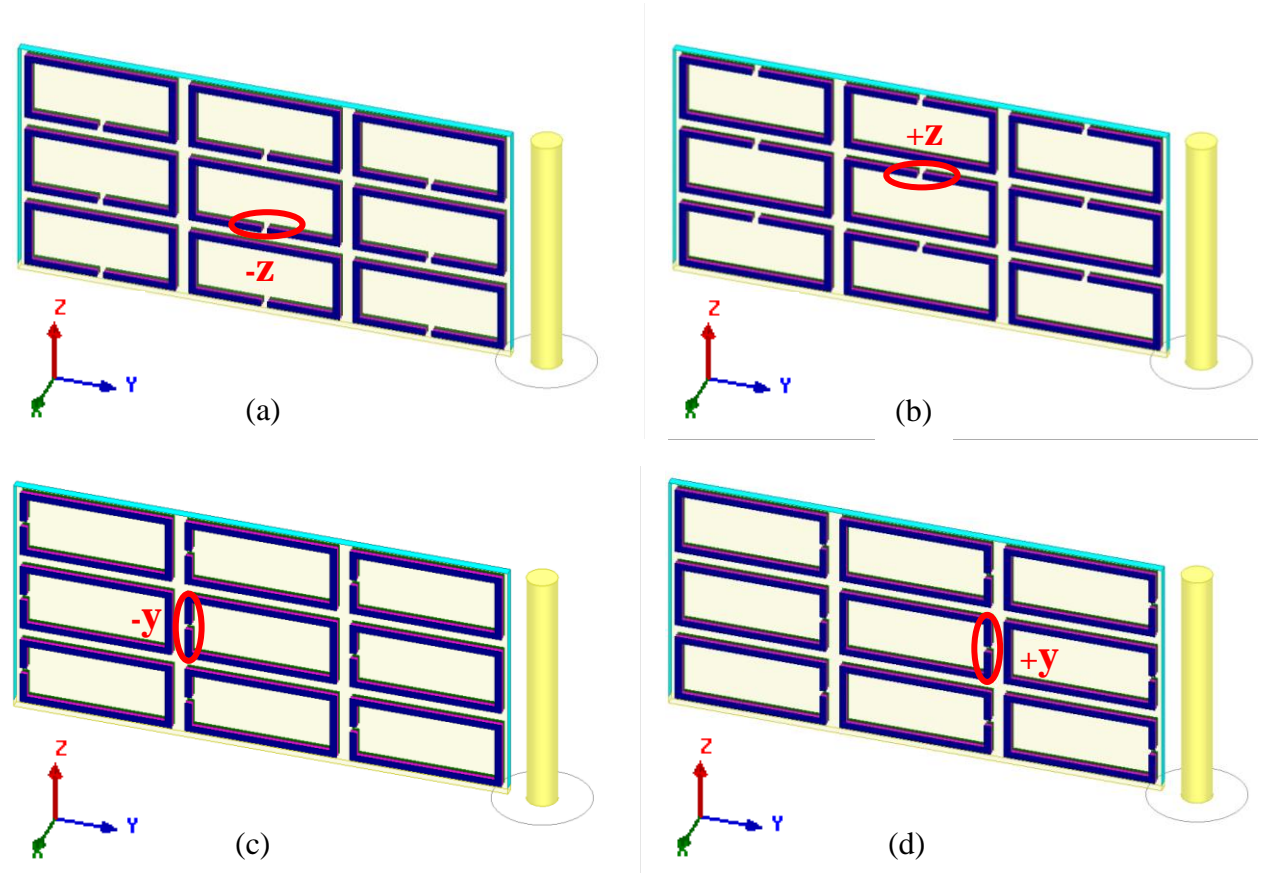


Figure 4.6 Metallized split ring loaded DRAs with different slit positions. (a) –z (bottom), (b) +z (top), (c) -y (left), and (d) +y (right). (metallization ▭; host DRA (0.9 transparency) and probe ▭; three identical layers of SRRs – front ▬, center ▬, and back ▬.)

The simulated antenna performance of each metallized split ring loaded DRA at the four slit positions is shown in Table 4.3, and is also plotted in Figure 4.7 for a more visual demonstration. As can be seen, the resonant frequency shifts as the slit position varies. And interestingly enough, five of the six SRR arrangements follow the same resonance shifting rule except for the arrangement of $3\vec{x} \times 1\vec{y} \times 1\vec{z}$, as summarized below:

$$
\begin{cases}
f_{r@+z} < f_{r@-y} \cong f_{r@+y} < f_{r@-z}, \text{Arrangement} = 3\vec{y} \times 3\vec{z}, 3\vec{y} \times 2\vec{z}, 3\vec{y} \times 1\vec{z}, 2\vec{y} \times 2\vec{z}\ 2\vec{y} \times 1\vec{z} \\
\\
f_{r@+z} < f_{r@-z} < f_{r@+y} < f_{r@-y}, \text{Arrangement} = 1\vec{y} \times 1\vec{z}
\end{cases}
$$

where $f_{r@-z}$, $f_{r@+z}$, $f_{r@-y}$, and $f_{r@+y}$ are resonance frequencies of the metallized split ring loaded DRAs with slits placed at –z, +z, -y, and +y, respectively. Although the arrangement $3\vec{x} \times 1\vec{y} \times 1\vec{z}$ follows a different rule than the rest, the lowest resonant frequency for all six arrangements occurs when the slits are placed at the top of the SRRs (+z), which is the exact opposite of the non-metallized split ring loaded DRAs whose lowest resonance is obtained by placing the slits at the bottom of the SRRs (-z). Theoretically, since the inclusion parameters and the metallization remain the same in each arrangement, such frequency shifts should be caused by the changes in the currents in the metallization and SRRs. In order to verify this analysis, current distributions of the metallization and SRRs at different slit positions are plotted and compared. Two SRR arrangements, namely $3\vec{x} \times 2\vec{y} \times 1\vec{z}$ and $3\vec{x} \times 1\vec{y} \times 1\vec{z}$, and two slit positions, namely –z and +z, are used as examples to demonstrate the variations in currents as the slit position changes. As expected, in both cases, the currents in both metallization and SRRs are higher when the slits are placed at the top of the rings (+z), as shown in Figure 4.8. Although the slit position +z allows for the most miniaturization in all cases, it can worsen the antenna performance to a degree that one may find unacceptable in some cases. For example, for the

arrangement $3\vec{x} \times 2\vec{y} \times 1\vec{z}$, compared to the slit position –z, slit position +z can reduce the resonant frequency by 0.4039 GHz, however, at the expense of losing 24.2% radiation efficiency (from 83.76% to 59.56%) and 1.94 dB gain (from 7.01 dBi to 5.07 dBi). Similarly, for the arrangement $3\vec{x} \times 1\vec{y} \times 1\vec{z}$, the price of lowering the resonant frequency by 0.2891 GHz is 17.97% radiation efficiency (from 51% to 33.03%) and 2.35 dB gain (from 4.48 dBi to 2.13 dBi) drop. Therefore, one has to decide if such antenna performance degradation is acceptable for an exchange of antenna size reduction depending on their applications.

Table 4.3 Antenna Performance VS. Slit Positions for All Six SRR Arrangements

| Arrangement | Slit Position | $f_r$ (GHz) | BW (%) | η (%) | Gain (dBi) | X-pol (dB) | Dir (dBi) |
|---|---|---|---|---|---|---|---|
| $3\vec{x} \times 3\vec{y} \times 3\vec{z}$ | -z | 3.4196 | 1.87 | 78.68 | 6.90 | -17.64 | 7.94 |
| | +z | 3.2449 | 1.63 | 74.78 | 6.55 | -18.03 | 7.81 |
| | -y | 3.3407 | 1.82 | 78.02 | 6.65 | -16.35 | 7.73 |
| | +y | 3.3396 | 1.75 | 76.76 | 6.84 | -19.23 | 7.99 |
| $3\vec{x} \times 3\vec{y} \times 2\vec{z}$ | -z | 3.3715 | 1.83 | 80.65 | 7.03 | -18.45 | 7.96 |
| | +z | 3.1046 | 1.50 | 73.09 | 6.37 | -18.3 | 7.73 |
| | -y | 3.2554 | 1.76 | 77.51 | 6.47 | -15.61 | 7.56 |
| | +y | 3.2569 | 1.63 | 76.17 | 6.85 | -21.89 | 8.04 |
| $3\vec{x} \times 3\vec{y} \times 1\vec{z}$ | -z | 3.2546 | 1.71 | 83.49 | 7.14 | -20.11 | 7.92 |
| | +z | 2.7875 | 1.21 | 68.53 | 5.91 | -20.12 | 7.55 |
| | -y | 3.0367 | 1.57 | 78.23 | 6.10 | -13.8 | 7.16 |
| | +y | 3.0341 | 1.43 | 76.12 | 6.73 | -33.02 | 7.91 |
| $3\vec{x} \times 2\vec{y} \times 2\vec{z}$ | -z | 3.2640 | 1.55 | 75.59 | 6.64 | -18.41 | 7.85 |
| | +z | 2.8601 | 1.19 | 65.35 | 5.66 | -18.3 | 7.50 |
| | -y | 3.0933 | 1.53 | 74.34 | 6.02 | -14.43 | 7.31 |
| | +y | 3.0592 | 1.40 | 72.07 | 6.56 | -24.78 | 7.98 |
| $3\vec{x} \times 2\vec{y} \times 1\vec{z}$ | -z | 3.0267 | 1.37 | 83.76 | 7.01 | -20.7 | 7.78 |
| | +z | 2.4696 | 0.95 | 59.56 | 5.07 | -20.14 | 7.32 |
| | -y | 2.8284 | 1.30 | 73.36 | 5.37 | -12.25 | 6.71 |
| | +y | 2.8229 | 1.18 | 71.68 | 6.22 | -23.08 | 7.66 |
| $3\vec{x} \times 1\vec{y} \times 1\vec{z}$ | -z | 2.0934 | 0.69 | 51.00 | 4.48 | -20.98 | 7.41 |
| | +z | 1.8043 | 0.66 | 33.03 | 2.13 | -20.65 | 6.95 |
| | -y | 2.2369 | 1.06 | 54.52 | 2.55 | -7.63 | 5.19 |
| | +y | 2.1543 | 0.83 | 48.68 | 3.47 | -13.15 | 6.60 |
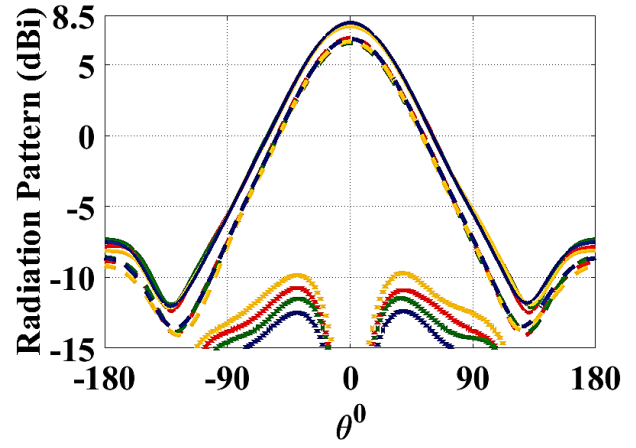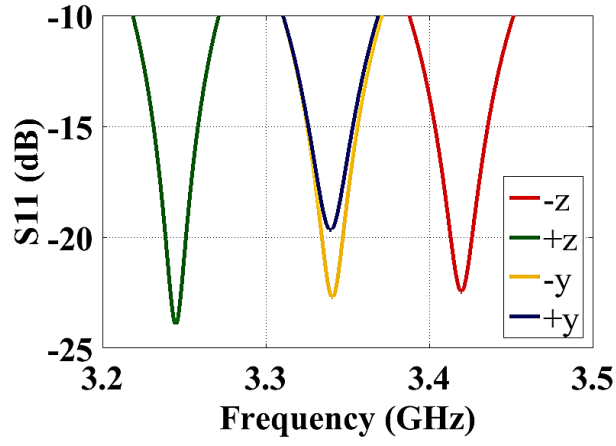
(a) $3\vec{x} \times 3\vec{y} \times 3\vec{z}$
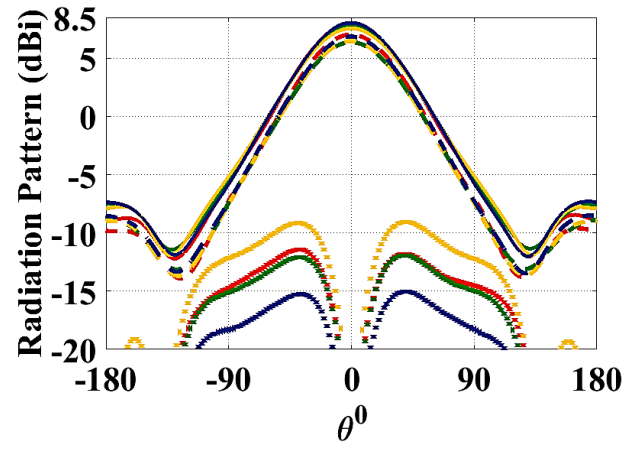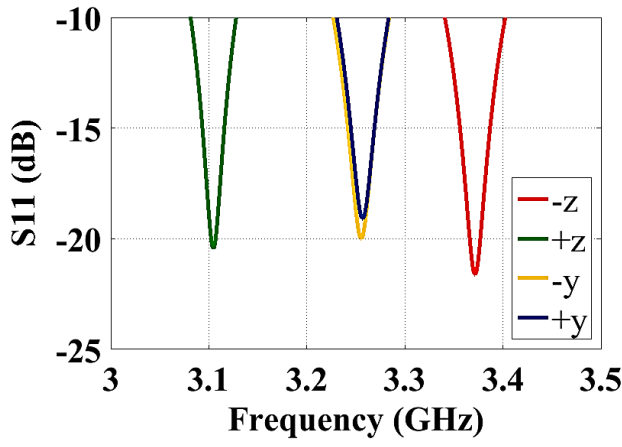


(b) $3\vec{x} \times 3\vec{y} \times 2\vec{z}$
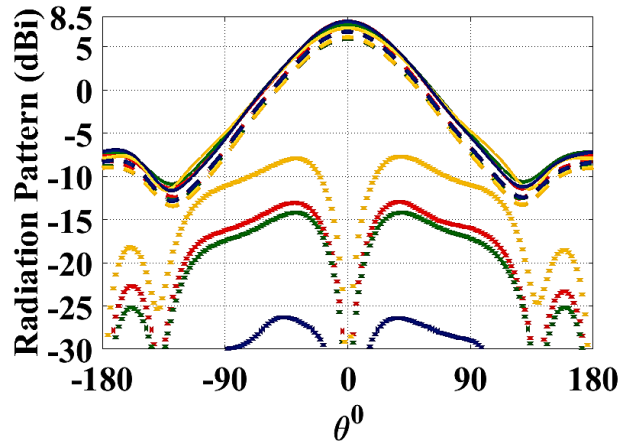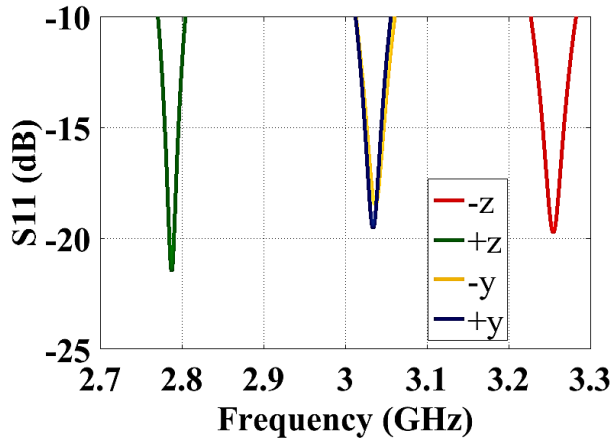


(c) $3\vec{x} \times 3\vec{y} \times 1\vec{z}$
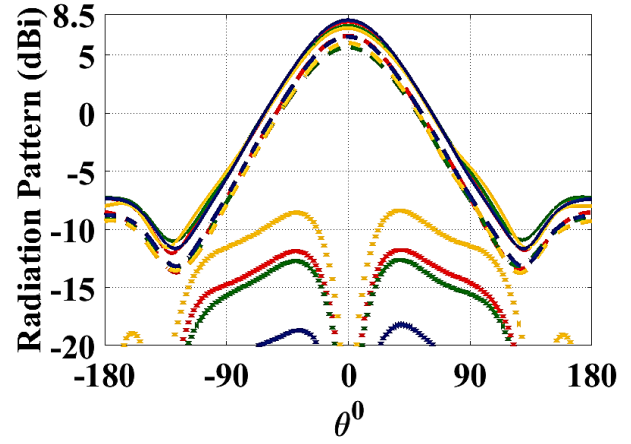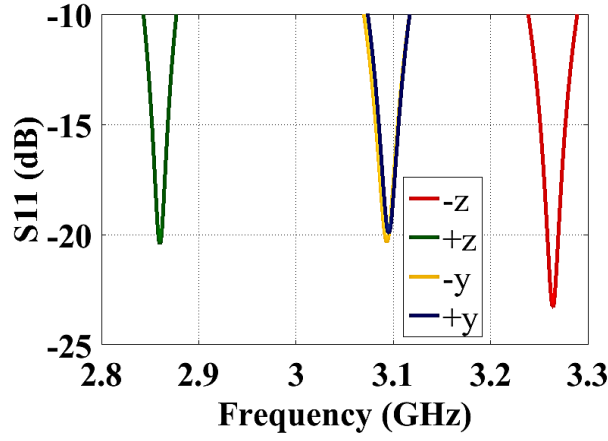
(d) $3\vec{x} \times 2\vec{y} \times 2\vec{z}$
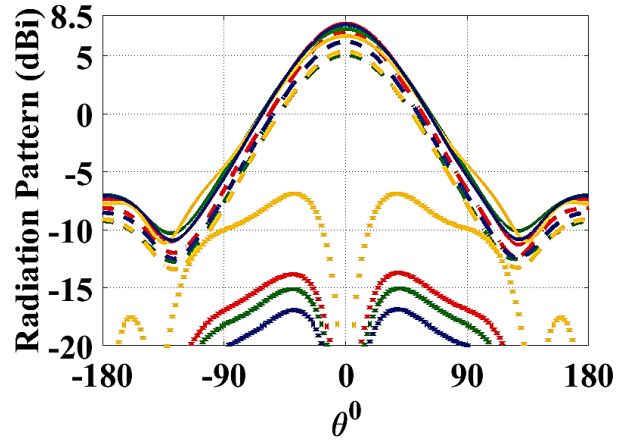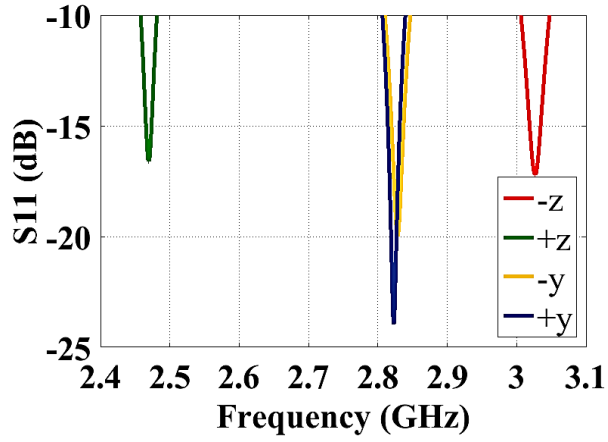
(e) $3\vec{x} \times 2\vec{y} \times 1\vec{z}$
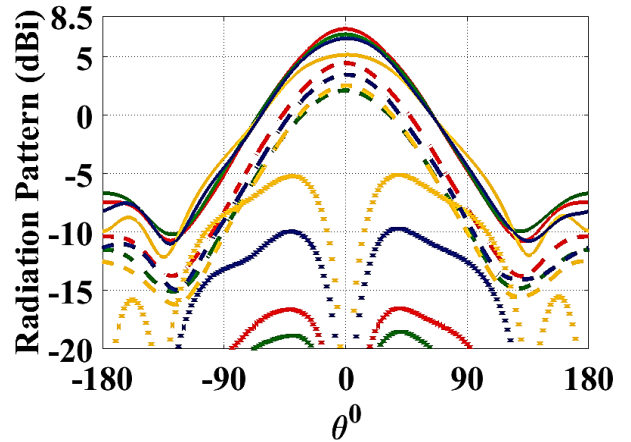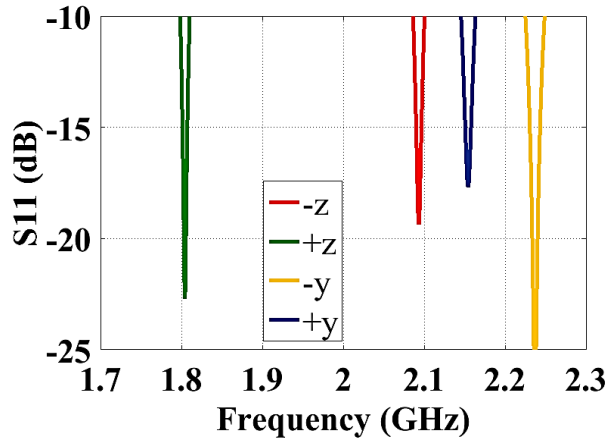
(f) $3\vec{x} \times 1\vec{y} \times 1\vec{z}$

| Slit Position: -z | Slit Position: +z | Slit Position: -y | Slit Position: +y |
|---|---|---|---|
| — Dir  -- Gain  x X-pol | — Dir  -- Gain  x X-pol | — Dir  -- Gain  x X-pol | — Dir  -- Gain  x X-pol |

Figure 4.7 The effect of the slit position on the metallized DRAs with SRRs of different arrangements: (a) $3\vec{x} \times 3\vec{y} \times 3\vec{z}$, (b) $3\vec{x} \times 3\vec{y} \times 2\vec{z}$, (c) $3\vec{x} \times 3\vec{y} \times 1\vec{z}$, (d) $3\vec{x} \times 2\vec{y} \times 2\vec{z}$, (e) $3\vec{x} \times 2\vec{y} \times 1\vec{z}$, and (f) $3\vec{x} \times 2\vec{y} \times 1\vec{z}$.



(a1)                                   (a2)

(b1)                                   (b2)
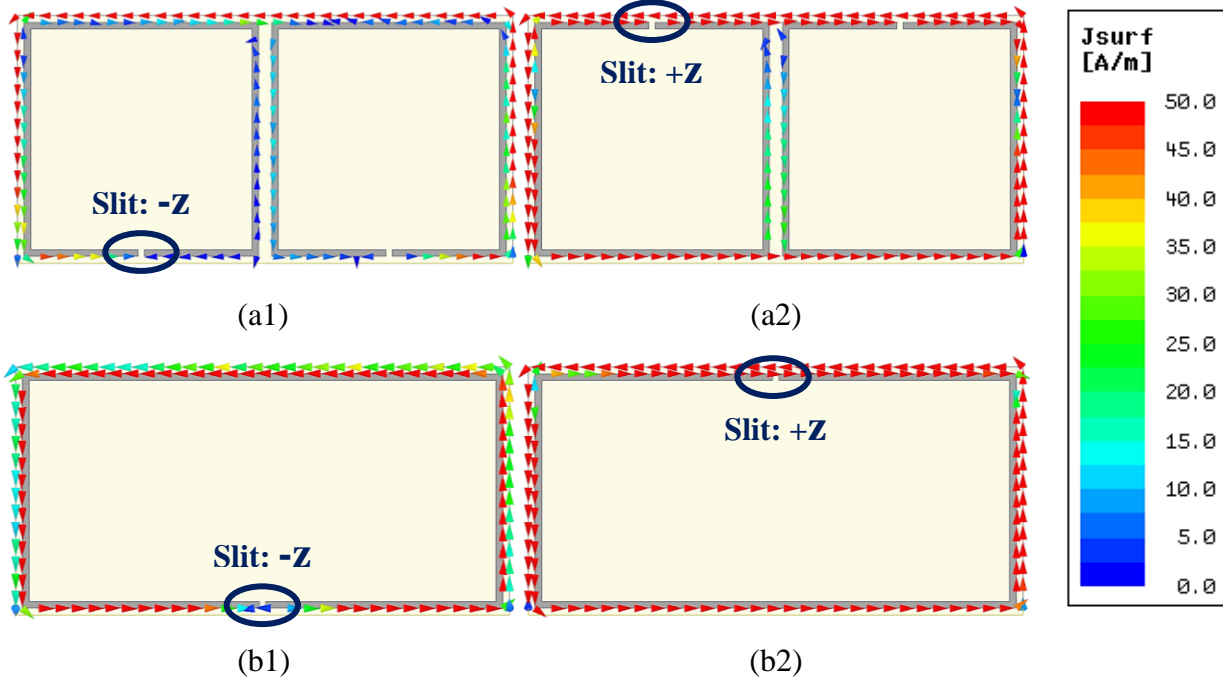
Figure 4.8 Current distribution of the U-shaped metallization and SRRs in the metallized split ring loaded DRAs with (a1) ring arrangement of $3\vec{x} \times 2\vec{y} \times 1\vec{z}$ and slit position of –z, (a2) ring arrangement of $3\vec{x} \times 2\vec{y} \times 1\vec{z}$ and slit position of +z, (b1) ring arrangement of $3\vec{x} \times 1\vec{y} \times 1\vec{z}$ and slit position of –z, and (b2) ring arrangement of $3\vec{x} \times 1\vec{y} \times 1\vec{z}$ and slit position of +z.

It is interesting to notice that the arrangement $3\vec{x} \times 1\vec{y} \times 1\vec{z}$ not only does not follow the same frequency shift rule as the other arrangements, but also does not follow the same cross-polarization rule (see Figure 4.7) as shown below:

$$\begin{cases} Xpol_{+y} < Xpol_{+z} < Xpol_{-z} < Xpol_{-y}, \text{Arrangement} = 3\vec{y} \times 3\vec{z}, 3\vec{y} \times 2\vec{z}, 3\vec{y} \times 1\vec{z}, 2\vec{y} \times 2\vec{z} \ 2\vec{y} \times 1\vec{z} \\ \\ Xpol_{+z} < Xpol_{-z} < Xpol_{+y} < Xpol_{-y}, \text{Arrangement} = 1\vec{y} \times 1\vec{z} \end{cases}$$

As can be seen, the lowest cross-polarization level of the other five arrangements occurs when the slits are placed on the right side of the SRRs (+y), while that of the $3\vec{x} \times 1\vec{y} \times 1\vec{z}$ occurs when the slits are placed at the top of the SRRs (+z). Despite all these differences, all of the six arrangements have one thing in common, that is, placing the slits on the left side of the SRRs (-y) provides the lowest directivity and highest cross-polarization while does not offer better performance on other antenna parameters. A variation in directivity is observed for different arrangements with the same slit position, and it is mostly due to the ground plane side wall height being different. More specifically, the side wall heights were set to be the same, i.e. 15 mm, for all arrangements, but the resonance frequencies varies with the ring arrangements, leading to unequal electrical side wall heights for various arrangements.

## 4.2  Split Ring Loaded Dielectric Resonator Antennas with Split-Ring-Shaped Metallization

The previous section has demonstrated that extra size reduction of a split ring loaded antenna can be achieved by applying a U-shaped metallization on the surfaces of the antenna. In this section, the possibility of further reducing the antenna size by using a split-ring-shaped metallization, as shown in Figure 4.9, is investigated. Unlike the U-shaped metallization, split-ring-shaped metallization also covers the bottom surface of the split ring loaded DRA. As demonstrated in the previous section, the metallization itself is also capable of inducing permeability, and thus, miniaturizing the metallization can improve the overall miniaturization capability of the antenna. And the miniaturization of the metallization is achieved by adding a slit to the bottom of the metallization. Since the arrangement $3\vec{x} \times 1\vec{y} \times 1\vec{z}$ provides more miniaturization than the other

arrangements, it will be used as an example in this investigation to demonstrate the possible miniaturization capability gained by the addition of the split-ring-shaped metallization. In order to estimate the miniaturization capability of the split-ring-shaped metallization, both the loaded DRA with $3\vec{x} \times 1\vec{y} \times 1\vec{z}$ SRRs (ring width $w = 1.6\ mm$, gap width $g = 0.2\ mm$) and unloaded DRA are covered with the metallization. Since the bottom surface of the antenna is also metallized, the antenna has to be lifted to be above the ground plane at a distance, $h$, so that the antenna is not shorted to the ground plane. In order to achieve such insolation, one can either choose to simply lift up the antenna and let the air fill the gap, or use any other dielectric materials to fill the gap. Here, air is used as the insolating layer. In order to investigate the effect of the air gap, antennas are lifted to various heights above the ground plane. Table 4.4 demonstrates the antenna performance of the SRR loaded and unloaded DRAs with the split-ring-shaped metallization. It is obvious that both bandwidth and efficiency increase with the increasing air gap, however, at the expanse of reducing miniaturization capability. Unlike loading the SRR loaded DRAs with U-shaped metallization, the addition of the split-ring-shaped metallization dramatically reduces the efficiency of the SRR loaded DRA even when little miniaturization is obtained by adding SRR inclusions. For instance, an unloaded metallized antenna has an efficiency of 82.63% and bandwidth of 1.84%, and its loaded counterpart only has an efficiency of 43.32% (39.31% efficiency drop) while the extra miniaturization due to the inclusions is quite small (~0.2 GHz). Therefore, it is reasonable to draw the conclusion that an split-ring-shaped metallization coated DRA is better without the SRR inclusions, because the negative effects due to the inclusions are far greater than the positive effects.
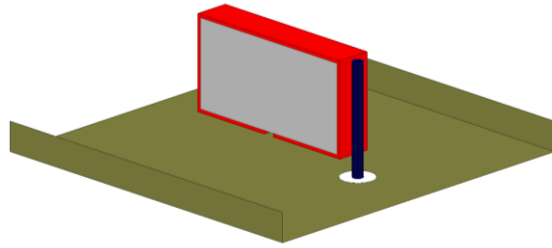
(a) Metallized DRA without SRRs
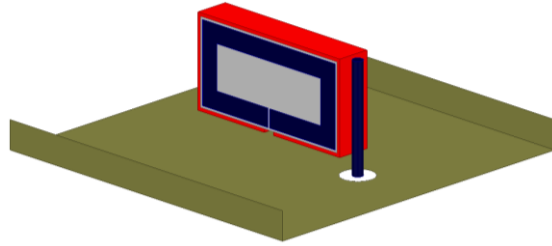
(b) Metallized DRA with $3\vec{x} \times 1\vec{y} \times 1\vec{z}$ SRRs
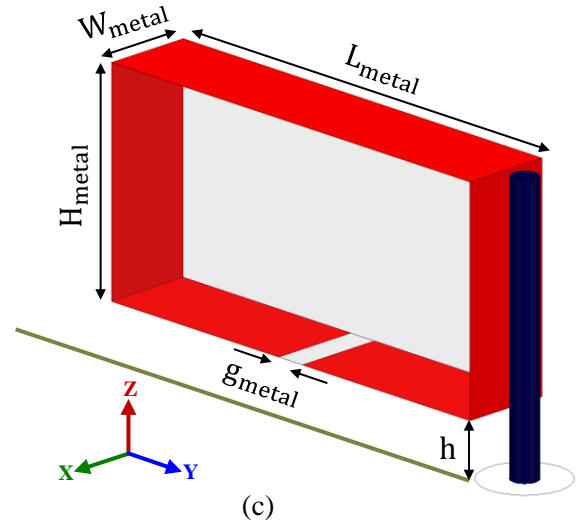
(c)

Figure 4.9 Metallized DRAs (a) with and (b) without SRRs. (c) Split-ring-shaped metallization. Note that figures are not to the scale. $L_{metal}$ = L = 15 mm, $H_{metal}$ = H − 0.2 mm = 7.3 mm, $W_{metal}$ = W = 0.2 mm, $g_{metal}$ = 0.2 mm. (� Host DRA (0.9 transparency in (c)); ▰ Metallization; ▰ SRRs and Probe; ▰ Ground plane.)

Table 4.4 Antenna Performance of the Split-Ring-Shaped Metallization on the Loaded and Unloaded DRAs.

| SRR Inclusions | h (mm) | $g_{metal}$ (mm) | w (mm) | g (mm) | $f_r$ (GHz) | BW (%) | η (%) | Gain (dBi) | X-pol (dB) | Dir (dBi) |
|---|---|---|---|---|---|---|---|---|---|---|
| No | 0.1 | 0.2 | - | - | 1.932 | 0.76 | 39.90 | 3.21 | -21.19 | 7.20 |
| No | 1 | 0.2 | - | - | 2.6801 | 1.28 | 71.77 | 6.06 | -17.12 | 7.50 |
| No | 2 | 0.2 | - | - | 2.7985 | 1.54 | 78.73 | 6.38 | -15.39 | 7.44 |
| No | 3 | 0.2 | - | - | 2.8382 | 1.84 | 82.63 | 6.33 | -13.33 | 7.16 |
| Yes, $3\vec{x} \times 1\vec{y} \times 1\vec{z}$ | 3 | 0.2 | 1.6 | 0.2 | 2.6127 | 1.63 | 43.32 | 2.53 | -10.41 | 6.17 |

87

## 4.3  Summary

Top surface and/or side surface metallizations have been previously used for conventional DRA miniaturization [23] [66]. In this chapter, the possibility of miniaturizing SRR loaded DRAs by using this technique, i.e. metallization, was investigated. Two types of ring shaped metallization, namely, U-shaped and split-ring-shaped metallization, were investigated. The ring shaped metallization was chosen for the following two reasons:

- Such metallization does not interfere with the magnetic field, and thus does not interfere with the electromagnetic interaction between the SRR inclusions and the magnetic field.

- Such metallization itself is capable of inducing permeability, and thus can more effectively miniaturize DRAs with or without SRRs.

The U-shaped metallization was studied in the first section of this chapter, and it was applied to both SRR loaded and unloaded DRAs. The simulation results verified that the U-shaped metallization alone can indeed effectively miniaturize a conventional DRA without much performance degradation. And extra miniaturization was also observed in SRR loaded DRAs, except for one ring arrangement, namely $3\vec{x} \times 1\vec{y} \times 1\vec{z}$. Despite no extra miniaturization gained from the addition of the U-shaped metallization, the one with $3\vec{x} \times 1\vec{y} \times 1\vec{z}$ SRRs still remains the most miniaturized among all six arrangements.

The second section studied the effect of the split-ring-shaped metallization on an unloaded conventional DRA and a loaded DRA with $3\vec{x} \times 1\vec{y} \times 1\vec{z}$ SRRs. It was found that although the split-ring-shaped metallization does not add much miniaturization to the SRR loaded DRA, it can significantly degrade the antenna performance. However, a significant miniaturization was observed when there was no SRR inclusion. Unlike the metallized loaded DRA, the antenna

performance of the metallized unloaded DRA can be easily improved. With all other antenna parameters remaining the same, the performance improvement could be easily achieved by increasing the air gap, $h$, between the ground plane and the metallization.

Since the split-ring-shaped metallization has demonstrated the ability of working as a more efficient antenna on its own, it is interesting to conduct a more detailed study on it as an individual antenna. And this will be done in the following chapter.

# Chapter 5

# Probe-fed Flat-wire Open Ring Antennas

In the previous chapter, it was shown that the split ring shaped metallization performs better when there is no inclusion in the host DRA. In other words, the split ring shaped metallization itself can act as an antenna on its own. In this chapter, such split ring shaped metallization will be investigated and referred to as probe-fed flat-wire open ring antenna in the following context. Unlike the previous designs, the host medium used for this flat-wire open ring antenna is air such that the antenna can be easily fabricated by using either folding or milling techniques. Firstly, a single-turn flat-wire open ring antenna is studied. In order to better understand this antenna, parametric studies on the ring and the ground plane are performed. Secondly, to further reduce the antenna size, a two-turn flat-wire open ring antenna is proposed and studied, and different combinations of the outer and inner ring slit positions are also investigated.

## 5.1 Single-Turn Flat-wire Open Ring Antenna

Figure 5.1 shows a single-turn flat-wire open ring antenna, made of copper and placed above a U-shaped ground plane at a distance, $h$. The reason for the use of a U-shaped ground is the same as stated in previous chapters, i.e. gain enhancement and cross-polarization reduction. In order to investigate the effect of each antenna parameter on the antenna performance, parametric studies on the ring length ($L$), ring height ($H$), ring width ($W$), slit width ($w_{slit}$) and air gap ($h$) are conducted. Because of the asymmetry of the feeding probe, the effect of the slit position is also investigated. The ground plane dimensions for all the antenna parametric studies are set to be the

optimal ground plane dimensions, namely $L_{ground} = 1.2\lambda$ and $H_{side\,wall} = 0.36\lambda$, which are obtained based on the same technique as in Chapter 3. Although optimal ground plane dimensions allow for the highest gain, it is not always worth increasing the ground plane size straight to the optimal values, and in some cases the highest gain is also not required. Therefore, in order to form a more informed design guideline, the relationship between the ground plane size and the gain performance is investigated at the end of this section.
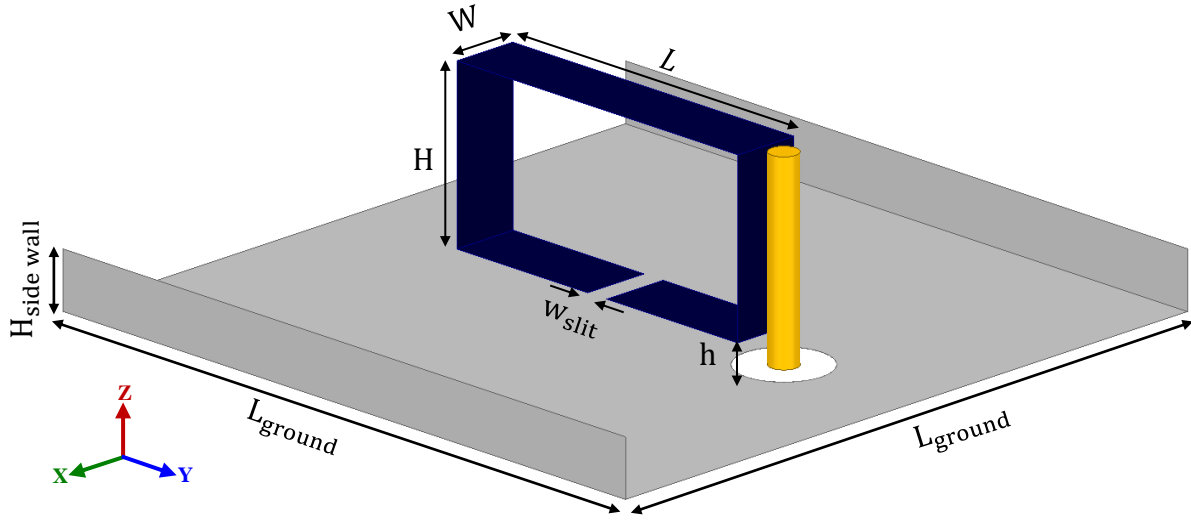


Figure 5.1 Probe-fed single-turn flat-wire open ring antenna.

## I. Parametric Studies on Ring Parameters

The parameters to be studied are listed in Table 5.1 and the corresponding simulation results are also given in the table. It shows that an increase in the ring length, $L$, and ring height, $H$, can reduce the resonant frequency of the antenna, which are expected because an increase in either of them will lead to a larger ring circumference, and thus a lower resonant frequency.

Interestingly, it is found that the ring width, $W$, is a very sensitive parameter that can be used to adjust the resonant frequency. With the given dimensions, an increase in the ring width by only 1 mm is able to reduce the resonant frequency by 0.28 GHz, while the resonant frequency only shifts down by less than 0.14 GHz when the ring length or the ring height is increased by 1 mm. Unlike the ring length and the ring height, the ring width does not degrade the antenna gain and efficiency for the gained miniaturization. On the contrary, it can improve the gain and efficiency, but at the expense of a slightly reduced bandwidth. For instance, as the ring width increases from 0.5 mm to 1.5 mm, improvements in both gain (0.5 dB) and efficiency (9.4%) are observed and the resonant frequency shifts from 2.5431 GHz to 2.2676 GHz. Such miniaturization due to an increased ring width, $W$, can be understood from the following aspect:

- An increase in the ring width leads to a larger capacitance in the ring slit and thus a reduced resonant frequency.

The slit width study shows that the resonant frequency increases with the increase in the slit width, $w_{slit}$. For example, as the slit width increases from 0.2 mm to 2.2 mm, the resonant frequency shifts up by 0.173 GHz. This is expected because an increase in the slit width leads to a shortened ring circumference and a reduced capacitance in the slit, both of which can cause the resonant frequency to go up.

The air gap, $h$, between the ring and the ground plane is also found to be a very sensitive parameter that can be used to adjust the resonant frequency. An increase of only 0.1 mm in the air gap can result in a resonant frequency shift of more than 0.1 GHz. It also shows that the radiation efficiency can be improved by increasing the air gap, but the degree of improvement

decreases with the increase in the air gap. For example, for the first 0.1 mm increase in the air gap (from 0.3 mm to 0.4 mm), the radiation efficiency is increased by 4.39%;  for the second 0.1 mm increase in the air gap (from 0.4 mm to 0.5 mm), the radiation efficiency is increased by 1.98%.

Table 5.1 Studies on Flat-wire Open Ring Parameters and Air Gap Spacing

| | L (mm) | H (mm) | W (mm) | $w_{slit}$ (mm) | h (mm) | $f_r$ (GHz) | BW (%) | η (%) | Gain (dBi) | Dir (dBi) |
|---|---|---|---|---|---|---|---|---|---|---|
| **Study on Ring Width, L** | **13** | 7.5 | 1.0 | 0.2 | 0.5 | **2.6349** | 1.01 | 85.58 | 7.86 | 8.54 |
| | **14** | 7.5 | 1.0 | 0.2 | 0.5 | **2.5028** | 0.96 | 84.13 | 7.82 | 8.57 |
| | **15** | 7.5 | 1.0 | 0.2 | 0.5 | **2.3822** | 0.90 | 82.45 | 7.81 | 8.65 |
| **Study on Ring Height, H** | 15 | **5.5** | 1.0 | 0.2 | 0.5 | **2.6532** | 0.83 | 81.04 | 7.79 | 8.70 |
| | 15 | **6.5** | 1.0 | 0.2 | 0.5 | **2.5072** | 0.88 | 81.89 | 7.78 | 8.65 |
| | 15 | **7.5** | 1.0 | 0.2 | 0.5 | **2.3822** | 0.90 | 82.45 | 7.81 | 8.65 |
| **Study on Ring Width, W** | 15 | 7.5 | **0.5** | 0.2 | 0.5 | **2.5431** | 1.01 | 76.97 | 7.45 | 8.59 |
| | 15 | 7.5 | **1.0** | 0.2 | 0.5 | **2.3822** | 0.90 | 82.45 | 7.81 | 8.65 |
| | 15 | 7.5 | **1.5** | 0.2 | 0.5 | **2.2676** | 0.85 | 86.36 | 7.94 | 8.57 |
| **Study on Slit Width, $w_{slit}$** | 15 | 7.5 | 1.0 | **0.2** | 0.5 | **2.3822** | 0.90 | 82.45 | 7.81 | 8.65 |
| | 15 | 7.5 | 1.0 | **1.2** | 0.5 | **2.4869** | 0.98 | 85.24 | 7.96 | 8.65 |
| | 15 | 7.5 | 1.0 | **2.2** | 0.5 | **2.5552** | 1.06 | 86.49 | 8.02 | 8.65 |
| **Study on Air Gap, h** | 15 | 7.5 | 1.0 | 0.2 | **0.3** | **2.1497** | 0.70 | 75.88 | 7.38 | 8.57 |
| | 15 | 7.5 | 1.0 | 0.2 | **0.4** | **2.2849** | 0.82 | 80.27 | 7.63 | 8.59 |
| | 15 | 7.5 | 1.0 | 0.2 | **0.5** | **2.3822** | 0.90 | 82.45 | 7.81 | 8.65 |

## II. Effect of the Slit Position

In order to investigate the effect of slit positions on the performance of a flat-wire open ring antenna, four antennas of the same dimensions (as given in Table 5.2) with four different slit positons, i.e. −z (bottom), +z (top), -z (left), and +y (right) as shown in Figure 5.2, are studied. The simulation results (Table 5.3) show that the one with the slit at the bottom of the ring, i.e. slit position = -z, provides more miniaturization than the other three slit positions. In addition to the advantage of being more miniaturized, the bottom slit also allows the antenna to have the highest gain/directivity and lowest cross-polarization among all. With the given dimensions, the gain, directivity and cross-polarization of the antenna with a bottom slit are 7.81 dBi, 8.65 dBi and -27.5 dB, respectively.

Table 5.2 Antenna Dimensions of a Single-turn Flat-wire Open Ring Antenna for the Slit Position Study

| L (mm) | H (mm) | W (mm) | h (mm) | $w_{slit}$ (mm) |
|--------|--------|--------|--------|-----------------|
| 15 | 7.5 | 1 | 0.5 | 0.2 |
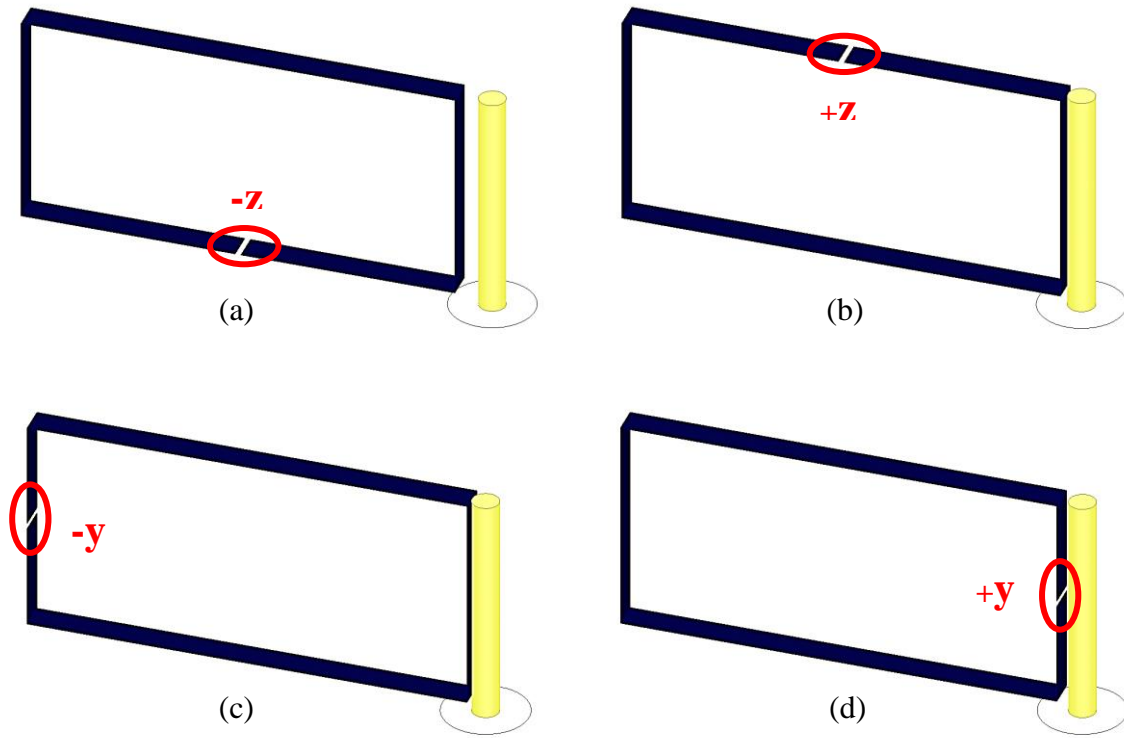
Figure 5.2 Probe-fed single-turn flat-wire open ring antennas with different slit positions: (a) −z, (b) +z, (c) −y, and (d) +y.

Table 5.3 Studies on Flat-wire Open Ring Slit Positions

| Slit Position | $f_r$ (GHz) | BW (%) | η (%) | Gain (dBi) | X-pol (dB) | Dir (dBi) |
|---|---|---|---|---|---|---|
| -z | 2.3822 | 0.90 | 82.45 | 7.81 | -27.50 | 8.65 |
| +z | 3.5717 | 1.40 | 85.52 | 4.80 | -21.17 | 5.48 |
| -y | 3.0647 | 2.36 | 95.89 | 5.27 | -10.72 | 5.45 |
| +y | 2.6105 | 1.25 | 85.91 | 6.73 | -16.48 | 7.39 |

### III. Effect of the U-shaped Ground Plane Size

In order to investigate the effect of the ground plane size on the antenna performance, a single-turn flat-wire open ring with various ground plane lengths and side wall heights is studied. The

antenna dimensions are given in Table 5.4. As discussed in Chapter 3, the directivity-ground plane length/side wall height curve only peaks at the optimal ground plane length/side wall height, which means the directivity increases with the increase in the ground plane length/side wall height before reaching the optimal value and decreases if the ground plane length/side wall height continues increasing after the optimal value.

Table 5.4 Antenna Dimensions of a Single-turn Flat-wire Open Ring Antenna for the Ground Plane Study

| L (mm) | H (mm) | W (mm) | h (mm) | $w_{slit}$ (mm) |
|--------|--------|--------|--------|-----------------|
| 15 | 7.5 | 1 | 0.5 | 0.2 |

In order to investigate the effect of the ground plane length, $L_{ground}$, the ground plane length is varied from $0.8\lambda$ to $1.3\lambda$ with an increment of $0.05\lambda$, while the side wall height, $H_{side\,wall}$, is set to be $0.32\lambda$ and all other antenna parameters are set to be the same as in Table 5.4. The simulation results (Table 5.5) show that the variation in the ground plane length has little effect on the resonant frequency, bandwidth and the efficiency, but can significant affect the directivity, gain and cross-polarization. More specifically, with a 2.04dB increase in directivity, 1.92dB increase in gain, and 8dB decrease in cross-polarization, there is only 0.15% bandwidth drop and 2.43% efficiency drop. As expected, there is a peak in both ground plane length-directivity ($L_{ground}$ − Directivity) and ground plane length-gain ($L_{ground}$ − Gain) curves, which occurs at $L_{ground} = 1.2\lambda$, as demonstrated in Figure 5.3. In other words, the optimal ground plane length for higher directivity/gain and lower cross-polarization is $L_{ground} = 1.2\lambda$.

Table 5.5 Effect of the Ground Plane Length, $L_{ground}$, on the Performance of a Single-turn Flat-wire Open Ring Antenna

| $H_{side\ wall}$ (mm) | $H_{side\ wall}$ /λ | $L_{ground}$/λ | $f_r$ (GHz) | BW (%) | η (%) | Gain (dBi) | X-pol (dB) | Dir (dBi) |
|---|---|---|---|---|---|---|---|---|
| 40 | 0.32 | 0.80 | 2.3677 | 1.04 | 85.21 | 5.84 | -19.02 | 6.54 |
| 40 | 0.32 | 0.85 | 2.3678 | 1.04 | 85.22 | 6.28 | -20.40 | 6.98 |
| 40 | 0.32 | 0.90 | 2.3706 | 1.04 | 85.24 | 6.64 | -21.65 | 7.33 |
| 40 | 0.32 | 0.95 | 2.3704 | 1.03 | 85.04 | 6.94 | -22.58 | 7.65 |
| 40 | 0.32 | 1.00 | 2.3745 | 1.01 | 84.26 | 7.23 | -24.03 | 7.98 |
| 40 | 0.32 | 1.05 | 2.3760 | 0.97 | 83.95 | 7.48 | -25.28 | 8.24 |
| 40 | 0.32 | 1.10 | 2.3783 | 0.95 | 83.46 | 7.64 | -25.71 | 8.43 |
| 40 | 0.32 | 1.15 | 2.3804 | 0.92 | 82.98 | 7.73 | -26.38 | 8.55 |
| 40 | 0.32 | **1.20** | 2.3817 | 0.89 | 82.78 | 7.76 | -27.02 | **8.58** |
| 40 | 0.32 | 1.25 | 2.3826 | 0.88 | 82.49 | 7.63 | -27.18 | 8.47 |
| 40 | 0.32 | 1.30 | 2.3822 | 0.88 | 82.14 | 7.29 | -26.93 | 8.15 |
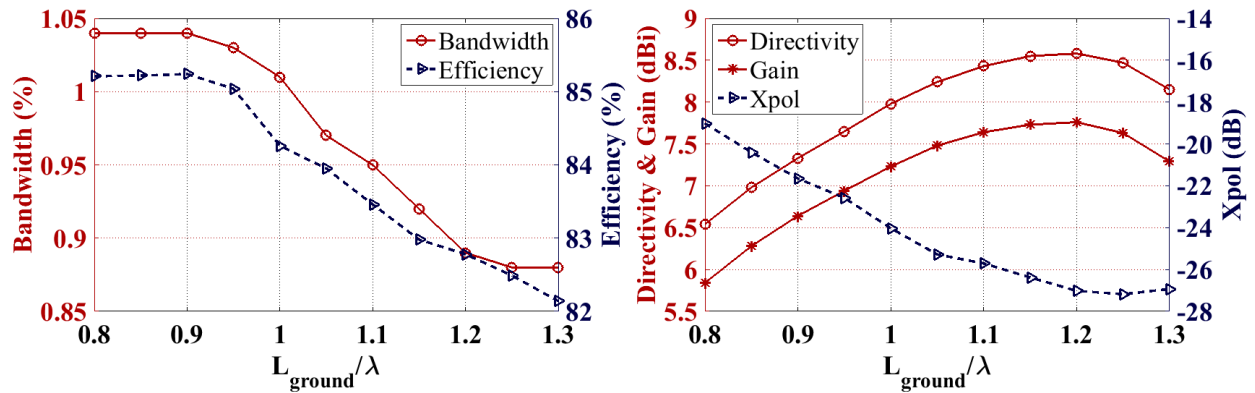


Figure 5.3 The effect of the ground plane length, $L_{ground}$, on the performance of a single-turn flat-wire open ring antenna.

Similarly, by fixing the ground plane length and other antenna parameters and varying the side wall height, $H_{side\ wall}$, the optimal side wall height can be found. Since the optimal ground plane length, i.e. $L_{ground} = 1.2\lambda$, has already been determined, it will be used for the side wall height study. Similar to the ground plane length, the side wall height has almost no effect on the resonant frequency, bandwidth, and radiation efficiency, but can significantly affect the directivity, gain and cross-polarization, as shown in Figure 5.4 (Table 5.6). It is obvious that the polarization performance can be improved by using a U-shaped ground plane, instead of a conventional planar ground plane ($H_{side\ wall} = 0\ mm$), and the degree of improvement depends on the height of the side walls. Interestingly enough, the Directivity-$H_{side\ wall}$, Gain-$H_{side\ wall}$, and Xpol-$H_{side\ wall}$ curves are very similar to those of the ground plane length study. More specifically, as the side wall height and the ground plane length approach the optimal values where the peaks occur, the effect of the increase in the side wall height/ground plane length becomes less significant. For example, for the first 10 mm increase in the side wall height (from $H_{side\ wall} = 15\ mm$ to $H_{side\ wall} = 25\ mm$), there is 0.72 dB increase in gain; for the second 10 mm increase in the side wall height (from $H_{side\ wall} = 25\ mm$ to $H_{side\ wall} = 35\ mm$), there is 0.46 dB increase in gain; for the third 10 mm increase in the side wall height (from $H_{side\ wall} = 35\ mm$ to $H_{side\ wall} = 45\ mm$), there is only 0.21 dB increase in gain. And of course, a further increase in both side wall height and ground plane length beyond the optimal values will result in a reduced directivity and gain, and increased cross-polarization. Thus, in order to effectively use the U-shaped ground plane, one should keep the ground plane length and the side wall height at or slightly lower than the optimal values, i.e. $L_{ground} \leq 1.2\lambda$ and $H_{side\ wall} \leq 0.36\lambda$.

Table 5.6 Effect of the Side Wall Height, $H_{side\,wall}$, on the Performance of a Single-turn Flat-wire Open Ring Antenna

| $H_{side\,wall}$ (mm) | $H_{side\,wall}/\lambda$ | $L_{ground}/\lambda$ | $f_r$ (GHz) | BW (%) | η (%) | Gain (dBi) | X-pol (dB) | Dir (dBi) |
|---|---|---|---|---|---|---|---|---|
| 0 | 0 | 1.20 | 2.3815 | 0.90 | 82.57 | 5.55 | -18.51 | 6.38 |
| 15 | 0.12 | 1.20 | 2.3818 | 0.89 | 82.39 | 6.42 | -20.56 | 7.26 |
| 20 | 0.16 | 1.20 | 2.3815 | 0.89 | 82.75 | 6.83 | -21.75 | 7.65 |
| 25 | 0.20 | 1.20 | 2.3819 | 0.90 | 82.44 | 7.14 | -23.23 | 7.97 |
| 30 | 0.24 | 1.20 | 2.3818 | 0.91 | 82.47 | 7.40 | -24.13 | 8.23 |
| 35 | 0.28 | 1.20 | 2.3822 | 0.89 | 82.36 | 7.60 | -26.04 | 8.44 |
| 40 | 0.32 | 1.20 | 2.3817 | 0.89 | 82.78 | 7.76 | -27.02 | 8.58 |
| **45** | **0.36** | 1.20 | 2.3822 | 0.90 | 82.45 | 7.81 | -27.50 | **8.65** |
| 50 | 0.40 | 1.20 | 2.3824 | 0.89 | 82.49 | 7.82 | -27.60 | 8.65 |
| 55 | 0.44 | 1.20 | 2.3824 | 0.89 | 82.44 | 7.77 | -27.38 | 8.60 |
| 60 | 0.48 | 1.20 | 2.3827 | 0.89 | 82.28 | 7.67 | -27.04 | 8.52 |
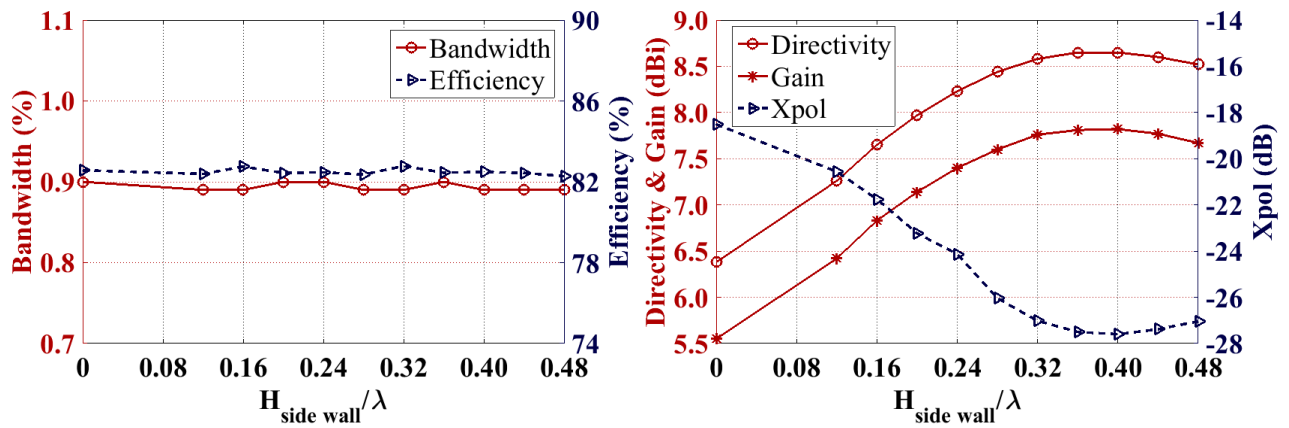


Figure 5.4 The effect of the side wall height, $H_{side\,wall}$, on the performance of a single-turn flat-wire open ring antenna.

It is worth mentioning that the optimal ground plane length and side wall height calculated here are based on only one antenna. For more accurate and generic expressions of the optimal ground plane length and side wall height that can be applied to different antennas with different operating frequencies or different configurations, more simulations have to be conducted.

## 5.2    Fabrication and Measurement Results

In order to experimentally verify the above discussion, a single-turn flat-wire open ring antenna, as shown in Figure 5.5 is fabricated and tested. The dimensions of the antenna (Table 5.7) are chosen for the convenience of the fabrication and measurement. Due to its softness and reasonably good conductivity, aluminum is chosen to be the material for both the ring and the ground plane. For a more rigid structure and more accurate dimensions, milling is used in making the ring, instead of folding. Nylon screws and nylon nuts are used to assemble the ring and the ground plane. The two nylon nuts, placed between the ground plane and the ring, are machined to be 1 mm high to achieve the desired air gap, namely, $h = 1\ mm$.



(a)

(b)

(c)
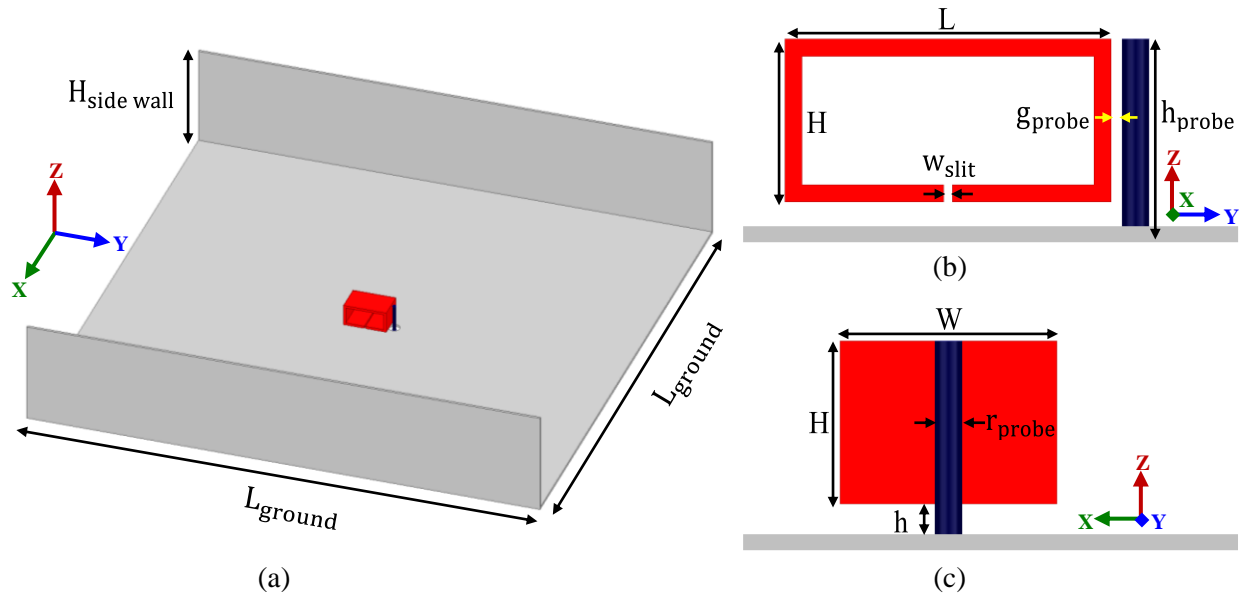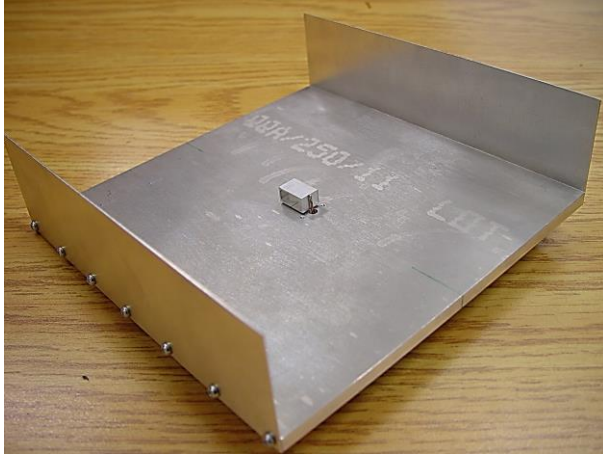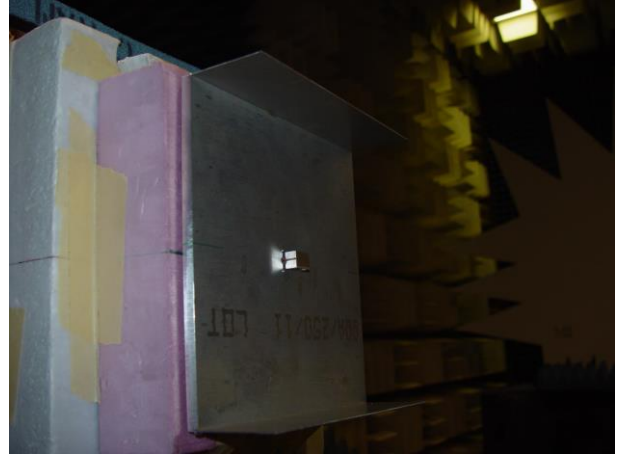
<center>(d)                                        (e)</center>

Figure 5.5 Probe-fed single-turn flat-wire aluminum open ring antenna. (a) Diametric view, (b) zoomed-in front view and (c) zoomed-in right side view of the simulated antenna; (d) fabricated antenna, and (e) antenna under test in the anechoic chamber at the University of Manitoba.

Table 5.7 Dimensions of the Single-turn Flat-wire Aluminum Open Ring Antenna.

| Flat-wire Open Ring | | | | Probe | | | Air Gap | U-shaped Ground | |
|---|---|---|---|---|---|---|---|---|---|
| L (mm) | H (mm) | W (mm) | $w_{slit}$ (mm) | $r_{probe}$ (mm) | $h_{probe}$ (mm) | $g_{probe}$ (mm) | h (mm) | $L_{ground}$ (mm) | $H_{side\ wall}$ (mm) |
| 15 | 7.5 | 10 | 0.2 | 0.625 | 8.5 | 0.5 | 1.0 | 180 | 45 |

Figure 5.6 shows the comparison of the simulated and measured S11 and gain results of the fabricated single-turn flat-wire aluminum open ring antenna. The solid curves are simulated results and the dashed curves are measured results. As can be seen, there is a small offset (0.0428 GHz) in the simulated (black solid curve) and measured (black dashed curve) resonant frequencies. Apart from the errors in the simulation and measurement, the fabrication imperfections can also contribute to such frequency offset. As discussed in the previous sections, the resonant frequency is quite sensitive to a few dimensions, such as the length ($L$), height ($H$) and width ($W$) of the ring, the slit width ($w_{slit}$), the air gap between the ring and the ground

plane ($h$), and the probe height ($h_{probe}$). Here, two of the listed parameters, namely, the slit width, $w_{slit}$, and the air gap, $h$, are used to demonstrate how the observed frequency offset can be caused by minor fabrication errors. The red and the blue solid curves in Figure 5.6 (a) show that a slight variation of 0.03 mm in slit width, $w_{slit}$, or 0.2 mm in air gap, $h$, either of them alone is enough to cause the observed frequency offset. Since the use of the two nylon screws in the fabricated antenna with a permittivity of 4.3 will slightly increase the effective electrical height of the air gap ($h$), which makes sense that the measurement (dashed black curve) and the simulation (solid black curve) agree better when the air gap in the simulation is slightly increased (solid blue curve). It is worth mentioning that the frequency offset may not be a result of the fabrication error in a single parameter, but is due to a combination of fabrication errors in multiple dimensions in addition to the simulation and measurement errors.

The simulated and measured radiation patterns have reasonably good agreement, as shown in Figure 5.6 (b). There is only 0.04 dB difference in the simulated and measured H-plane gains, that is, $Gain_{H\_simu} = 8.67\ dBi$ and $Gain_{H\_meas} = 8.71\ dBi$. However, a 0.43 dB gain difference in the measured E and H-planes is observed, which explains why there is a larger difference (0.39 dB) in the simulated and measured E-plane gains. The slight misalignment during the antenna measurement can be one of the reasons for such difference in the two planes, and can be improved by improving the positioning of the antenna under test.

Table 5.8 Simulation and Measurement Results of the Fabricated Single-Turn Flat-wire Aluminum Open Ring Antenna.

| | $f_r$ (GHz) | BW (%) | Gain (dBi) | X-pol (dB) |
|---|---|---|---|---|
| **Simulation** | 1.9260 | 0.84 | 8.67 | -29.51 |
| **Measurement** | 1.9688 | 1.12 | 8.71 | -25.22 |



(a)
(b)
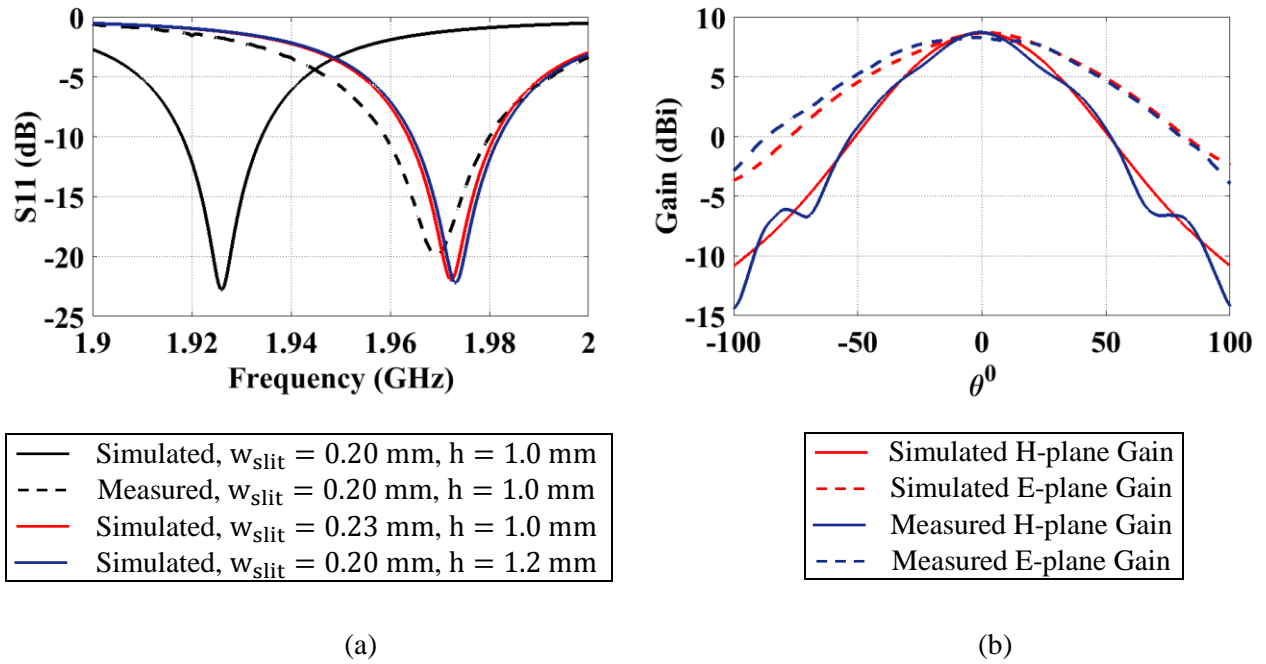
Figure 5.6 The comparison of the simulated and measured results of the fabricated single-turn flat-wire aluminum open ring antenna ($w_{slit}$ = 0.20 mm, h = 1.0 mm): (a) Simulated (solid black) and measured (dashed black) S11s of the fabricated antenna, and simulated S11s of the fabricated antenna with fabrication errors considered (solid red and solid blue); (b) Simulated (red) and measured (blue) E (dashed) and H-plane (solid) radiation patterns of the fabricated antenna.

## 5.3  Two-turn Flat-wire Open Ring Antenna

The added inner split ring in a complimentary split ring resonator (CSRR) enables further miniaturization of a split ring resonator (SRR) [41]. In this section, the possibility of further miniaturizing a single-turn flat-wire open ring antenna by adding an inner open ring is

investigated. The dimensions of the two-turn flat-wire open ring antenna are shown in Table 5.9. The widths of the outer and inner rings are the same, and the spacing between the two rings is 0.5 mm. There are a few slit position combinations of the outer and inner open rings. Here, the slit of the outer ring is fixed at the bottom of the ring, i.e. –z, and the slit position of the inner ring is varied, as shown in Figure 5.7.

Table 5.9 Dimensions of the Two-turn Flat-wire Open Ring Antenna

| L (mm) | H (mm) | W (mm) | h (mm) | $w_{slit}$ (mm) | Spacing (mm) |
|--------|--------|--------|--------|-----------------|--------------|
| 15 | 7.5 | 1 | 0.5 | 0.2 | 0.5 |
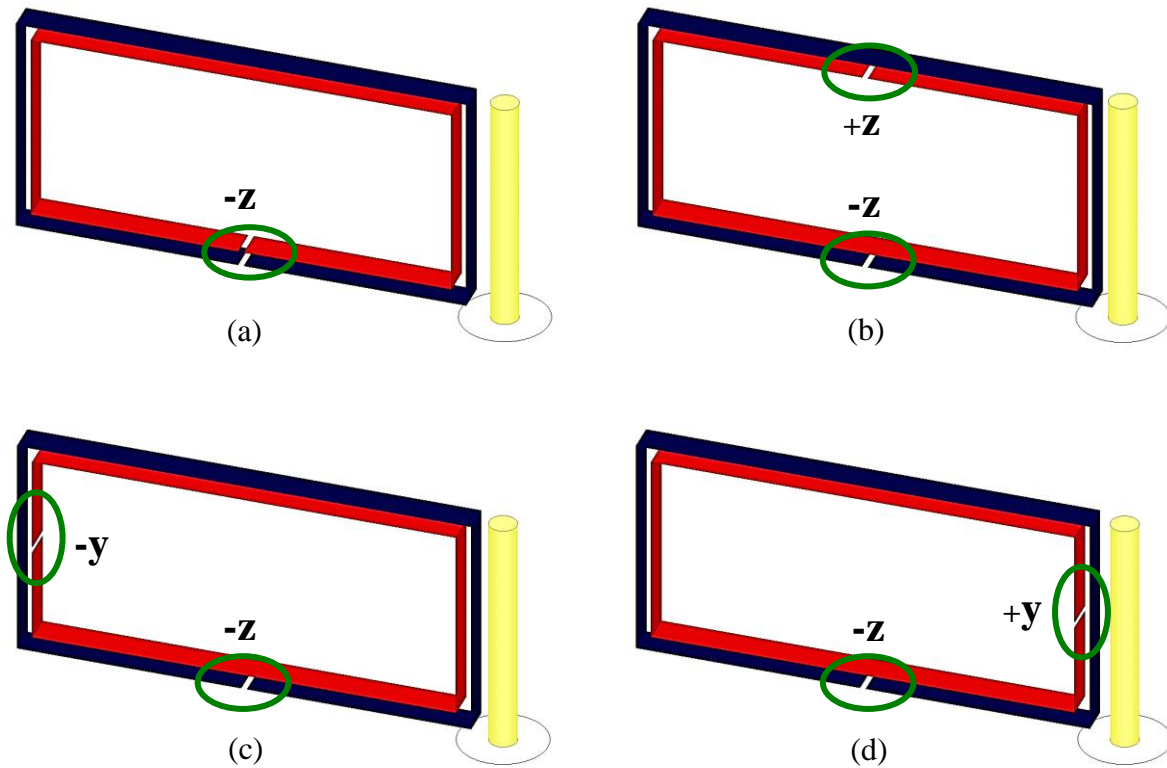


Figure 5.7 Two-turn flat-wire open ring antennas with different slit combinations. (a) Outer: -z, inner: -z, (b) outer: -z, inner: +z, (c) outer: -z, inner: -y, and (d) outer: -z, inner: +y.

Table 5.10 demonstrates the performance of the two-turn flat-wire open rings with varying inner slit positions. The results are compared with that of the single-turn flat-wire open ring of the same dimensions (as shown in table Table 5.9). It is found that the two-turn open ring with outer slit $-z$ and inner slit $+z$ allows the most miniaturization with a frequency shift of 0.6602 GHz ($f_{r\_single-trun}$ =2.3822 GHz, $f_{r\_two-trun\_-z\&+z}$=1.722 GHz), while the one with outer slit $-z$ and inner slit $-z$ allows the least miniaturization with a frequency shift of only 0.0359 GHz ($f_{r\_single-trun}$ = 2.3822 GHz, $f_{r\_two-trun\_-z\&+z}$= 2.3463 GHz). As expected, these miniaturized antennas, with the inner slit at $+z$, $-y$, or $+y$, suffer from different degrees of performance degradation, such as reduced radiation efficiency and lowered gain. In order to improve the efficiency and the gain, two methods are investigated. One is to increase the spacing between the outer and the inner ring, *Spacing*, and the other is to increase the widths of both rings, *W*. It is observed that both methods can successfully improve the antenna performance, but increasing the widths of the rings can further miniaturize the antenna while improving the efficiency and the gain of the antenna. For example, the two-turn flat-wire open ring with the $-z$ and $+z$ slit combination has an efficiency of 59.72% and a gain of 6.13 dBi when the spacing between the two rings is 0.5 mm and the ring width is 1 mm. By increasing the spacing between the two rings from 0.5 mm to 1 mm, the efficiency and the gain can be increased to 75.23% and 7.18 dBi, respectively, but at the expense of an increased resonant frequency (from 1.722 GHz to 2.0722 GHz). However, keeping the spacing fixed at 1 mm and increasing the widths of the rings from 0.5 mm to 1 mm, the efficiency and the gain will be increased to 77.86% and 7.36 dBi, respectively, and more importantly, with a decrease in the resonant frequency by 0.242 GHz.

Without the inner ring, the width of the ring, $W$, has to be increased from 1 mm to 9 mm in order to have the same resonant frequency (namely 1.7220 GHz) as its most miniaturized two-turn counterpart, with all other antenna parameters remaining the same. Although the two-turn ring antenna ($W = 1$ mm) is more compact than the single-turn ring antenna ($W = 9$ mm), the performance of the single-turn ring antenna is significantly better than that of the two-turn ring antenna, with a wider bandwidth (0.71%), higher efficiency (98.43%), and higher gain (8.58 dBi). Therefore, depending on the miniaturization requirements, one can either have a single-turn open ring with a wider ring width and better antenna performance or a two-turn open ring with a narrower ring width and relatively deteriorated antenna performance, or the combination of both, namely a two-turn open ring with an increased ring width and reasonably good performance.

Table 5.10 Performance of the Two-turn Flat-wire Open Ring Antennas with Different Inner Slit Positions

| Outer Slit Position | Inner Slit Position | Spacing (mm) | W (mm) | $f_r$ (GHz) | BW (%) | η (%) | Gain (dBi) | X-pol (dB) | Dir (dBi) |
|---|---|---|---|---|---|---|---|---|---|
| -z | No Inner Ring | - | 1 | 2.3822 | 0.90 | 82.45 | 7.81 | -27.50 | 8.65 |
| | | **-** | **9** | **1.7225** | **0.71** | **98.43** | **8.58** | **-35.10** | **8.64** |
| -z | -z | 0.5 | 1 | 2.3463 | 0.89 | 83.58 | 7.82 | -27.70 | 8.60 |
| | | 1 | 1 | 2.3579 | 0.89 | 83.26 | 7.80 | -27.02 | 8.59 |
| | | 1 | 2 | 2.1471 | 0.79 | 87.36 | 7.99 | -28.82 | 8.57 |
| | +z | **0.5** | **1** | **1.7220** | **0.42** | **59.72** | **6.13** | **-29.51** | **8.37** |
| | | 1 | 1 | 2.0722 | 0.63 | 75.23 | 7.18 | -28.22 | 8.42 |
| | | 1 | 2 | 1.8302 | 0.51 | 77.86 | 7.36 | -30.02 | 8.44 |
| | -y | 0.5 | 1 | 1.8511 | 0.51 | 68.24 | 6.65 | -23.75 | 8.31 |
| | | 1 | 1 | 2.1497 | 0.72 | 79.31 | 7.40 | -24.23 | 8.41 |
| | | 1 | 2 | 1.9096 | 0.58 | 81.16 | 7.54 | -26.54 | 8.45 |
| | +y | 0.5 | 1 | 1.8476 | 0.49 | 67.02 | 6.80 | -40.82 | 8.54 |
| | | 1 | 1 | 2.1504 | 0.69 | 78.58 | 7.55 | -33.40 | 8.60 |
| | | 1 | 2 | 1.9078 | 0.57 | 80.93 | 7.64 | -34.60 | 8.56 |

## 5.4   Summary

The previous chapter showed the potential of the split-ring-shaped metallization working as an individual antenna, and this chapter conducted a more comprehensive study on such an antenna, which was referred to as flat-wire open ring antenna in this chapter. In the first section of this

chapter, a single-turn probe-fed flat-wire open ring antenna was investigated. Studies on various antenna parameters, including the ring length, ring height, ring width, slit width, air gap, slit position, and ground plane size, were performed. The gap position study showed that a slit at the bottom of the ring, i.e. $slit\ position = -z$, enables the most miniaturization while providing the highest gain and directivity. An interesting result was observed from the ring width study: unlike all other parameters, an increase in the ring width, $W$, can miniaturize the antenna without reducing its radiation efficiency. Instead, it will increase the efficiency. In the second section, a single-turn flat-wire open ring antenna was fabricated and measured. The measurement results and the simulation results were compared, and the possible causes for the disagreements between the two results were analyzed. In the third section, two-turn flat-wire open ring antennas with different combinations of inner and outer slit positions were investigated. With the outer ring slit being fixed at –z, it was found that the combination of the outer ring with the slit at –z and inner ring with the slit at +z enables the most miniaturization. Performance degradation, i.e. efficiency drop, was observed among all the miniaturized antennas, and two techniques, namely increasing the ring width, $W$, and increasing the spacing between the inner and outer rings, $Spacing$, were verified to be able to successfully improve the performance of the miniaturized two-turn flat-wire open ring antenna.

# Chapter 6

# Conclusions and Future Work

## 6.1   Conclusions

Chapter 1 discussed the motivation of antenna miniaturization and the available miniaturization techniques. The advantages and disadvantages of having a small antenna were briefly discussed. The main drawbacks of antenna miniaturization are having to sacrifice the antenna performance, such as radiation efficiency, impedance bandwidth and matching, for its compactness. So if such performance deterioration can be minimized, the miniaturized antenna will be more useful. Among the different miniaturization techniques, one particular technique, namely artificial high-permeability loading, was reported to be able to reduce the degradation in the efficiency and the bandwidth of the miniaturized antenna.

Unlike natural magnetic materials, the high-permeability in an artificial material is artificially engineered based on an otherwise non-magnetic material. In Chapter 2, by replicating the major magnetization mechanism in a natural magnetic material, high permeability was successfully induced in a dielectric material (i.e. Rogers RT/duroid 5880) by employing and properly arranging a split ring resonator (SRR) with respect to the magnetic field. The parametric study of an SRR unit cell showed that the properties of the engineered material, such as peak permeability and resonant frequency, can be modified by altering the unit cell parameters. Unlike the loss mechanisms in a natural magnetic material, the loss mechanisms in an engineered material, namely dielectric loss and conductor loss, do not necessarily make the material too lossy to

operate in the microwave regime. The possible ways of reducing those losses in the engineered material were discussed at the end of the chapter.

Chapter 3 demonstrated how a dielectric resonator antenna could be miniaturized by using the artificial high-permeability material proposed in Chapter 2. In order to evaluate the miniaturization capability of the SRR loaded DRAs, two evaluation methods for both high and low-permittivity based antennas were defined in the first section of the chapter, namely frequency comparing method and refractive index comparing method. In the second section, the effects of SRR parameters and SRR arrangements on the antenna performance were studied. From these studies, we drew the following conclusions:

1. Increasing the probe height, $h_{probe}$, will increase the miniaturization capability, but at the expense of an increased cross-polarization and a decreased gain/directivity.

2. High cross-polarization and low gain/directivity, caused by increasing the probe height, can be addressed by replacing the conventional 2-D ground plane with a 3-D U-shaped ground plane.

3. The slit at the bottom of the SRR, i.e. $slit\ position = -z$, enables the most miniaturization.

4. Increasing the ring width, $w$, will shift the resonant frequency up and increase the radiation efficiency and the impedance bandwidth.

5. Similarly, increasing the gap width, $g$, will also shift the resonant frequency up and increase the radiation efficiency and the impedance bandwidth.

6. The miniaturization capability varies with the SRR arrangement, and it follows the following order:

$$MC_{3\vec{x} \times 3\vec{y} \times 3\vec{z}} < MC_{3\vec{x} \times 3\vec{y} \times 2\vec{z}} < MC_{3\vec{x} \times 2\vec{y} \times 2\vec{z}} < MC_{3\vec{x} \times 3\vec{y} \times 1\vec{z}} < MC_{3\vec{x} \times 2\vec{y} \times 1\vec{z}} < MC_{3\vec{x} \times 1\vec{y} \times 1\vec{z}}.$$

As the loaded DRAs became more miniaturized, reduced radiation efficiencies and narrowed impedance bandwidths were observed. Two methods, namely increasing the ring width and increasing the gap width, were verified to be able to effectively improve the efficiency and the bandwidth of the miniaturized antennas. In the third section of the chapter, a $1\vec{x} \times 1\vec{y} \times 1\vec{z}$ SRR loaded DRA was fabricated and measured. The measurement results and the simulation results were compared, and the possible causes for the disagreements between the two results were analyzed.

In Chapter 4, the possibility of further miniaturizing SRR loaded DRAs by applying metallization on the dielectric surfaces were investigated. Two types of ring shaped metallization, namely, U-shaped and split-ring-shaped metallization, were investigated. The U-shaped metallization was studied in the first section of the chapter, and it was applied to both SRR loaded and unloaded DRAs. The simulation results verified that the U-shaped metallization alone can indeed effectively miniaturize a conventional DRA without much performance degradation. And extra miniaturization was also observed in SRR loaded DRAs, except for one ring arrangement, namely $3\vec{x} \times 1\vec{y} \times 1\vec{z}$. Despite no extra miniaturization gained from the addition of the U-shaped metallization, the one with $3\vec{x} \times 1\vec{y} \times 1\vec{z}$ SRRs still remains the most miniaturized among all six arrangements. The second section studied the effect of the split-ring-shaped metallization on an unloaded conventional DRA and a loaded DRA with $3\vec{x} \times 1\vec{y} \times 1\vec{z}$ SRRs. It was found that although the split-ring-shaped metallization does not add much

miniaturization to the SRR loaded DRA, it can significantly degrade the antenna performance. However, a significant miniaturization was observed when the split-ring-shaped metallization was applied to the unloaded DRA. Unlike the metallized loaded DRA, the antenna performance of the metallized unloaded DRA can be easily improved. With all other antenna parameters remaining the same, the performance improvement could be easily achieved by increasing the air gap, $h$, between the ground plane and the metallization. In other words, the split-ring-shaped metallization can work more efficiently as an antenna on its own.

In Chapter 5, such split-ring-shaped-metallization working as an individual antenna, referred to as flat-wire open ring antenna, was studied. In the first section of the chapter, a single-turn probe-fed 3-D split ring antenna was investigated. Parametric studies on various antenna parameters were performed and following conclusions were drawn:

1.  Resonant frequency increases as the ring length, $L$, and the ring height, $H$, increase.

2.  Slit at the bottom of the ring, i.e. $slit\ position = -z$, enables the most miniaturization while providing the highest gain and directivity.

3.  Unlike all other parameters, an increase in the ring width, $W$, can miniaturize the antenna without reducing the radiation efficiency. Instead, it will increase the efficiency.

In the second section of the chapter, a single-turn flat-wire open ring antenna was fabricated and measured. The measurement results and the simulation results were compared, and the possible causes of the disagreements between the two results were analyzed. In the third section, two-turn flat-wire open ring antennas with different combinations of inner and outer slit positions were investigated. With the outer ring position being fixed at $-z$, it was found that the combination of

the outer ring with a slit at $-z$ and inner ring with a slit at $+z$ allows the most miniaturization. Performance degradation, i.e. efficiency drop, was observed among all the miniaturized antennas, and two techniques, namely increasing the ring width, $W$, and increasing the spacing between the inner and outer rings, $Spacing$, were verified to be able to successfully improve the efficiency of the miniaturized antenna.

## 6.2 Future Work

Based on the studies in this work, possible future work includes:

1. Investigate DRAs loaded with more miniaturized loops. Since the studies in Chapter 3 have demonstrated that reducing the resonant frequency of the SRR inclusions can lead to more miniaturization in the host DRA. DRAs with more miniaturized electrical loops will be investigated in the future.

2. Miniaturize other types of antennas using artificial high-μ materials. Chapter 3 has demonstrated that loading a DRA with artificial high-μ materials can successfully miniaturize the antenna. By using the same technique, other types of antennas should also be miniaturized.

3. Investigate flat-wire open ring antennas of more complicated configurations that can lead to more miniaturization.

# References

[1]  L. J. Chu, "Physical Limitations of Omni-Directional Antennas," *Journal of applied physics,* vol. 19, no. 12, pp. 1163-1175, 1948.

[2]  H. Wheeler, "Small antennas," *IEEE Transactions on Antennas and Propagation,* vol. 23, no. 4, pp. 462-469, 1975.

[3]  D. H. Schaubert, D. M. Pozar and A. Adrian, "Effect of microstrip antenna substrate thickness and permittivity: comparison of theories with experiment," *IEEE Transactions on Antennas and Propagation,* vol. 37, no. 6, pp. 677-682, 1989.

[4]  R. K. Mongia, A. Ittibipoon and M. Cuhaci, "Low profile dielectric resonator antennas using a very high permittivity material," *Electronics letters,* vol. 30, no. 17, pp. 1362-1363, 1994.

[5]  G. Yang, X. Xing, A. Daigle, M. Liu, O. Obi, S. Stoute, K. Naishadham and N. Sun, "Tunable miniaturized patch antennas with self-biased multilayer magnetic films," *IEEE Transactions on antennas and propagation,* vol. 57, no. 7, pp. 2190-2193, 2009.

[6]  Y. Shirakata, N. Hidaka, M. Ishitsuka, A. Teramoto and T. & Ohmi, "High permeability and low loss Ni–Fe composite material for high-frequency applications," . *IEEE Transactions on Magnetics, 44(9), 2100-2106.,* vol. 44, no. 9, pp. 2100-2106, 2008.

[7]  K. Buell, H. Mosallaei and K. Sarabandi, "A substrate for small patch antennas providing

tunable miniaturization factors," *IEEE Transactions on Microwave Theory and Techniques,* vol. 54, no. 1, pp. 135-146, 2006.

[8] R. C. Hansen and M. Burke, "Antennas with magneto-dielectrics," *Microwave and optical technology letters,* vol. 26, no. 2, pp. 75-78, 2000.

[9] P. Ikonen and S. Tretyakov, "On the advantages of magnetic materials in microstrip antenna miniaturization," *Microwave and Optical Technology Letters,* vol. 50, no. 12, pp. 3131-3134, 2008.

[10] W. S. Chen, "Single-feed dual-frequency rectangular microstrip antenna with square slot," *Electronics Letters,* vol. 34, no. 3, pp. 231-232, 1998.

[11] H. D. Chen, "A dual-frequency rectangular microstrip antenna with a circular slot," *Microwave and Optical Technology Letters,* vol. 18, no. 2, pp. 130-132, 1998.

[12] C. L. Tang and K. L. Wong, "A modified equilateral-triangular-ring microstrip antenna for circular polarization," *Microwave and Optical Technology Letters,* vol. 23, no. 2, pp. 123-126, 1999.

[13] H. T. Nguyen, "Miniaturizing microstrip patch antennas by slot loading," M.Sc. thesis, University of Manitoba, Winnipeg, 2006.

[14] J. Anguera, L. Boada, C. Puente, C. Borja and J. Soler, "Stacked H-shaped microstrip patch antenna," *IEEE Transactions on Antennas and Propagation,* vol. 52, no. 4, pp. 983-993, 2004.

[15] R. Raju, "Investigation of Miniaturized Microstrip Antenna Efficiency Enhancement," M.Sc. thesis, University of Manitoba, Winnipeg, 2015.

[16] J. H. Lu and K. L. Wong, "Slot-loaded, meandered rectangular microstrip antenna with compact dual frequency operation," *Electronics Letters,* vol. 34, no. 11, pp. 1048-1050, 1998.

[17] G. Ramesh, Microstrip antenna design handbook, Artech house, 2001.

[18] C. A. Balanis, Antenna theory: analysis and design, John Wiley & Sons, 2016.

[19] A. K. Skrivervik, J. F. Zurcher, O. Staub and J. R. Mosig, " PCS antenna design: The challenge of miniaturization," *IEEE Antennas and Propagation Magazine,* vol. 43, no. 4, pp. 12-27, 2001.

[20] R. Waterhouse, "Small microstrip patch antenna," *Electronics Letters,* vol. 31, no. 8, pp. 604-605, 1995.

[21] R. Porath, "Theory of miniaturized shorting-post microstrip antennas," *IEEE Transactions on Antennas and Propagation,* vol. 48, no. 1, pp. 41-47., 2000.

[22] K. L. Wong, Compact and broadband microstrip antennas, vol. 168, John Wiley & Sons, 2004.

[23] R. K. Mongia, "Reduced size metallized dielectric resonator antennas," in *in APS International Symposium, 1997. IEEE., 1997 Digest*, 1997, July.

[24] M. Tam and R. D. Murch, "Half volume dielectric resonator antenna designs," *Electronics Letters,* vol. 33, no. 23, pp. 1914-1916, 1997.

[25] K. L. Wong and Y. F. Lin, "Small broadband rectangular microstrip antenna with chip-resistor loading," *Electronics Letters,* vol. 33, no. 19, pp. 1593-1594, 1997.

[26] J. H. Lu, C. L. Tang and K. L. Wong, "Microwave and Optical Technology Letters," *Slot‐coupled compact broadband circular microstrip antenna with chip‐resistor and chip‐capacitor loadings,* vol. 18, no. 5, pp. 345-349, 1998.

[27] D. H. Lee, A. Chauraya, Y. Vardaxoglou and W. S. Park, "A compact and low-profile tunable loop antenna integrated with inductors," *IEEE Antennas and Wireless Propagation Letters,* vol. 7, pp. 621-624, 2008.

[28] D. R. Smith, "Novel Electromagnetic Media," Duke University, [Online]. Available: http://people.ee.duke.edu/~drsmith/metamaterials/metamaterial_elements.htm.

[29] K. Buell, "Development of engineered magnetic materials for antenna applications," Doctoral dissertation, The University of Michigan, Ann Arbor, 2005.

[30] Y. Liu, R. Raju, L. Shafai and C. Shafai, "A miniaturized artificial magneto-dielectric resonator antenna with split ring resonators," in *in ANTEM, 2016 17th International Symposium on. IEEE*, Montreal, 2016.

[31] Y. Liu, L. Shafai and C. Shafai, "Effects of Split Ring Arrangement and Slit location on the Miniaturization Performance of Split," in *32nd URSI GASS, Montreal, 19-26 August 2017*,

Montreal, 19-26 August 2017.

[32] A. Alù, F. Bilotti, N. Engheta and L. Vegni, "Subwavelength, compact, resonant patch antennas loaded with metamaterials," *IEEE Transactions on Antennas and Propagation,* vol. 55, no. 1, pp. 13-25, 2007.

[33] F. Bilotti, A. Alu and L. Vegni, "Design of miniaturized metamaterial patch antennas with-negative loading," *IEEE Transactions on Antennas and Propagation,* vol. 56, no. 6, pp. 1640-1647, 2008.

[34] S. Hrabar, D. Bonefacic and D. Muha, "Application of wire-based metamaterials for antenna miniaturization," in *In Antennas and Propagation, 2009. EuCAP 2009. 3rd European Conference on*, 2009.

[35] D. Ramaccia, F. Scattone, F. Bilotti and A. Toscano, "Broadband compact horn antennas by using EPS-ENZ metamaterial lens," *Antennas and Propagation, IEEE Transactions on,* vol. 61, no. 6, pp. 2929-2937, 2013.

[36] J. G. Pollock and A. K. & Iyer, "Miniaturized circular-waveguide probe antennas using metamaterial liners," *Antennas and Propagation, IEEE Transactions on,* vol. 63, no. 1, pp. 428-433, 2015.

[37] K. C. Kao, Dielectric phenomena in solids, Academic press, 2004.

[38] W. Lewin, "Lec 21: Magnetic Materials | 8.02 Electricity and Magnetism," Spring 2002.

[39] C. A. Balanis, Advanced engineering electromagnetics, John Wiley & Sons, 1999.

[40] J. B. Pendry, A. J. Holden, D. J. Robbins and W. J. Stewart, "Magnetism from conductors and enhanced nonlinear phenomena," *IEEE transactions on microwave theory and techniques,* vol. 47, no. 11, pp. 2075-2084., 1999.

[41] F. Bilotti, A. Toscano and L. Vegni, "Design of spiral and multiple split-ring resonators for the realization of miniaturized metamaterial samples," *IEEE Transactions on Antennas and Propagation,* vol. 55, no. 8, pp. 2258-2267, 2007.

[42] ANSYS, [Online]. Available: http://www.ansys.com/products/electronics/ansys-hfss.

[43] Ansoft, "Maxwell Online Help System," [Online]. Available: http://read.pudn.com/downloads107/ebook/442805/hfss/converge.pdf.

[44] X. Chen, T. Grzegorczyk, B. Wu, J. Pacheco Jr and J. Kong, "Robust method to retrieve the constitutive effective parameters of metamaterials," *Physical Review E,* vol. 70, no. 1, p. 016608, 2004.

[45] D. Smith, D. Vier, T. Koschny and C. Soukoulis, "Electromagnetic parameter retrieval from inhomogeneous metamaterials," *Physical review E,* vol. 71, no. 3, p. 036617, 2005.

[46] J. Reinert, A. Brockmeyer and R. W. De Doncker, "Calculation of losses in ferro-and ferrimagnetic materials based on the modified Steinmetz equation," *IEEE Transactions on Industry applications,* vol. 37, no. 4, pp. 1055-1061, 2001.

[47] J. B. Goodenough, "Summary of losses in magnetic materials," *IEEE Transactions on magnetics,* vol. 38, no. 5, pp. 3398-3408, 2002.

[48] C. P. Steinmetz, "On the law of hysteresis," *In IEEE Proceeding,* vol. 72, no. 2, pp. 197-221, 1984.

[49] P. Virgil, A. J. Shapiro and R. D. Shull, "Reduction of hysteresis losses in the magnetic refrigerant Gd5Ge2Si2 by the addition of iron," *Nature,* vol. 429, no. 6994, p. 853, 2004.

[50] J. Shen, B. Gao, H. Zhang, F. Hu, Y. Li, J. Sun and B. Shen, "Reduction of hysteresis loss and large magnetic entropy change in the Na Zn 13-type LaPrFeSiC interstitial compounds," *Applied Physics Letters,* vol. 91, no. 14, p. 142504, 2007.

[51] H. Zhang, B. Shen, Z. Xu, X. Zheng, J. Shen, F. Hu, J. Sun and Y. Long, "Reduction of hysteresis loss and large magnetocaloric effect in the C-and H-doped La (Fe, Si) 13 compounds around room temperature," *Journal of Applied Physics,* vol. 111, no. 7, p. 07A909, 2012.

[52] J. Li, T. Abdallah and C. R. Sullivan, "Improved calculation of core loss with nonsinusoidal waveforms," in *Industry Applications Conference, 2001. Thirty-Sixth IAS Annual Meeting. Conference Record of the 2001 IEEE*, 2001.

[53] Murat, "Mathworks," 5 December 2013. [Online]. Available: https://www.mathworks.com/matlabcentral/answers/108733-how-can-i-draw-this-loop. [Accessed 12 October 2016].

[54] R. W. Erickson and D. Maksimovic, Fundamentals of power electronics, Springer Science & Business Media, 2007.

[55] P. D. Agarwal, "Eddy-current losses in solid and laminated iron," *Transactions of the American Institute of Electrical Engineers, Part I: Communication and Electronics,* vol. 78, no. 2, pp. 169-181, 1959.

[56] Z. Barber, A. Kalorkoti, L. Sallows and D. Brook, "DoITPoMS," UK Centre for Materials Education and the Department of Materials Science and Metallurgy, University of Cambridge, 14 August 2008. [Online]. Available: https://www.doitpoms.ac.uk/tlplib/dielectrics/loss.php.

[57] C. Zhu, "Dielectric Loss," Dept. of ECE, National University of Singpore.

[58] G. Koehler, Circuits and Networks, Macmillan, 1955.

[59] B. Du, "The skin effect and the copper loss due to skin effect," October 2006. [Online]. Available: https://wenku.baidu.com/view/1639d4a6a58da0116c174997.html.

[60] X. Nan and C. R. Sullivan, "An improved calculation of proximity-effect loss in high-frequency windings of round conductors," in *Power Electronics Specialist Conference, 2003. PESC'03. 2003 IEEE 34th Annual. IEEE*, June 2003.

[61] G. S. Smith, "Proximity effect in systems of parallel conductors," *Journal of Applied Physics,* vol. 43, no. 5, pp. 2196-2203, 1972.

[62] A. Ludwig, "The definition of cross polarization," *IEEE Transactions on Antennas and Propagation,* vol. 21, no. 1, pp. 116-119, 1973.

[63] P. Arapoglou, K. Liolis, M. Bertinelli, A. Panagopoulos, P. Cottis and R. De Gaudenzi,

"MIMO over satellite: A review," *IEEE communications surveys & tutorials,* vol. 13, no. 1, pp. 27-51, 2011.

[64] W. H. Hsu and K. L. Wong, "Broadband probe-fed patch antenna with a U-shaped ground plane for cross-polarization reduction," *IEEE Transactions on Antennas and Propagation,* vol. 50, no. 3, pp. 352-355, 2002.

[65] R. K. Mongia and A. Ittipiboon, "Theoretical and experimental investigations on rectangular dielectric resonator antennas," *IEEE Transactions on Antennas and Propagation,* vol. 45, no. 9, pp. 1348-1356, 1997.

[66] M. T. Lee, K. M. Luk, K. W. Leung and M. K. Leung, "A small dielectric resonator antenna," *IEEE Transactions on Antennas and Propagation,* vol. 50, no. 10, pp. 1485-1487, 2002.